

5045

UNIVERSITY OF HAWAII LIBRARY

UNDERSTANDING THE COMPOSITION AND EVOLUTION
OF THE MARTIAN SURFACE USING THERMAL INFRARED
LABORATORY ANALYSES AND REMOTE SENSING

A DISSERTATION SUBMITTED TO
THE GRADUATE DIVISION OF THE UNIVERSITY OF HAWAII
IN PARTIAL FULFILLMENT OF THE REQUIREMENTS FOR THE DEGREE OF
DOCTOR OF PHILOSOPHY
IN
GEOLOGY AND GEOPHYSICS

MAY 2008

By
William Carl Koeppen

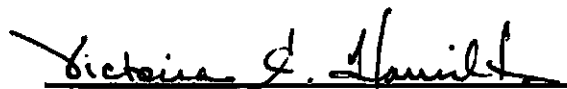
Dissertation Committee:

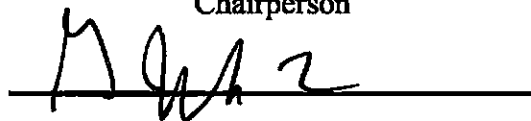
Victoria E. Hamilton, Chairperson
G. Jeffrey Taylor
Sarah A. Fagents
Paul G. Lucey
Eric J. Hochberg

5045

We certify that we have read this dissertation and that, in our opinion, it is satisfactory in scope and quality as a dissertation for the degree of Doctor of Philosophy in Geology and Geophysics.

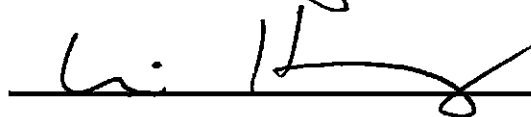
DISSERTATION COMMITTEE


Chairperson









ACKNOWLEDGEMENTS

My parents. My dad took me outside and instilled a love for the natural world. He took my fish off the hook, explained the cut bank of a stream (so I wouldn't fall in), and helped me identify rocks in our driveway. My mom has supported all of my obsessions, including this one. She even took Introduction to Geology to figure out what I do.

Juniata College. Drs. Bob Washburn, Larry Mutti, and Dave Lehmann of the geology department, and Drs. James White and Jim Borgardt of the physics department, not to mention Drs. Emil Nagengast, James Roney, and Mark Hochberg (from whom I just took one life-changing class each). Juniata provided me with a strong background in the fundamentals of physics, geology, and Life coupled with the confidence to ask questions and think freely. Everyone there encouraged me to attend graduate school, and they made me realize that a PhD was not just achievable, but that it might even be useful.

Scott and Vicky. Scott Anderson mentored me as an impressionable intern at JPL. He chatted when I had no friends, paid when I was poor, and taught me everything about rock-climbing. He introduced me to my advisor, Vicky Hamilton, and I really could not have asked for someone better. She gave me useful advice and scientific insights, read through terrible paper drafts, and she is both an optimist and a realist about deadlines.

My committee. Drs. Vicky Hamilton, Jeff Taylor, Sarah Fagents, Paul Lucey, and Eric Hochberg. You deserve medals of patience, and all you get is this document.

My friends. You won't even get a copy of this, but you know who you are. Roommates, fellow grad students, dancers, surfers, film buffs, symposium organizers. You got me through this. Now what?

ABSTRACT

In this work, thermal infrared (TIR) spectroscopy is used to refine and advance our understanding of the mineralogic composition of the Martian surface. The distinctiveness of glasses and phyllosilicates in TIR spectra is quantified using discriminant analysis and linear least squares modeling of numerical mixtures. Uncertainties in the modeled abundances of glasses and phyllosilicates are $\pm 15\%$ when the glass components in the mixture are included in the model, whereas uncertainties rise to $\pm 65\%$ when glass components are arbitrarily excluded from the model. When these uncertainties are applied to glass and phyllosilicate abundances on Mars derived from Thermal Emission Spectrometer (TES) data we find that glass is a likely component of the Martian surface. Spectral indexing and linear least squares modeling are used to compare laboratory-measured TIR emission spectra of Fo₉₁, Fo₆₈, Fo₅₃, Fo₃₉, Fo₁₈, and Fo₁ olivine samples to TES data and map the global distribution, composition, and abundance of olivine on Mars. Fo₉₁ spectral shapes are identified in the rims of the Hellas and Argyre impact basins. The Fo₆₈ and Fo₅₃ olivine spectral shapes are common in the southern highlands, chasmata, outflow channels, and are the most common compositions in the Nili Fossae region. The presence of the Fo₃₉ olivine composition suggests that olivine on Mars is more iron-rich than olivine in most Martian meteorites. The mineralogy, thermophysical properties, stratigraphy, and visual character of four locales in Terra Tyrrhena identified by different compositions of olivine (Fo₉₁, Fo₆₈, Fo₅₃, and Fo₃₉) are investigated. Fo₉₁-enriched materials occur as thin Noachian lava flows, perhaps associated with the Hellas impact basin. Fo₆₈-enriched materials are present throughout

Terra Tyrrhena, and in some places have interacted with liquid water at the end of the Noachian epoch; the presence of olivine constrains the total duration of aqueous activity during this period to $< \sim 20,000$ years. Fo_{53} and Fo_{39} -enriched materials are interpreted as Hesperian-aged lavas that erupted after the end of the Noachian aqueous activity. The settings of olivine-enriched materials suggest that surface materials in Terra Tyrrhena may have been more enriched in olivine before aqueous activity associated with the end of the Noachian epoch.

TABLE OF CONTENTS

| | |
|--|-----|
| Acknowledgments | iii |
| Abstract..... | iv |
| List of Tables..... | ix |
| List of Figures | x |
| | |
| Chapter 1. Introduction..... | 1 |
| | |
| Chapter 2. Discrimination of glass and phyllosilicate minerals in thermal infrared data ... | 6 |
| Abstract..... | 7 |
| 1. Introduction | 8 |
| 2. Analytical Approach..... | 10 |
| 2.1 Glass and phyllosilicate spectra..... | 10 |
| 2.2 Discriminant Analysis..... | 12 |
| 2.3 Generation of numerical mixtures | 13 |
| 2.4 The Deconvolution Algorithm..... | 15 |
| 2.5 Deconvolution analyses | 16 |
| 3. Results..... | 18 |
| 3.1 Discriminant Analysis..... | 18 |
| 3.2 One-component deconvolutions..... | 19 |
| 3.3 Two-component deconvolutions | 20 |
| 3.4 Four-component Deconvolutions | 23 |
| 3.5 Spectral Resolution Effects | 25 |
| 4. Discussion | 26 |
| 5. Application to Mars..... | 33 |
| 6. Conclusions | 35 |
| Acknowledgments | 38 |
| Tables..... | 39 |
| Figures | 41 |
| | |
| Chapter 3. The global distribution, composition, and abundance of olivine on the surface of Mars from thermal infrared data | 49 |
| Abstract..... | 50 |
| 1. Introduction..... | 51 |
| 2. Methods..... | 54 |

| | |
|--|-----|
| 2.1 Olivine Samples..... | 56 |
| 2.2 Spectral Index Analyses..... | 57 |
| 2.3 Linear Deconvolution Analyses | 60 |
| 2.4 Estimating the Detection Limit of Olivine..... | 64 |
| 2.5 Validation of Isolated Detections | 66 |
| 3. Results..... | 68 |
| 3.1 Spectral Index Analyses..... | 68 |
| 3.2 Deconvolution Analyses | 72 |
| 3.3 Distribution of Olivine with Latitude, Elevation, and Age..... | 79 |
| 4. Discussion | 82 |
| 4.1 Comparisons to Previous Work..... | 82 |
| 4.2 Implications of Latitude, Elevation, and Age Correlations..... | 87 |
| 4.3 Possible Origins of Olivine on Mars..... | 90 |
| 4.4 Comparison to a Model of the Martian Mantle..... | 94 |
| 5. Conclusions | 95 |
| Acknowledgments | 97 |
| Tables..... | 98 |
| Figures | 101 |
| | |
| Chapter 4. The geologic setting of olivine-enriched materials in Terra Tyrrhena..... | 115 |
| Abstract..... | 116 |
| 1. Introduction | 117 |
| 2. Data and Methods..... | 121 |
| 2.1 Instruments | 121 |
| 2.2 Data and Derived Products..... | 123 |
| 2.3 Study Site Selection | 132 |
| 3. Results..... | 133 |
| 3.1 Fo ₉₁ Study Area | 133 |
| 3.2 Fo ₆₈ Study Area | 137 |
| 3.3 Fo ₅₃ Study Area | 140 |
| 3.4 Fo ₃₉ Study Area | 143 |
| 4. Geologic Interpretation and Discussion..... | 145 |
| 4.1 Fo ₉₁ Study Area | 146 |
| 4.2 Fo ₆₈ Study Area | 148 |
| 4.3 Fo ₅₃ Study Area | 151 |
| 4.4 Fo ₃₉ Study Area | 152 |
| 4.5 Olivine in Terra Tyrrhena | 153 |
| 5. Conclusions | 157 |

| | |
|-------------------------------|------------|
| Acknowledgements | 159 |
| Tables | 160 |
| Figures | 161 |
| REFERENCES | 175 |

LIST OF TABLES

| | |
|--|-----|
| Chapter 2. | |
| Table 1. Abundances of components in four-component mixtures..... | 39 |
| Table 2. Wavenumber ranges and resolutions examined..... | 39 |
| Table 3. End member sets tested for each deconvolution analysis | 39 |
| Table 4. Relative positions on the discriminant function plane | 40 |
| Table 5. Deconvolution results for one-component mixtures | 40 |
| Chapter 3. | |
| Table 1. Sample, Fo-number, particle size, and source of olivine samples | 98 |
| Table 2. Wavenumbers (cm^{-1}) and channels for each index value..... | 98 |
| Table 3. Minerals that give high index values for each olivine index..... | 99 |
| Table 4. List of end-members used for deconvolution analyses | 100 |
| Chapter 4. | |
| Table 1. Percent abundances of mineral groups in the study area terrains..... | 158 |

LIST OF FIGURES

| | |
|---|-----|
| Chapter 2. | |
| Figure 1. Normalized emissivity spectra | 41 |
| Figure 2. Example analyses..... | 42 |
| Figure 3. Errors in models that exclude the phyllosilicate..... | 43 |
| Figure 4. Errors in models that exclude both the glass and phyllosilicate..... | 44 |
| Figure 5. Mean modeled abundances for four-component mixtures..... | 45 |
| Figure 6. Errors observed in models of four-component mixtures | 46 |
| Figure 7. Modeled abundances for four-component deconvolutions | 47 |
| Figure 8. Resolution effects on modeled results | 48 |
| Chapter 3. | |
| Figure 1. Thermal emission spectra of olivine samples..... | 101 |
| Figure 2. Position of bands used for olivine spectral indices..... | 102 |
| Figure 3. TES spectrum and models with varying amounts of olivine | 103 |
| Figure 4. Density distributions of index values vs. modeled olivine fractions | 104 |
| Figure 5. Index identifications of olivine..... | 105 |
| Figure 6. Mean fractional contribution maps of mineral classes | 106 |
| Figure 7. Total abundance and standard deviation of olivine | 107 |
| Figure 8. Individual abundance maps of olivine | 108 |
| Figure 9. Fo ₉₁ olivine occurrence in Argyre Planitia..... | 109 |
| Figure 10. Fo ₅₃ olivine occurrence in smooth-floored crater..... | 110 |
| Figure 11. Fo ₃₉ olivine occurrence in Noachis Terra | 111 |
| Figure 12. Fo ₁ occurrence near Hellas Basin | 112 |
| Figure 13. Density histogram of elevation of olivine-bearing pixels >5%..... | 113 |
| Figure 14. Density histogram of latitude of olivine-bearing pixels >5% | 114 |
| Chapter 4. | |
| Figure 1. Location of olivine-enriched study areas | 161 |
| Figure 2. DCS mosaic of the Fo ₉₁ study area..... | 162 |
| Figure 3. Flow features wrapping around a pre-existing knob | 163 |
| Figure 4. Dark-toned materials associated with olivine | 164 |
| Figure 5. Topographic profiles over Fo ₉₁ -enriched materials..... | 165 |
| Figure 6. DCS mosaic of the Fo ₆₈ study area..... | 166 |
| Figure 7. Sedimentary fan in Saheki Crater | 167 |
| Figure 8. Inverted topography of the fan and contact Saheki Crater's floor | 168 |
| Figure 9. DCS mosaic of the Fo ₅₃ study area..... | 169 |
| Figure 10. Palimpsest crater in the Fo ₅₃ study area | 170 |
| Figure 11. Fresh crater in the Fo ₅₃ study area | 171 |
| Figure 12. DCS mosaic of the Fo ₃₉ study area..... | 172 |
| Figure 13. Crater floor and Fo ₃₉ -bearing materials | 173 |
| Figure 14. Contact between light- and dark-toned units..... | 174 |

CHAPTER 1. INTRODUCTION

The overall purpose of this dissertation is to elucidate and refine our view of the mineralogy of Mars using thermal infrared (TIR) spectroscopy. Mars has undergone a host of geologic processes, many similar to those that occur on the Earth, that have transformed and been recorded by its surface. It harbors the largest shield volcanoes in the solar system, gigantic outflow channels, channel systems, a topographic dichotomy between the northern and southern hemispheres, evidence of platy flood lavas, and surfaces that look to have been exposed for over four billion years. The mineralogy of Mars provides insights into the chemistry and differentiation of Martian magmas, the conditions under which crystals formed, the eruptive processes that served as portals for lavas to reach the surface, and the resulting rocks' subsequent evolution due to weathering and/or erosion.

Although panchromatic and visible wavelength cameras have been flying to Mars since the first spacecraft arrived there in 1965, our quantitative knowledge of Martian mineralogy and geochemistry has relied almost exclusively on meteorites from Mars.

However, the number of Martian meteorites is relatively small (currently only 34 rocks) making it doubtful that they are able to represent the entire surface of Mars. Minerals have relatively distinct spectral signatures in TIR wavelengths (~5-50 μm) that occur because the wavelength-dependent thermal energy emitted from a material is representative of the strength and type of bonds contained in its molecules and mineral lattice structure. These TIR spectral signatures can be exploited to determine the mineralogy of a remote surface, and my dissertation focuses on using TIR remote sensing techniques to infer the mineralogy of the Martian surface from orbiting spacecraft. The primary advantage of using TIR remote sensing to determine the mineral makeup of the Martian surface is that it provides a global and quantitative measure of both the distribution and the abundance of minerals.

Although I use data from up to four different instruments, my dissertation primarily relies on data from the Thermal Emission Spectrometer. The TES instrument flew on board Mars Global Surveyor, which arrived at Mars in 1997, and revolutionized our view of Martian mineralogy. The TES instrument was a significant step forward in TIR technology in a Mars orbiter because of the wide range of wavelengths it measured (~5 to 50 μm) combined with a spatial resolution of 3 x 8 km, nearly two orders of magnitude higher than its predecessors, the Mariner 7 Infrared Spectrometer (IRS) and the Mariner 9 Infrared Interferometer Spectrometer (IRIS). The TES instrument has been used to unambiguously identify basalt and its components (feldspar, pyroxene, and olivine), hematite, quartzofeldspathic materials, and dacite on the Martian surface.

In the second chapter of this dissertation, I aim to distinguish glasses and phyllosilicate minerals in TIR data, and apply my findings to Mars. Previous workers have proposed that glasses and phyllosilicates have similar spectral shapes in TIR data, leading to ambiguity in their identification and derived abundances on Mars. The ambiguity is important to quantify because the presence of glass on the Martian surface suggests a primary igneous lithology that is relatively unweathered (glass breaks down relatively easily under weathering conditions), whereas phyllosilicates are the weathering products of igneous rocks. In this chapter I use discriminant analysis and linear least squares modeling of synthetic spectral mixtures that include glasses and phyllosilicates to determine the degree to which they can be distinguished in TIR data. I then empirically estimate the errors associated with deriving the abundances of glasses and phyllosilicates under laboratory conditions and in TES data. The estimated error bars are applied to linear least squares models of TES data performed by previous workers, and I conclude that glass, which is indicative of unweathered igneous rocks, is most likely present on the surface of Mars.

In chapters two and three I investigate the distribution, composition, abundance, and geologic settings of another primary igneous mineral used in the weathering debate, olivine. Olivine, $(\text{Mg, Fe})_2\text{SiO}_4$, is one of the first minerals to crystallize from of magmas at depth and olivine's Mg/Fe content can be used as a proxy for the composition of the magma from which it came. Like glass, olivine also breaks down relatively quickly in the presence of weathering agents (e.g., water) and its presence has been used to suggest the existence or lack of liquid water on the surface of Mars.

In chapter three, I investigate the global occurrence of olivine on Mars. I measure the thermal emission spectra of a series of olivine samples with varying Mg/Fe contents using the University of Hawaii's FTIR spectrometer. I identify spectral features characteristic of each composition of olivine in TES data via a simple mathematical tool called indexing, and I use the more robust method of linear least squares modeling to create maps of the abundance of each composition of olivine on the Martian surface. The maps are used to discuss the evolution of the Martian mantle and its surface with regards to chemistry and the timing of liquid water at the surface.

In the fourth chapter of my dissertation, I examine a few olivine-enriched locales identified by the work done in chapter three. I focus on the Terra Tyrrhena region of Mars, where olivine occurs with a large variety of compositions in a relatively small geographical area. I identify 25 olivine-enriched locales in the region and analyze in detail four sites displaying different olivine compositions using thermal infrared bolometer, hyperspectral, and multispectral data, visible images taken at multiple scales, and topographic data. I interpret the complex geology of each site and use them to build a cohesive view of the origin, evolution, and timing of the surface in Terra Tyrrhena.

Overall, the work presented here is a step towards gaining a more complete view of primary igneous phases observed in TIR data and on Mars. The error bars I estimate for glass and phyllosilicates, as well as the thermal emission spectra measured for different compositions of olivine, are applicable to both Earth- and Mars-based remote sensing data. The global olivine abundance maps for Mars have been made publicly available, and will perhaps be used by the authors of subsequent studies, especially those

who have not the will nor time to fully learn and develop TIR remote sensing techniques themselves. Finally, the detailed analyses of olivine-enriched locales serve as models for how mineralogy derived from TIR data can be used in conjunction with geomorphic and topographic data to build a cohesive interpretation of geologically interesting localities on Mars.

CHAPTER 2: DISCRIMINATION OF GLASS AND PHYLLOSILICATE MINERALS IN THERMAL INFRARED DATA

Published in its present form as Koeppen, W. C., and V. E. Hamilton (2005), Journal of Geophysical Research, 110, doi:10.1029/2005JE002474.

Abstract

Thermal infrared spectra of glasses and phyllosilicates have similar shapes leading to a proposed ambiguity in deconvolution results. We quantify the spectral separability of these two classes using discriminant analysis and linear deconvolution. We apply the deconvolution technique to single spectra, and two- and four-component mixtures. Missing end-members result in quantifiable uncertainties between modeled abundances of glasses and phyllosilicates. Mixtures containing silica-K₂O glass are susceptible to overestimating phyllosilicates with minimal increases in RMS error if the silica-K₂O glass spectrum is not present in the end-member set. Missing phyllosilicate end-members are likely to be modeled as combinations of other phyllosilicates rather than glasses, with saponite, nontronite, and halloysite showing the highest uncertainties. Empirically, $\pm 15\%$ of the total glass plus phyllosilicate abundance incorporates all uncertainties in derived glass abundance if the glass in the mixture is in the end-member set. If the glass in the mixture is excluded from the end-member set, these uncertainties increase to $\pm 65\%$. Four-component mixtures show that glasses and phyllosilicates act as a two-component mixing system but can induce small uncertainties in other components. Applying the maximum derived uncertainties to deconvolutions of surface type 2, measured by the Mars Global Surveyor Thermal Emission Spectrometer, we find that silica-K₂O glass abundance is above the instrument detection limit and a likely component of the surface. Pure silica glass, a proposed amorphous weathering product, is the least likely candidate for confusion with phyllosilicates and its non-inclusion in models of Martian spectra suggests it likely is not a component of the Martian surface.

1. Introduction

Glass and/or phyllosilicates are modeled in nearly all deconvolutions of Mars Global Surveyor Thermal Emission Spectrometer (MGS TES) data [*Bandfield et al.*, 2000b; *Hamilton et al.*, 2001; *Wyatt and McSween*, 2002; *McSween et al.*, 2003], and their identification on the Martian surface has important implications for the evolution of the planet's interior and exterior. The presence of phyllosilicates may suggest that water and weathering processes have acted at the surface whereas glass may imply a volcanic origin or alternate weathering style. However, discriminating between glasses and phyllosilicates has proven difficult because of the apparent spectral similarities of these classes [*Bandfield et al.*, 2000b; *Noble and Pieters*, 2001; *Minitti et al.*, 2002; *Wyatt and McSween*, 2002].

TES data suggest the presence of two global surface units on Mars distinguished primarily by their pyroxene and glass/phyllosilicate contents [*Bandfield et al.*, 2000b]. Surface type 1 consistently is interpreted as a basaltic mineralogy containing minimal glass (<10%) and low phyllosilicate (<~20%) abundance [*Bandfield et al.*, 2000b; *Hamilton et al.*, 2001; *Wyatt and McSween*, 2002; *McSween et al.*, 2003]. The interpretation of surface type 2, however, has varied. Initial deconvolution of the surface type 2 spectrum, using an end-member set including both glasses and phyllosilicates, indicated that this surface type is best modeled by a basaltic andesite to andesite-like mixture of minerals composed of feldspar, glass, clinopyroxene, and phyllosilicates – the latter two mineral classes being at or below TES detection limits [*Bandfield et al.*, 2000b]. *Wyatt et al.* [2001] selected an end-member set containing only primary igneous

mineralogies designed to distinguish between basalt and andesite, which was used by *Hamilton et al.* [2001] to model the surface type 2 spectrum. They obtained a spectral fit with only a slightly higher root-mean-squared (RMS) error than that of *Bandfield et al.* [2000] and supported the hypothesis of *Bandfield et al.* [2000] that surface type 2 was higher in silica than surface type 1.

Wyatt and McSween [2002] suggested that similarities between the spectra of glasses and some phyllosilicates might complicate discrimination between these classes in deconvolutions of Martian spectra. Using an end-member set that excluded glasses, they again deconvolved the surface type 2 spectrum and also obtained a reasonable fit based on a relatively low RMS error. Their best-fit model included large abundances of phyllosilicates (~30%) and K-feldspar (~15%), a result that, along with the geographic distribution of the surface type 2 spectral shape, was interpreted to suggest that the surface type 2 spectrum represents a weathered basaltic lithology. *Wyatt and McSween* [2002] concluded, however, that the best fits in terms of RMS error are obtained when both glasses and phyllosilicate end-members are used to model the surface.

To date, no quantitative work has demonstrated to what degree glasses and phyllosilicates may or may not be distinguished. The best fit to the surface type 2 spectrum is achieved using both glasses and phyllosilicates, but reasonable fits can be obtained using only glasses or only phyllosilicates. Because two interpretations of the TES data are thus possible, it is important to establish the separability of the classes as well as the relative abundances and chemistries of mixtures that aggravate difficulties in discrimination.

In this study we apply discriminant analysis, a multivariate technique, to glass and phyllosilicate spectra to judge the statistical separability of the two classes. We then use an end-member set confined to glass and phyllosilicate spectra, a series of numerical mixtures of those spectra, and a linear deconvolution algorithm to analyze the empirical problems associated with discriminating between glasses and phyllosilicates. We quantify the spectral similarities and differences of glasses and phyllosilicates, determine the conditions and combinations of these classes that affect abundance estimation, and develop a maximum range of uncertainties for deconvolution results that include or exclude these classes in the end-member set. Four-component mixtures include glass, phyllosilicate, feldspar, and pyroxene to simulate mafic igneous rocks. These are used to ascertain (1) if errors in discrimination identified in glass-phyllosilicate mixtures deteriorate in the presence of other phases, and (2) if ambiguity in glass and phyllosilicate discrimination affects the deconvolved abundances of other phases present in a mixture. Finally, we apply the derived uncertainties to deconvolution results from TES data and make inferences about the nature of the Martian surface from our results.

2. Analytical Approach

2.1 Glass and phyllosilicate spectra

Emissivity spectra of two glasses [Wyatt *et al.*, 2001] and seven granular phyllosilicate minerals were selected from the Arizona State University (ASU) spectral library [Christensen *et al.*, 2000b] (Figure 1). The two glass spectra are used commonly in Mars remote sensing end-member sets [e.g. Hamilton *et al.*, 2001; Wyatt *et al.*, 2001].

The silica-K₂O glass is 77.9% SiO₂, 12.6% Al₂O₃, 5.67% K₂O, and 3.90% Na₂O, and has spectral features that match well with natural samples of obsidian and pumice [e.g., *Crisp et al.*, 1990; *Ramsey and Fink*, 1999]. The pure silica glass is 99.99% SiO₂, and its spectrum has a similar shape to that of the silica-K₂O glass but shows emissivity minima shifted towards higher wavenumbers [*Wyatt et al.*, 2001]. Minima of the pure silica glass match many natural and synthesized samples of amorphous silica proposed to be present on Mars [*Kraft et al.*, 2003; *Michalski et al.*, 2003]. The phyllosilicate spectra selected represent three of the five major classes of layered “clay minerals”, kaolinite, illite, and smectite [*Deer et al.*, 1992]. The illite and smectite classes, in particular, resemble near-infrared spectral properties of the Martian surface and are the most likely weathering products to be found on Mars [*Toulmin et al.*, 1977; *Gooding et al.*, 1991; *Bishop et al.*, 1993; *Bishop and Pieters*, 1995].

Though similarities between glasses and phyllosilicate minerals exist in thermal emission spectra, there are differences as well. Examination of the spectra show that precise locations of the Christiansen feature and emissivity minima in the 1300 – 900 cm⁻¹ region of phyllosilicate minerals are 20 – 45 cm⁻¹ less than in the silica-K₂O glass spectrum and 50 – 75 cm⁻¹ less than in the pure silica glass spectrum (Figure 1). Phyllosilicate minerals also display a shallower emissivity minimum at 1300-900 cm⁻¹ than at 465 cm⁻¹ whereas glasses show the opposite trend. Additionally, five of the seven phyllosilicate minerals tested here show an emissivity minimum at 500 – 570 cm⁻¹ that is absent in both glass spectra; however, this region commonly is excluded from deconvolutions of TES data because of strong atmospheric CO₂ absorptions.

2.2 Discriminant Analysis

Discriminant analysis is a multivariate technique that quantifies the separability of known populations, in our case the spectra of glasses and phyllosilicates, based on linear functions of the variables [Rencher, 1995]. The discriminant function describes a plane onto which the original, multivariate spectra can be projected to maximize the distance between the spectral features unique to glasses and phyllosilicates. The vector of coefficients resulting from the analysis is the same length as the input spectra, and when applied to each input spectrum, describes the position of each spectrum with a single value along the plane. The absolute positions are unimportant and will be different for each series of spectra; however, the relative positions indicate how close spectra are along a line describing their maximum separation, the linear discriminant function. We normalized the resulting positions so that most dissimilar spectra have values of zero and one, and all other spectra fall in between. Although discriminant analysis is not directly applicable to deconvolution analysis (which does not use a projected axis to separate end-members), it gives a statistical indication of the separability of glass and phyllosilicate spectra. Linear discriminant analysis may be applied to more than two spectral classes [e.g., Hochberg and Atkinson, 2003] and a full description of the technique is found in Rencher [1995].

2.3 Generation of numerical mixtures

We linearly combined the spectra of glasses and phyllosilicates to generate numerical mixtures. The assumption of linear mixing in thermal infrared data is well documented [*Crown and Pieters, 1987; Thomson and Salisbury, 1993; Ramsey and Christensen, 1998; Hamilton and Christensen, 2000*] and allows for rapid generation and analysis of many mixtures of known composition. *Ramsey and Christensen [1998]* tested the linear deconvolution technique with numerical and physical mixtures and demonstrated that areal mineral abundances may be predicted with both methods to within 4% average absolute error. In our study, the use of numerical mixtures eliminated significant time expenditure for mixture preparation and characterization, and dramatically increased the total number of analyses performed.

Because we analyzed spectral rather than physical mixtures, we do not address issues related to particle size effects that may be relevant under certain conditions, such as the presence of fine phyllosilicate grains clinging to larger glass or mineral grains. Particle size effects may include reduction of spectral contrast, and introduction of transparency features at small particle sizes [*Hunt and Vincent, 1968; Vincent and Hunt, 1968; Salisbury, 1993*], and we do not account for these phenomena in this study. The “granular” phyllosilicate spectra we selected are from minerals mixed in a wet slurry, desiccated, and broken into small clods [*Piatek, 1997*]. The results we obtain should be appropriate for application to deconvolutions of Martian dark regions, which do not display spectral effects attributed to the presence of fine particulates [*Ruff and*

Christensen, 2002] and typically are thought to contain coarse particles and lag deposits [*Christensen and Moore, 1992*].

The two glasses used are of approximately the same spectral contrast, but show much deeper features than phyllosilicates. Changes in the spectral contrast of components in an unknown mixture or in the end-member set may affect identification and abundance determination, a problem beyond the scope of this study. We generated mixtures and tested end-member sets composed of commonly used spectra without normalization or other contrast-altering techniques.

Our two-component mixtures included one glass and one phyllosilicate spectrum making 14 unique pairs of glasses and phyllosilicates. We added the phases together in the following proportions (glass:phyllosilicate): 90:10, 80:20, 70:30, 60:40, 50:50, 40:60, 30:70, 20:80, 10:90. This provided us with nine mixture spectra for each glass and phyllosilicate pair for a total of 126 mixtures.

We generated four-component mixtures that included glass, phyllosilicate, pyroxene, and feldspar to determine the effect of additional phases on deconvolution results. We used an augite from the ASU spectral library as it is the most abundant pyroxene deconvolved in basaltic rocks and also is common in andesite and dacite [*Wyatt et al., 2001*]. Feldspar minerals also are found in basaltic and andesitic rocks. We chose labradorite (plagioclase feldspar) to represent the feldspar component in these mixtures as it is an intermediate composition commonly found in terrestrial basalts and deconvolution results from both Martian surface types [*Milam et al., 2004*]. Four-component mixtures provided a large number of possible abundance configurations so we restricted them

using two ratios of glass and phyllosilicate (Table 1). Each set of mixtures contained two spectra bearing more glass than phyllosilicate and two spectra bearing less glass than phyllosilicate. These were coupled with another ratio, total glass and phyllosilicate abundance greater than and less than total pyroxene and feldspar abundance, yielding four combinations for each glass/phyllosilicate pair.

2.4 The Deconvolution Algorithm

The linear deconvolution technique we used for analyzing emission spectra is described by *Ramsey and Christensen* [1998] with modifications by *Bandfield et al.* [2000] and has been used by several investigators [*Hamilton et al.*, 1997; *Feely and Christensen*, 1999; e.g. *Bandfield et al.*, 2000b; *Christensen et al.*, 2000c; *Wyatt et al.*, 2001; *McSween et al.*, 2003; *Milam et al.*, 2004; *Staid et al.*, 2004]. The technique relies on the concept that the spectrum of a mixture is a linear combination of the spectra of its component phases, in proportion to their abundance. The algorithm uses a set of end-member spectra, in our case represented by glass and phyllosilicate spectra, to perform a least squares fit to the spectrum of the unknown mixture. The program iteratively removes end-members with negative concentrations until all concentrations are positive or zero. Upon obtaining a fit, the algorithm produces a best-fit model spectrum and the abundance of each end-member used in the model.

The quality of the model fit and resultant mineralogy can be evaluated by the degree of difference between the model-derived spectrum and the mixture spectrum both visually and by the RMS error provided by the algorithm, presented in this study as the

RMS value [*Hamilton et al.*, 1997; *Ramsey and Christensen*, 1998; *Feely and Christensen*, 1999; *Hamilton and Christensen*, 2000]. However, though RMS errors are useful for comparing different model spectra of a particular mixture (for instance, resulting from different end-member sets), they cannot be used to compare the goodness of fit between different mixture spectra because the RMS error calculation is dependent on the overall spectral contrast of mixture components, the spectral resolution of the unknown mixture, and the signal to noise ratio.

Variations in the contrast of thermal infrared spectra have been shown to result from particle size-effects [e.g. *Aronson et al.*, 1966; *Salisbury and Wald*, 1992; *Moersh and Christensen*, 1995; *Mustard and Hays*, 1997; *Hamilton*, 2003] and spectra in an unknown mixture may not be of the same spectral contrast as those in the end-member set. For our study of numerical mixtures this was not the case. However, to simulate deconvolutions of actual surface data we included a blackbody spectrum – unit emissivity at all wavelengths – in all end-member sets provided to the deconvolution algorithm. The blackbody spectrum effectively adjusts the contrast of input end-members so that they can more closely match those in the mixture spectrum [*Hamilton et al.*, 1997].

2.5 Deconvolution analyses

We deconvolved our numerical mixture spectra using multiple spectral resolutions and wavenumber ranges in order to examine their effects on the resulting model abundances (Table 2). We used laboratory spectral sampling, TES spectral sampling with a typical atmospheric CO₂ region removed [*Bandfield et al.*, 2000b;

Christensen et al., 2000c; Hamilton et al., 2001], and TES spectral sampling with a narrowed CO₂ region removed [*Ruff, 2003*]. For simplicity, unless otherwise stated all figures and analyses shown represent mixtures with TES spectral sampling with a typical atmospheric CO₂ region removed. Performing the analysis at several resolutions quantifies the change in model error as a function of spectral resolution and wavenumber coverage, however, the narrowed CO₂ exclusion range tested here typically is only applicable to non-atmospherically-corrected TES data. We did not consider effects of signal-to-noise ratio on the deconvolution results.

Table 3 outlines the end-member sets tested for each deconvolution analysis. We first applied the deconvolution algorithm to individual glass and phyllosilicate spectra in one-component deconvolutions. These analyses provided empirical information on the mathematical similarity of an individual spectrum to the other spectra in the set, and we tested four scenarios at each spectral resolution: the algorithm was provided with an end-member set including (1) all glass and phyllosilicate spectra, (2) only glass spectra, (3) only phyllosilicate spectra, and (4) all glass and phyllosilicate spectra except the specific spectrum being modeled, for a total of 108 models.

We deconvolved two-component mixtures using three sets of end-members, including: (1) all glass and phyllosilicate spectra, (2) all glass and phyllosilicate spectra except for the specific phyllosilicate spectrum in the mixture being modeled, and (3) all glass and phyllosilicate spectra except the specific glass and phyllosilicate spectra present in the mixture spectrum. We do not report on the scenario where the specific glass spectrum in the mixture was excluded from the end-member set because these results

were similar to those that excluded both the glass and phyllosilicate, likely resulting from the limited number of glass spectra in our end-member set. We also do not show cases using end-member sets that include all possible end-member spectra, including those in the spectrum being modeled, as these models perfectly reproduce known abundances and have RMS errors of zero.

Deconvolutions of 168 four-component mixtures tested the same three end-member scenarios as the two-component mixtures. Additionally, the end-member set always included the correct feldspar and pyroxene spectra as the focus of this study was on the modeling of glass and phyllosilicate spectra.

3. Results

3.1 Discriminant Analysis

Table 4 lists the normalized positions of each spectrum projected onto the plane described by the discriminant function, in ascending order. We found that there was no statistical overlap between glass and phyllosilicate spectra. Furthermore, phyllosilicates are shown to be statistically closer to each other than to glasses, and statistically closer to the silica-K₂O glass than the pure silica glass. We do not show the positions of mixtures of glasses and phyllosilicates, but they follow the linear discriminant function in regular, linear increments as would be expected. For example, a mixture of 50% silica-K₂O glass and 50% illite is positioned at 0.303, halfway between the values for pure silica-K₂O glass and illite.

3.2 One-component deconvolutions

Our results for one-component deconvolutions are shown in Table 5. In five of nine cases in which the algorithm was provided with only end-member spectra other than the one being modeled, glasses were selected to partially model phyllosilicate spectra and vice versa. Table 5 shows the abundance of glass contributing to each model of an individual spectrum, the remaining abundances are made up of phyllosilicates. For example, the pure silica glass spectrum contributed only ~24% to the model of the silica-K₂O glass spectrum if the silica-K₂O glass spectrum was not included in the end-member set. Multiple phyllosilicate spectra (dominated by saponite and kaolinite) combined to produce the remaining ~76% of the silica-K₂O glass model. On the other hand, the pure silica glass spectrum was modeled exclusively by the silica-K₂O glass spectrum. Models of phyllosilicates always were modeled dominantly by other phyllosilicates; however, glass spectra were used to model phyllosilicate spectra up to 11%. The model of illite showed the highest contribution from glass end-members (~4% silica-K₂O glass and ~7% pure silica glass), but glass also was included in models of saponite, Ca-montmorillonite, and kaolinite. In the latter three cases the silica-K₂O glass spectrum was the only contributing glass phase.

Providing the algorithm with only glass end-members elevated the RMS errors for all models of phyllosilicates as well as the silica-K₂O glass over models that allowed both glasses and phyllosilicates in the end-member set. The greatest increase in RMS error for the glass-only end-member set was exhibited by nontronite.

Providing the algorithm with only phyllosilicate end-members (but not the spectrum being modeled) elevated the RMS errors for models of silica-K₂O glass, pure silica glass, illite, and Ca-montmorillonite over those that allowed both glasses and phyllosilicates in the end-member set. Models of phyllosilicate spectra used a variety of phyllosilicate end-members rather than any one in particular. Models for both glass spectra included almost entirely illite, though visual examination revealed that these fits obviously were poor.

Models of saponite and kaolinite showed almost no change in RMS error at the reported precision when provided with only phyllosilicate end-members, even though they included glass end-members if provided with them. Comparing models of the silica-K₂O glass spectrum revealed that only a slight increase in RMS error was associated with deconvolving the spectrum with only the pure silica glass over deconvolving it with only phyllosilicates.

3.3 Two-component deconvolutions

We deconvolved 9 mixture ratios for 14 glass-phyllosilicate spectral pairs across 3 different wavelength ranges, providing 378 two-component spectral mixtures. Figure 2 shows example analyses for mixtures containing silica-K₂O glass and nontronite, and pure silica glass and Fe-smectite. For each mixture spectrum (black) we show two model results. Red spectra represent models that excluded the phyllosilicate in the mixture from the end-member set, and the worst fits were achieved when the missing phyllosilicate was a large component in the mixture. Blue spectra represent models that excluded both the

glass and the phyllosilicate in the mixture from the end-member set and the worst fits were achieved when glass was a large component in the mixture. Glasses, with their strong spectral contrast relative to phyllosilicates, dominate the error spectra (measured – modeled) when that phase is missing from the end-member set, and misfits of the model to the mixture are obvious in all models that exclude glass present in the mixture from the end-member set.

Deconvolved abundances for models using end-member sets that excluded the specific phyllosilicate spectrum in the mixture are shown in Figure 3. In these models, the specific glass in the mixture was included in the end-member set. We defined the error in glass determination as the known glass abundance subtracted from the modeled glass abundance. Figure 3 shows that models of mixtures containing illite and saponite overestimate the glass abundance whereas models of mixtures containing nontronite and kaolinite underestimate the glass abundance. Models of mixtures containing Fe-smectite, Ca-montmorillonite, and halloysite both over- and underestimate the glass abundance.

Nontronite, saponite, kaolinite, and halloysite show trends when combined with either glass such that as glass abundance in the mixture increases, the error in glass determination first increases and then decreases. The maximum error in these models occurs when 30 to 60% of the mixture is a glass end-member. Models of mixtures containing illite and Ca-montmorillonite show a different trend where errors in glass abundance only decrease with increasing glass abundance. Models of mixtures containing Fe-smectite show an increasing then decreasing error in glass determination when paired with pure silica glass, but only decreasing error in glass determination with

glass abundance when paired with silica-K₂O glass. Most two-component models that excluded the specific phyllosilicate spectrum in the mixture from the end-member set estimated total glass abundance to within ~12%. Deconvolution results from mixtures containing nontronite showed the largest errors in modeled glass abundance, up to 19%.

Deconvolution results from models that excluded both the specific glass and phyllosilicate spectra in the mixture are shown in Figure 4. Virtually all models of mixtures containing silica-K₂O glass underestimated glass abundance in the mixture, and they show a relatively simple trend between increasing error in glass determination with increasing glass abundance in the mixture. Mixtures containing the pure silica glass almost always overestimated the glass abundance in the mixture, and they show a trend in which the error in glass determination increases quickly and then sharply decreases with increasing glass in the mixture. This trend occurs because models of mixtures containing pure silica glass greatly overestimate the total glass abundance. The error in glass abundance first increases with glass abundance in the mixture showing that glass is increasingly overestimated. In mixtures that contain more than 50% pure silica glass the modeled abundance of silica-K₂O glass is reported to be 100%, and the error in modeled glass abundance decreases as the glass abundance in the mixture approaches the glass abundance in the model.

Mixtures of pure silica glass and nontronite show the least error in glass determination (<~40%) followed by models of mixtures containing Fe-smectite and kaolinite. Other phyllosilicates paired with the pure silica glass show errors in glass determination up to ~60%. In all deconvolution results, the RMS error increased from

models excluding the phyllosilicate from the end-member set to models excluding both the glass and the phyllosilicate from the end-member set. This was especially true for models of mixtures containing pure silica glass, which has the strongest spectral contrast we tested.

3.4 Four-component Deconvolutions

Averaged four-component deconvolution results for two of the end-member sets tested are shown in Figure 5. Cases that exclude the phyllosilicate in the mixture from the end-member set show $< \sim 4\%$ absolute fraction (AF) difference from the known abundances; the worst case is exhibited by pure silica glass mixtures that contain 50% phyllosilicate. Cases that exclude both the glass and the phyllosilicate in the mixture from the end-member set have large errors in glass and phyllosilicate determination.

Figure 6 shows the mean errors and standard deviation in glass determination for end-member sets that exclude the phyllosilicate, and both the glass and phyllosilicate, in the mixture from end-member sets. Models that exclude the phyllosilicate in the mixture from the end-member set show low and relatively invariant mean errors. Mean errors are $< \pm 3\%$ (AF) and fall within the $\pm 12\%$ relative fraction (RF) determined for glass in the two-component deconvolutions. Almost all errors (applying the maximum standard deviation) are $< \pm 7\%$ (AF). Like the two-component results, the modeled abundance of glass is both over- and underestimated for this end-member case.

Models that exclude both the glass and phyllosilicate spectra in the mixture from the end-member set severely miscalculate the total glass content. For this case, mean

errors in glass determination increase with increasing glass abundance in the mixture and they fall within 70% (RF) of the known glass abundance. As with the two-component results, models of silica-K₂O glass mixtures always underestimate glass abundance whereas models of pure silica glass mixtures always overestimate the glass abundance. In both end-member scenarios – excluding the phyllosilicate, or both glass and phyllosilicate in the mixture – the standard deviation of modeled results increases with increasing phyllosilicate abundance in the mixture. Correspondingly, the largest standard deviation occurs when glass plus phyllosilicate is greater than pyroxene plus feldspar, and the phyllosilicate abundance is higher than that of glass.

The error in glass determination is a useful parameter for estimating the uncertainty in glass abundance, however, it does not reveal how glass and phyllosilicate change relative to each other. Figure 7 shows the distribution of modeled abundances for glass and phyllosilicate in all four-component mixtures we tested. In general, models within a particular mixture configuration that report glass abundance higher than the known also report phyllosilicate abundance lower than the known and vice versa. This generates the linear trends of glass and phyllosilicate abundances seen in Figure 7. These trends roughly follow a line between having the total amount of glass and phyllosilicate in the mixture modeled as exclusively glass or phyllosilicate. For example, in Figure 7a this trend would be a line between 0% glass, 70% phyllosilicate and 70% glass and 0% phyllosilicate. Deviations from this trend are mixtures that over- or underestimate feldspar and/or pyroxene in addition to glass and phyllosilicate. In cases that excluded both the glass and phyllosilicate in the mixture from the end-member set (closed symbols,

Figure 7), models of silica-K₂O glass mixtures underestimated pyroxene and models of pure silica glass mixtures underestimated feldspar.

3.5 Spectral Resolution Effects

Figure 8 shows the mean errors in glass determination from two-component deconvolution results. This presentation is similar to Figure 6, but plots each glass-phyllsilicate pair rather than the means and standard deviations. The horizontal axis summarizes cases that exclude the phyllosilicate in the mixture from the end-member set, and the vertical axis summarizes cases that exclude both the glass and phyllosilicate in the mixture from the end-member set. The three resolutions described in Table 2 are plotted for each mean error value. All model results show slight differences between the ranges, and the maximum difference is 10% (AF). Most mean errors varied by less than 4% (AF) along either axis, regardless of resolution. Although some cases showed lower mean errors for the mixtures with laboratory spectral sampling, most models showed the TES spectral sampling with a narrowed CO₂ exclusion to be the best range to use, especially for mixtures containing pure silica glass. The typical TES range had the highest mean errors for both end-member scenarios indicating the worst abundance estimations of the three resolutions tested. RMS errors varied slightly for models of a particular mixture at different resolutions, but there was no overall trend relating RMS errors to the spectral sampling. RMS errors fell within 20% of the maximum RMS value for a given mixture.

4. Discussion

Our discriminant analysis of common glass and phyllosilicate spectra showed statistical differences between the two classes. The lack of overlap on the linear discriminant plane suggests that although glass and phyllosilicate spectra may appear similar visually, statistical separability of the spectra exists and may be exploited by the linear deconvolution algorithm. Furthermore, our analysis indicates that phyllosilicate spectra numerically are closer to the silica-K₂O glass than to the pure silica glass.

When provided with all possible end-member spectra, the deconvolution algorithm always produced models with the correct end-members and abundances in the mixture. This was expected to occur because the end-member set contained the exact spectra used to construct the mixture and perfect optimization (an RMS error of zero) was possible.

One-component model results are not directly applicable to most thermal infrared data, but, like the discriminant analysis, demonstrate how similar the normalized emissivity shapes of end-members are to each other. Pure silica glass was modeled exclusively by silica-K₂O glass indicating that the silica-K₂O glass spectral shape is its closest match. Therefore, pure silica glass is not likely to be modeled by phyllosilicates if the silica-K₂O glass end-member is available the pure silica is not. On the other hand, the silica-K₂O glass spectrum is modeled with 76% phyllosilicates and only 24% glass indicating that the silica-K₂O glass spectrum has an overall shape more akin to a combination of phyllosilicates than to the pure silica glass. Although phyllosilicates dominantly can model the silica-K₂O glass when silica-K₂O glass is not in the end-

member set, the reciprocal does not seem to be true. None of the phyllosilicate models included more than 11% glass (found in models of illite) suggesting that phyllosilicate spectra are spectrally and thus numerically most similar to other phyllosilicate spectra rather than either glass spectrum. This result indicates that the silica-K₂O glass spectrum is more susceptible to being modeled by the phyllosilicate spectra than the phyllosilicate spectra are to being modeled by the silica-K₂O glass spectrum, and that if any glass may be present, glass end-members should be included in deconvolutions. Many of the one-component deconvolution results corroborate those of the discriminant analysis, which predicted both the similarity of the pure silica glass to the silica-K₂O glass and the similarity of phyllosilicates to each other. However, the susceptibility of the silica-K₂O glass being modeled by phyllosilicates and the glass abundances found in models of illite were not predicted, and these inconsistencies likely result from using a projected axis (which most accurately separates the spectral shapes) for the discriminant analysis and the wavenumber axis for the deconvolution analysis.

The numerical separation of phyllosilicates, silica-K₂O glass, and pure silica glass primarily stems from differences in the emissivity minima of the spectra. The deconvolution algorithm can model variations in depth of emissivity minima (e.g. via abundance) but cannot model shifts in the wavenumber position of those minima. The silica-K₂O glass has an emissivity minimum between those of the pure silica glass and phyllosilicates in the 1300 – 900 cm⁻¹ region that is closer to the phyllosilicate minima than it is to the minimum of the pure silica glass. The relative depths of emissivity minima also contribute to a spectrum's separability because one band minimum cannot

be shallowed independently of another. In glasses, the 1300-900 cm^{-1} emissivity minima are deeper than 465 cm^{-1} minima, a trait most evident in the pure silica glass (Figure 1) and opposite of most phyllosilicates. Fitting both the specific emissivity minima positions and their relative depths is important in order for the algorithm to minimize RMS error. For both spectral feature types, phyllosilicates are closer to the silica-K₂O glass than to the pure silica glass, and the pure silica glass is closer to the silica-K₂O glass than to phyllosilicates. This explains the relatively high abundances of phyllosilicates reported in deconvolutions of silica-K₂O glass and why illite showed the highest modeled abundance of glass. The illite spectrum has a spectral “shoulder” on the high wavenumber side of the main emissivity minimum that is matched in the silica-K₂O glass spectral shape and also has a 465 cm^{-1} emissivity minimum only slightly deeper than the 1300-900 cm^{-1} minimum.

No single end-member spectrum was modeled exclusively by end-members of another class unless they were forced to do so by manipulating the end-member set. All analyses that forced end-members of a different class into the deconvolution resulted in increased the RMS error, but in some cases, silica-K₂O glass in particular, the increase was relatively small over using only end-members of the same class. Again, this results from the emissivity minimum of the silica-K₂O glass in the 1300 – 900 cm^{-1} region being closer to minima in phyllosilicate spectra than to the minimum of pure silica glass. This shows that RMS errors obtained by deconvolving the silica-K₂O glass are not necessarily a good indicator of the algorithm’s determination of total glass abundance. With only one glass in the end-member set, results range from 100% glass (correct) to 100%

phyllosilicates (incorrect) with only a minimal change in RMS error. Visual inspection of the original data and the model, however, can give a good indication of the quality of fit. Although the RMS error may seem relatively small, characteristic parts of the spectrum ($1050 - 1200 \text{ cm}^{-1}$ and $400 - 500 \text{ cm}^{-1}$) are misfit if end-members are missing, a fact especially true of the glasses (Figure 2).

Of the three end-member sets used to deconvolve the two component models (including all end-members, excluding the phyllosilicate in the mixture, and excluding both the glass and the phyllosilicate in the mixture), two may have direct application to deconvolving unknown mixture spectra. The end-member set that excludes the phyllosilicate in the mixture from the end-member set tests the case that emissivity spectra of components in an unknown mixture are likely to have minima that fall on or between those of end-members provided to the deconvolution algorithm. Removal of the phyllosilicate spectrum in the mixture from the end-member set forces the algorithm to compensate for not being able to fit an exact model to the mixture. Two-component deconvolution results suggest that glass and phyllosilicate spectra are separable, showing errors in modeled glass abundance less than 19% (AF) as long as the correct glass is included in the end-member set.

The scenario that excludes both the glass and phyllosilicate in the mixture from the end-member set tests a case in which glasses and phyllosilicates in an unknown mixture may both be different from the spectra in the end-member set. If a glass in a mixture has a different composition than the silica-K₂O glass here and its $1300\text{-}900 \text{ cm}^{-1}$ region emissivity minimum is shifted to higher wavenumbers, it almost certainly will be

modeled entirely by the silica-K₂O glass spectrum as we observed in mixtures containing pure silica glass. In these cases the error in modeled glass was substantial, overestimating the total glass content by ~60% (AF). Although silica-K₂O glass was overestimated for mixtures containing pure silica glass, errors were obvious based on difference spectra and high RMS errors relative to models that included the correct glass end-member. If glasses in an unknown mixture are significantly different from those in the spectral library and the 1300-900 cm⁻¹ region emissivity minimum is shifted to lower wavenumbers, or the 600-400 cm⁻¹ minimum shows major differences such as a broadening, there could be cross-substitution between the glass and phyllosilicate spectral shapes in models produced by deconvolution. In this case, the reported abundances of other silicates also will be affected.

Four-component models tested the complexity of spectral discrimination in cases more like those found in typical geologic mixtures and helped us to examine the situation in which glass or phyllosilicates are not the dominant spectral shapes in a mixture. Four-component deconvolution results showed only small errors in modeled abundances of all phases (glass, phyllosilicate, pyroxene, and feldspar) in cases where only the specific phyllosilicate spectrum used to make the mixture was removed from the end-member set. This duplicated the results from the two-component deconvolutions. All modeled abundances of glass and phyllosilicate fell within 10% (AF) of the correct value when the mixture contained 50% glass and 20% phyllosilicate. Modeled abundances for glass and phyllosilicate were within 8% (AF) in mixtures containing 20% glass and 10% phyllosilicate. Like the two-component deconvolutions, nontronite combined with either

glass showed the highest uncertainties in glass and phyllosilicate abundances whereas models of mixtures containing illite, Ca-montmorillonite, Fe-smectite, and kaolinite estimated glass and phyllosilicate abundances within 2% (AF). Also similar to the two-component results, uncertainties were higher for cases in which both the glass and the phyllosilicate in the mixture were removed from the end-member set.

For the most part, modeled abundances from end-member sets excluding the phyllosilicate, and excluding both the glass and the phyllosilicate, in the mixture follow a roughly linear trend (Figure 7). This trend corresponds to a mixing system between the total glass and phyllosilicate abundance in the mixture being modeled completely by either glass or phyllosilicate. This shows that, to first order, there is little exchange between feldspar and pyroxene, and glass and phyllosilicate. This suggests that the pyroxene and feldspar components are not affected significantly by the lack of correct glass or phyllosilicate spectra in the end-member set. Glass and phyllosilicate spectra appear to act as a two-component mixing system and therefore the uncertainties calculated in our two-component analyses can be applied relatively to modeled abundances in unknown mixtures.

Based on the total amount of glass plus phyllosilicate present in the mixture, an empirical relationship can be approximated to calculate the uncertainty in modeled abundances for the two- and four-component models that exclude the phyllosilicate in the mixture from the end-member set. For glass, $\pm 15\%$ of the total glass plus phyllosilicate abundance accommodates all of the uncertainty in glass abundance reported by our deconvolution algorithm. For example, a mixture containing 30% glass and 10%

phyllosilicate would have an uncertainty in modeled glass abundance (exchanging mostly with phyllosilicate) of $\pm 6\%$. Phyllosilicate uncertainties do not exactly follow the same type of trend, however, they can be roughly estimated as $\pm 20\%$ of the total glass plus phyllosilicate abundance for over 80% of our data, and a more conservative estimate of $\pm 35\%$ incorporates 100% of our data. If both glass and phyllosilicates in an unknown mixture are different than those in the end-member set, maximum uncertainties increase to $\pm 65\%$ for glass, and $\pm 70\%$ for phyllosilicates. For the example mixture containing 30% glass and 10% phyllosilicate, this amounts to $\pm 26\%$ for modeled glass abundances and $\pm 28\%$ for modeled phyllosilicate abundances, again, exchanging mostly for each other.

In models of mixtures containing the pure silica glass spectrum and excluding both the glass and phyllosilicate in the mixture from the end-member set, glass abundance was overestimated to the point of removing phyllosilicates from the deconvolved abundances in all but one mixture. However, mixtures containing the silica-K₂O glass were never modeled exclusively by phyllosilicate or glass and almost always underestimated the total glass abundance.

The spectral resolution of the input spectra slightly changed the separability of glasses and phyllosilicates, independent of the end-member set used, and the TES spectral range with a typical CO₂ region removed was found to be the worst. Those spectra exclude a large wavenumber region including an emissivity minimum at 500 – 550 cm⁻¹ that is present in phyllosilicates and not glasses. Intuitively we might expect the laboratory spectral sampling to be the best, however, 2 cm⁻¹ sampling appears to

degrade the modeled abundances. This probably results from the inclusion of spectral structure in the 2 cm^{-1} resolution data (i.e., noise) that is effectively smoothed at 10 cm^{-1} sampling (we did not account for the lower signal-to-noise of the TES instrument relative to laboratory data). The TES spectral range with a narrowed CO_2 region removed benefits from including the $500 - 550\text{ cm}^{-1}$ and having smoother spectra, however, since these differences are small, improvement in modeled abundances is also small ($\sim 4\%$).

5. Application to Mars

We demonstrate the application of our empirically derived relationships using the deconvolution results of *Bandfield et al.* [2000], who used an end-member set that included obsidian glass (a glass end-member nearly identical to the silica- K_2O glass we use here [*Ramsey and Fink*, 1999; *Wyatt et al.*, 2001]), kaolinite, nontronite, Fe-smectite, and illite. Deconvolving the surface type 1 spectrum they found $\sim 10\%$ illite, $\sim 3\%$ kaolinite, and no occurrence of glass. Because the total glass plus phyllosilicate is below the detection limit stated by *Bandfield et al.* [2000], nothing can be said about the amount of glass or phyllosilicate actually present in the surface type 1 spectrum. Deconvolving the surface type 2 spectrum, *Bandfield et al.* [2000] found $\sim 10\%$ Fe-smectite, $\sim 2\%$ illite, and $\sim 25\%$ obsidian glass. The total glass plus phyllosilicate abundance was 37% , which is well above the TES detection limit. Assuming that glass on the surface of Mars is similar to the obsidian glass (silica- K_2O glass) in the end-member set, the resulting uncertainties are $\sim 25 \pm 6\%$ for the total glass abundance and $12 \pm 7\%$ for the total phyllosilicate abundance within the glass-phyllosilicate system. The glass abundance

reported by *Bandfield et al.* [2000] for surface type 2 remains above the stated detection limit, even with the maximum uncertainties used. However, the phyllosilicate abundances are mainly below the detection limit and their presence cannot be determined.

If there is reason to believe that both Martian glass and phyllosilicates are significantly different than those in the end-member set used by *Bandfield et al.* [2000], uncertainties rise to $25 \pm 24\%$ for glass and $11 \pm 24\%$ for phyllosilicate minerals, again, within the glass-phyllosilicate system. Although these uncertainties could, in extreme, predict 0% phyllosilicates (and 49% glass) or 0% glass (and 35% phyllosilicate minerals), our results indicate that modeling of both glass and phyllosilicate in the initial deconvolution indicates that both might be present in the mixture, and that the former set of uncertainties is the most reasonable. For the case in which glasses and phyllosilicates on Mars may be different from the spectra in the end-member set used by *Bandfield et al.* [2000] pyroxene and/or feldspar may be underestimated by up to 15% (AF).

Wyatt and McSween [2002] suggested that the proposed volcanic origin of the silica-K₂O glass may be too narrow of an interpretation, and that amorphous silica weathering products also may form on planetary surfaces and have a glass-like signature. However, the thermal infrared spectra of silica polymorphs, including products of weathering and hydrothermal alteration, exhibit band minima shifted relative to silica-K₂O glass, but which are similar to those of the pure silica glass [*Kraft et al.*, 2003; *Michalski et al.*, 2003], an end-member not included by *Bandfield et al.* [2000]. Our mixture analysis indicates that if the unknown mixture includes a component like the pure silica glass and possibly phyllosilicates, but the correct glass (and/or the

phyllosilicate) is not present in the end-member set, models may severely overestimate the Si-K₂O glass abundance by up to 65% the total glass plus phyllosilicate abundance, underestimate phyllosilicates by a similar amount, underestimate feldspar abundance, and exhibit visibly poor spectral fits resulting from the strong band minima in the pure silica glass spectrum and the displacement of the correct phase abundances. Because the *Bandfield et al.* [2000] end-member set lacked a pure silica spectrum, our analysis also indicates that their result cannot discriminate between silica-K₂O or pure silica glass. *Kraft et al.* [2003] and *Michalski et al.* [2003] point out that band minima associated with amorphous silicas (and pure silica glass) are inconsistent with the global surfaces deconvolved by *Bandfield et al.* [2000], an observation corroborated by our analysis. There are no characteristic misfits to the global surface types like those we observe in the numerical mixtures presented here, and glass remains a significant component of surface type 2 even with the maximum uncertainties applied.

6. Conclusions

(1) Even though emissivity spectra of glass and phyllosilicate minerals appear similar visually, their spectra are statistically separable. If the deconvolution algorithm is given all possible end-members, and minerals in an unknown mixture are very similar to those in the end-member set, results closely approximating the actual abundances are expected. If differences exist between the emissivity spectra of glasses and phyllosilicate minerals in the mixture and those in the end-member set, uncertainties arise in the reported abundances of those classes. We found that mixtures containing saponite,

nontronite, and halloysite give rise to the highest uncertainties in the reported abundances of glasses and phyllosilicate minerals in deconvolution models where the correct phyllosilicate was not present.

(2) For the phyllosilicate minerals and glasses used here, silica-K₂O glass is more susceptible to being modeled by phyllosilicate minerals than pure silica glass; this results from the proximity of the emissivity minimum in silica-K₂O glass to the minima of phyllosilicate minerals. Furthermore, when silica-K₂O glass is in the mixture but excluded from the end-member set used to deconvolve the mixture, phyllosilicates can be used to erroneously model the silica-K₂O spectral shape, sometimes with only a minimal increase in RMS error. Differences in RMS error at these levels must be greater than the emissivity-equivalent noise in the data in order for improvements to be significant, a situation examined neither here nor in previous studies. Exclusion of the silica-K₂O glass from an end-member set will result in overestimates of phyllosilicate abundance (up to 60%) if glass is present in the mixture, and the only way to discriminate between pure silica and silica-K₂O glasses is to include both as end-members. Therefore, we recommend that both glasses currently available be included in any deconvolutions of data that may contain amorphous components.

(3) We show that glasses and phyllosilicates in simple four-component mixtures tend to act as a two-component system and are anti-correlated. As a result, their absolute abundances are subject to uncertainties based on the total amount of glass and phyllosilicate in the mixture. By applying these uncertainties to the results of *Bandfield et al.* [2000], we find that the modeled glass abundance in the surface type 2 spectrum is

well above the detection limit of TES if the obsidian glass (silica-K₂O glass) is representative of glasses on Mars. Phyllosilicate abundances for surface type 2 remain at or below the detection limit even with the maximum uncertainties in deconvolved abundances applied.

(4) Our analyses indicate that amorphous weathering products with nearly pure silica compositions are the least likely glass spectra to be confused with phyllosilicates. As applied to Martian spectra, the relatively low RMS error and good spectral fit using an end-member set that did not contain the pure silica glass [Bandfield *et al.*, 2000b; Hamilton *et al.*, 2001; Wyatt *et al.*, 2001] indicates that pure silica glass, if present on the surface of Mars, is a small component of the TES spectral shapes. Furthermore, deconvolutions of the TES surface types that do include a pure silica glass end-member do not include that phase in the best fit [Michalski *et al.*, 2003], providing further support that the silica-K₂O glass is the best match to the amorphous component in Martian spectra. Based on available data, these results suggest that amorphous silica weathering components with compositions like those of Michalski *et al.* [2003] are not a substantial fraction of the Martian surface materials. Primary volcanic or secondary weathering phases with spectral characteristics like that of the silica-K₂O glass studied here may provide equally viable explanations for the origin of this component on Mars.

Acknowledgments

The authors would like to thank E. Hochberg for gracious assistance with the discriminant analysis presented here. J. Bandfield and an anonymous reviewer provided

very helpful formal reviews that improved the manuscript. This research was supported by the Mars Fundamental Research Program, grant NAG5-12685, and is HIG publication number 1389 and SOEST publication number 6611.

Tables

Table 1. Abundances (in percent) of components in four-component mixtures

| Phase | Gl + Phy > Pyx + Fsp | | Gl + Phy < Pyx + Fsp | |
|----------------------|----------------------|----------|----------------------|----------|
| | Gl > Phy | Gl < Phy | Gl > Phy | Gl < Phy |
| Glass (Gl) | 50 | 20 | 20 | 10 |
| Phyllosilicate (Phy) | 20 | 50 | 10 | 20 |
| Pyroxene (Pyx) | 15 | 15 | 35 | 35 |
| Feldspar (Fsp) | 15 | 15 | 35 | 35 |

Table 2. Wavenumber ranges and resolutions

| Spectral Sampling | Deconvolution Range |
|--------------------------------|--|
| Laboratory, 2 cm ⁻¹ | 1300 – 230 cm ⁻¹ |
| TES, 10 cm ⁻¹ | 1300 – 825, 508 – 232 cm ⁻¹ |
| TES, 10 cm ⁻¹ | 1300 – 780, 560 – 232 cm ⁻¹ |

Table 3. End-member sets tested for each deconvolution analysis

| End-member Set Tested | One-Component Deconvolutions | Two-Component Deconvolutions | Four-Component Deconvolutions |
|--|---------------------------------|---------------------------------|----------------------------------|
| Includes All End Members | + | + | + |
| Includes Only Glasses | + | | |
| Includes Only Phyllosilicates | + | | |
| Excludes Phyllosilicate in Mixture | + | + | + |
| Excludes Glass in Mixture | + | | |
| Excludes Glass and Phyllosilicate in Mixture | | + | + |

Table 4. Relative positions on the discriminant function plane

| End Member | Relative Position |
|-------------------------------|-------------------|
| Glasses | |
| Pure Silica Glass | 0.000 |
| Silica-K ₂ O Glass | 0.112 |
| Phyllosilicates | |
| Fe-smectite | 0.535 |
| Nontronite | 0.573 |
| Ca-montmorillonite | 0.574 |
| Illite | 0.718 |
| Kaolinite | 0.761 |
| Saponite | 0.797 |
| Halloysite | 1.000 |

Table 5. Deconvolution results for one-component mixtures

| Phase Modeled | End Member Set Includes: | | | | | |
|-------------------------------|--------------------------------|-----------|--------------|-----------|----------------------|-----------|
| | Both Glass and Phyllosilicates | | Only Glasses | | Only Phyllosilicates | |
| | Modeled Gl % | RMS error | Modeled Gl % | RMS error | Modeled Gl % | RMS error |
| Glasses | | | | | | |
| Silica-K ₂ O Glass | 23.9 | 0.023 | 100.0 | 0.035 | 0.0 | 0.036 |
| Pure Silica Glass | 100.0 | 0.052 | 100.0 | 0.052 | 0.0 | 0.072 |
| Phyllosilicates | | | | | | |
| Illite | 11.1 | 0.006 | 100.0 | 0.014 | 0.0 | 0.009 |
| Nontronite | 0.0 | 0.010 | 100.0 | 0.031 | 0.0 | 0.010 |
| Saponite | 7.3 | 0.008 | 100.0 | 0.017 | 0.0 | 0.008 |
| Ca-montmorillonite | 6.0 | 0.023 | 100.0 | 0.040 | 0.0 | 0.035 |
| Fe-smectite | 0.0 | 0.005 | 100.0 | 0.017 | 0.0 | 0.005 |
| Kaolinite | 1.5 | 0.009 | 100.0 | 0.019 | 0.0 | 0.009 |
| Halloysite | 0.0 | 0.005 | 100.0 | 0.012 | 0.0 | 0.005 |

Figures

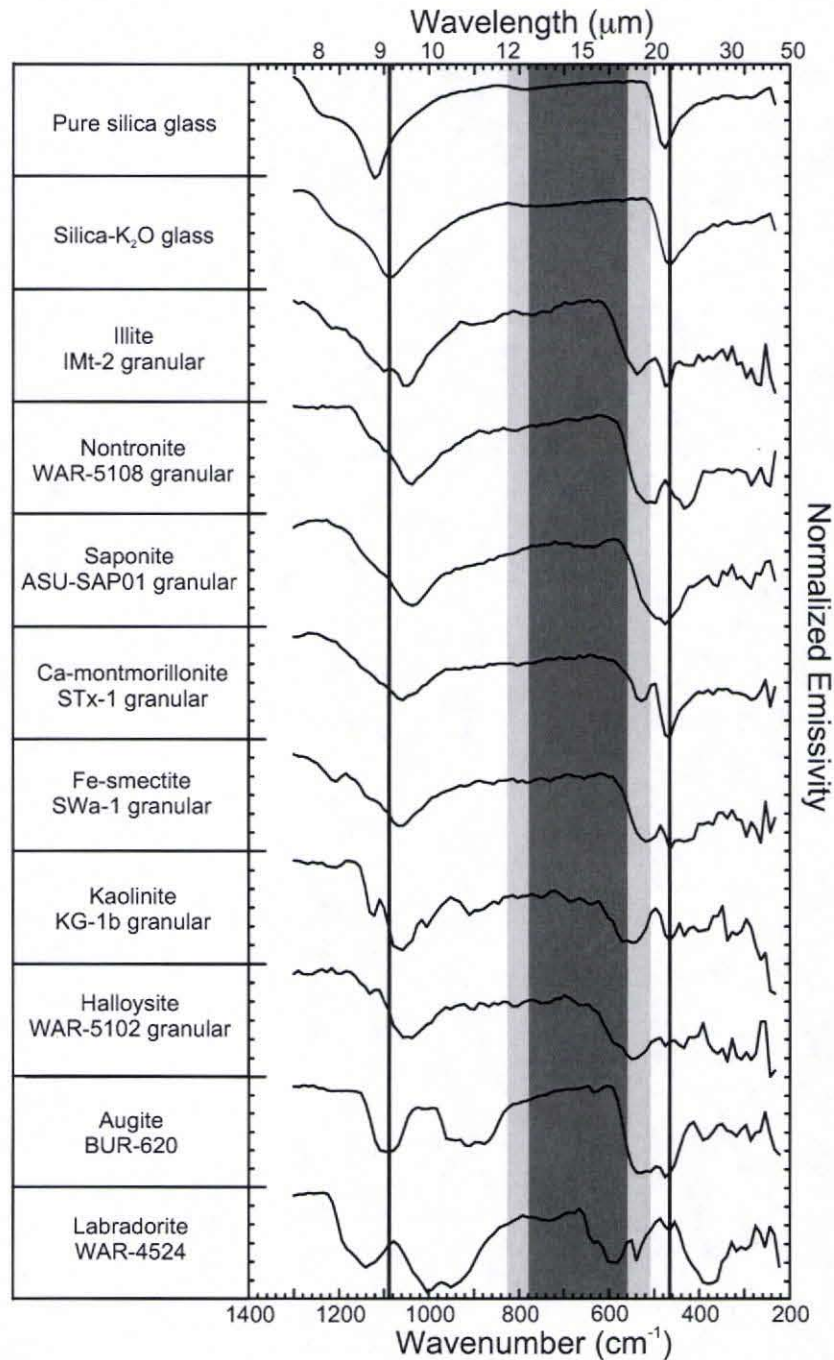


Figure 1. Normalized emissivity spectra (10 cm^{-1} resolution) of two glasses, seven phyllosilicates, one pyroxene, and one feldspar used in this study. Vertical lines mark the 1085 cm^{-1} and 465 cm^{-1} positions to emphasize differences in minima. Grayed areas are different wavenumber regions excluded from deconvolution as they are masked by atmospheric CO_2 . Dark gray is a narrowed CO_2 exclusion, light gray plus dark gray is a more typical CO_2 exclusion.

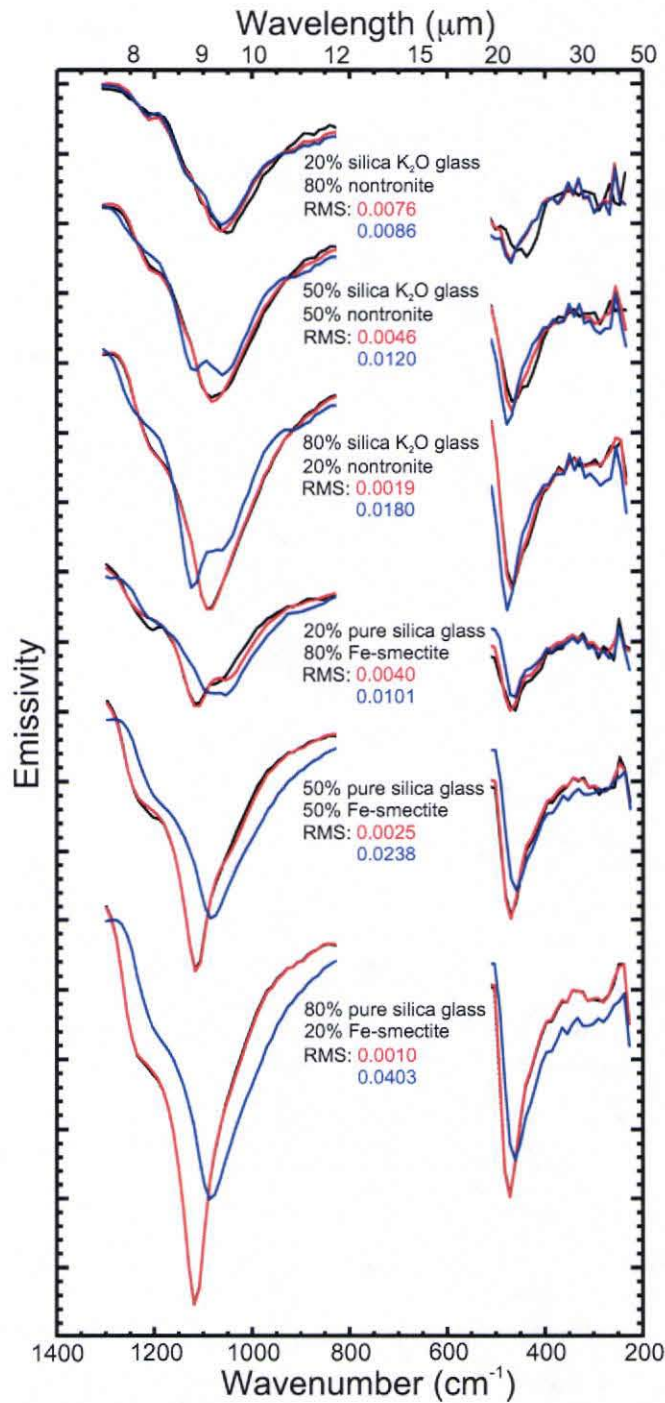


Figure 2. Example analyses for silica- K_2O glass and nontronite, pure silica glass and Fe-smectite. Mixture spectra are in black and offset for clarity. Red spectra are best-fit models that excluded the phyllosilicate in the mixture from the end-member set. Blue spectra are best-fit models that excluded both the glass and phyllosilicate in the mixture from the end-member set. Where the black mixture spectra are not visible, they are covered by closely matching red spectra.

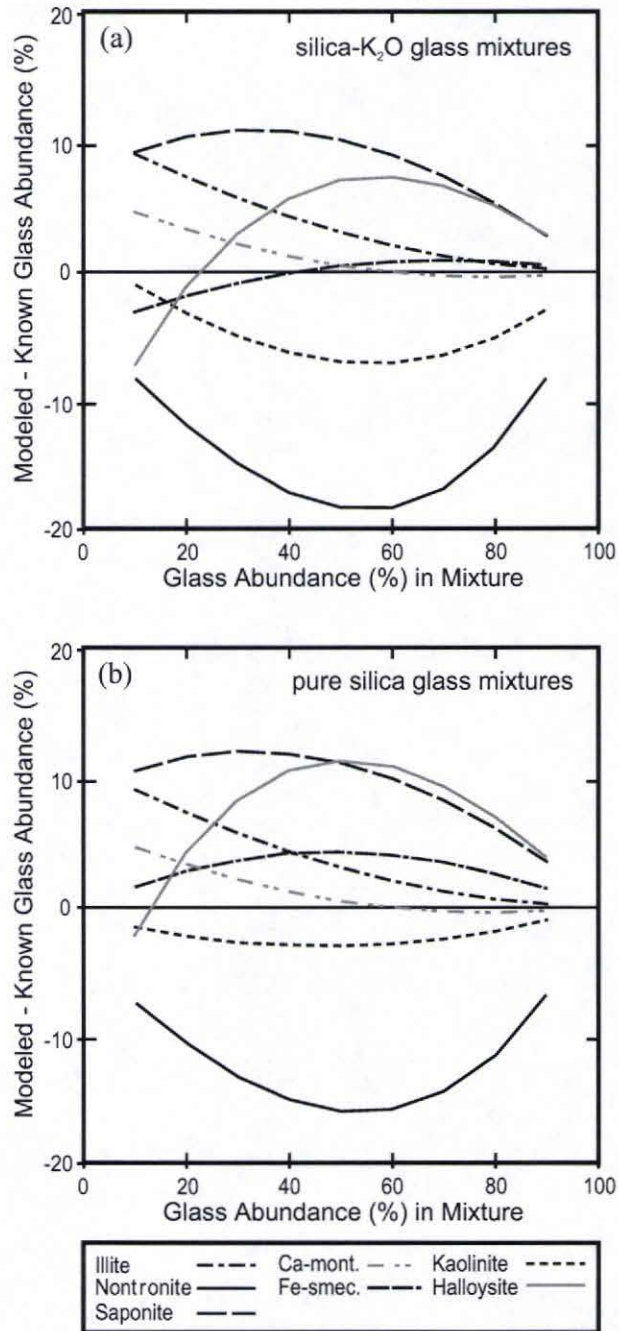


Figure 3. Errors (modeled - known) in glass determination for models that exclude the phyllosilicate in the mixture from the end-member set. Two-component mixtures are separated by those containing (a) silica-K₂O glass and (b) pure silica glass.

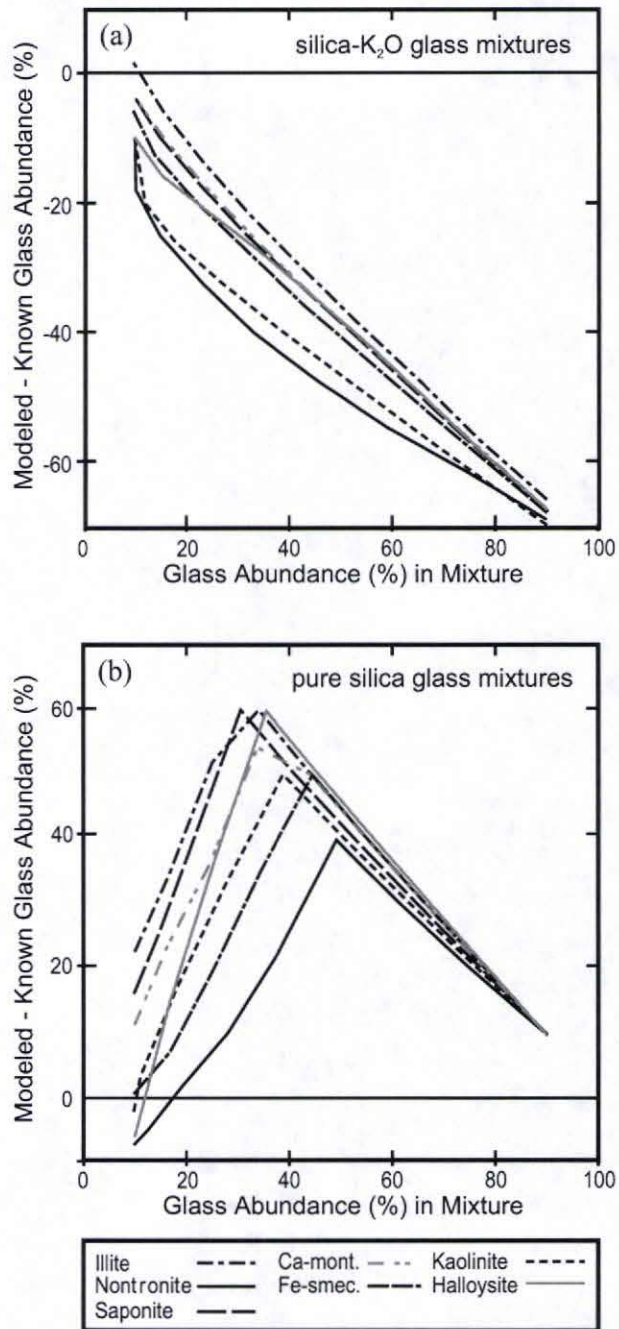


Figure 4. Errors (modeled - known) in glass determination for models that exclude both the glass and phyllosilicate in the mixture from the end-member set. Two-component mixtures are separated by those containing (a) silica-K₂O glass and (b) pure silica glass. Note differences in (modeled - known) axes.

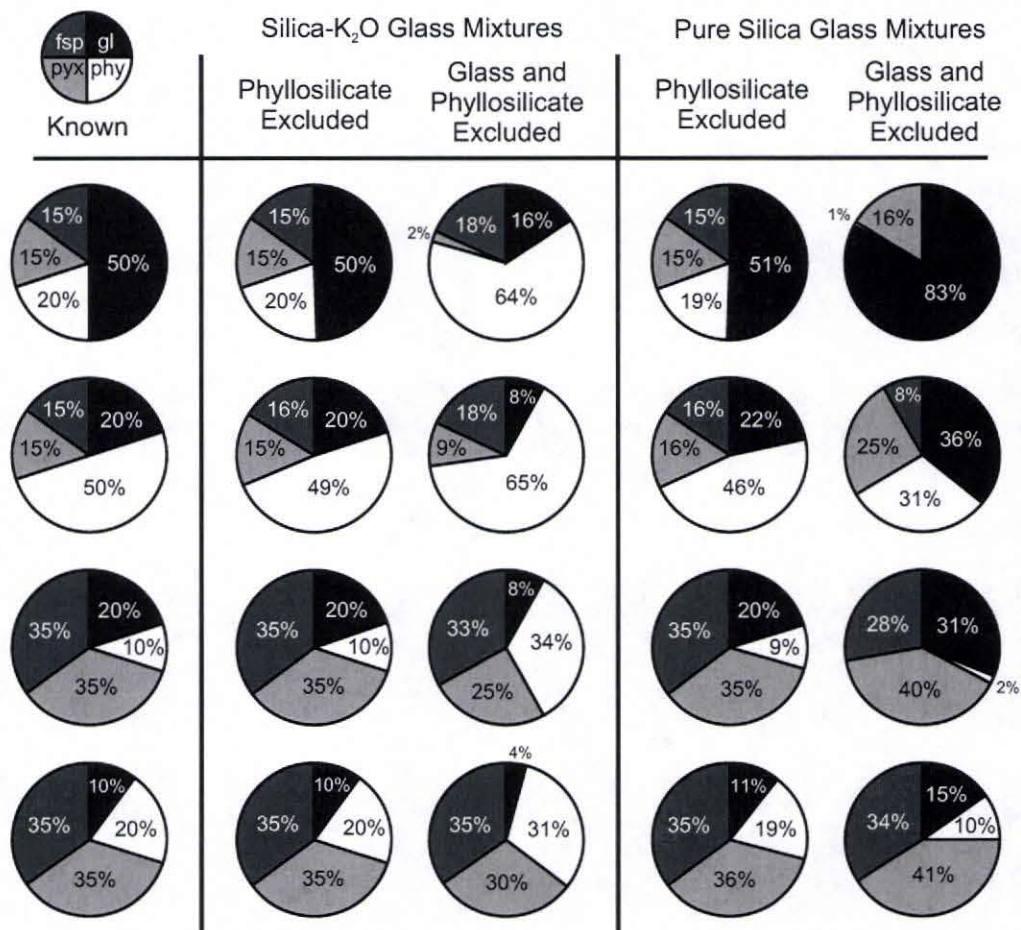


Figure 5. Mean modeled abundances for four-component deconvolutions that include glass (gl), phyllosilicate (phy), pyroxene (pyx), and feldspar (fsp). Models are grouped by end-member set and glass used to make the mixture. Seven models, corresponding to seven glass-phyllosilicate pairs, are averaged for each graph.

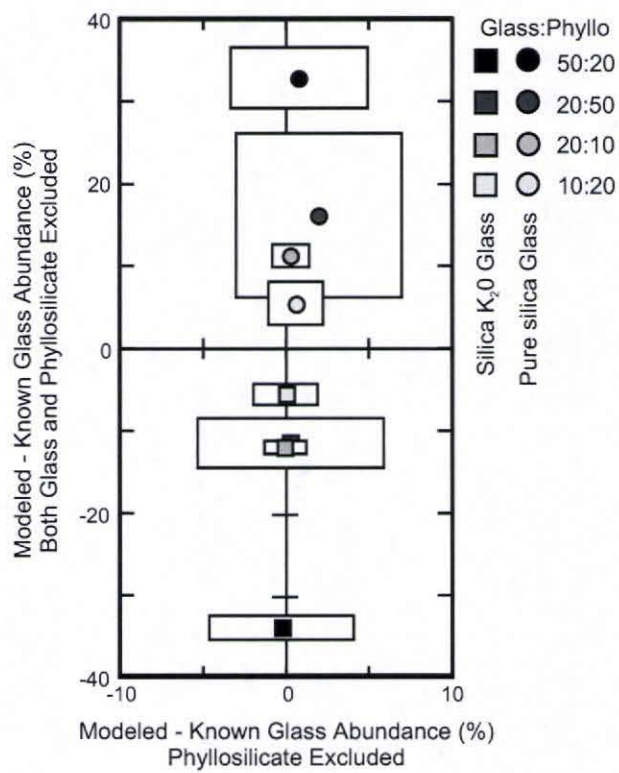


Figure 6. Mean errors (modeled - known) in glass abundance for two end-member sets tested on four-component mixtures. Data closer to the origin represents a better glass abundance determination for both end-member sets. Boxes surrounding data points represent the standard deviations. Note differences in axes.

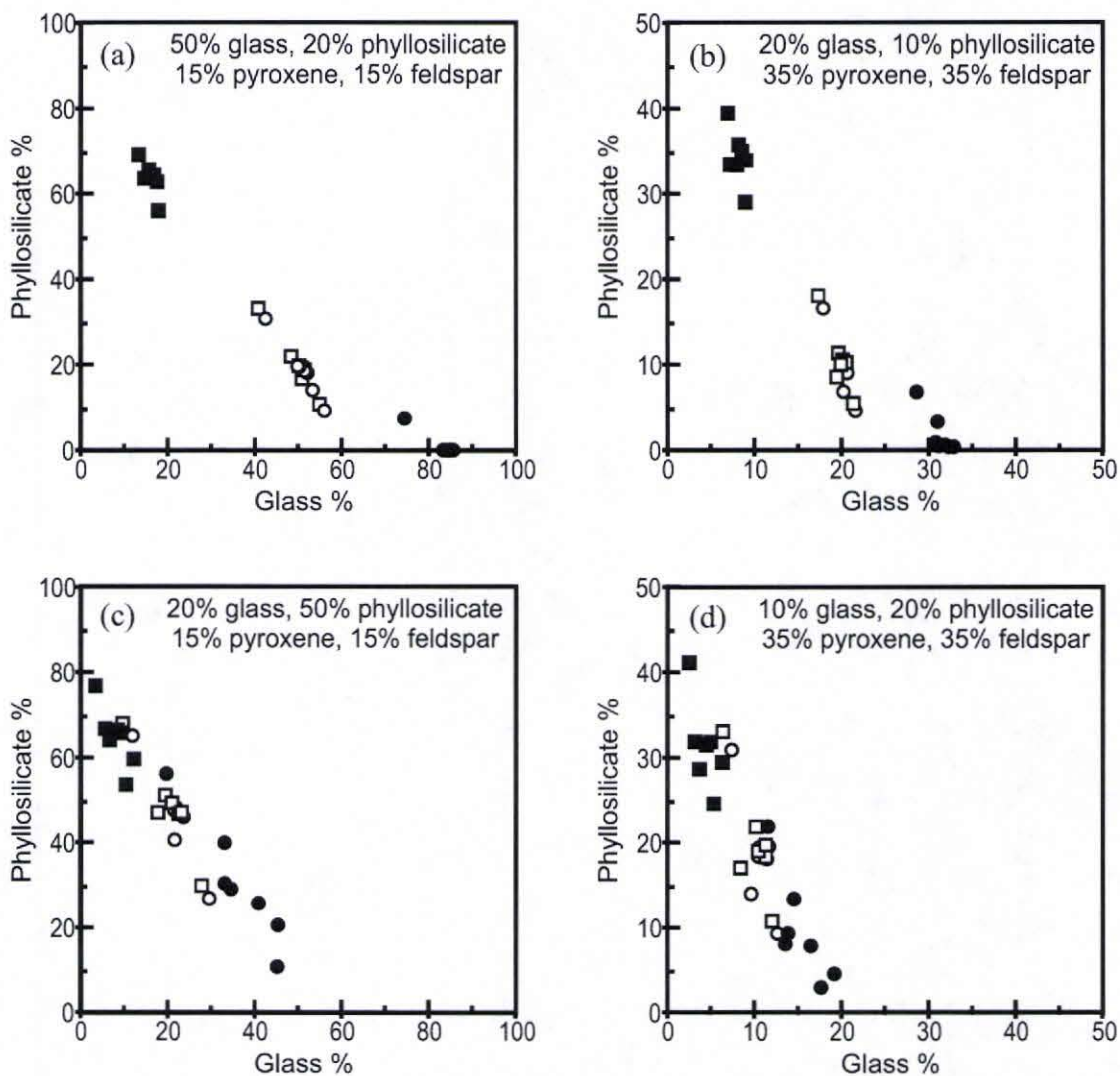


Figure 7. Modeled abundances for four-component deconvolutions. Square symbols are models of mixtures containing silica-K₂O glass, circles are models of mixtures containing pure silica glass. Open symbols are models using end-member sets that exclude the phyllosilicate in the mixture. Closed symbols are models using end-member sets that exclude the glass and phyllosilicate in the mixture.

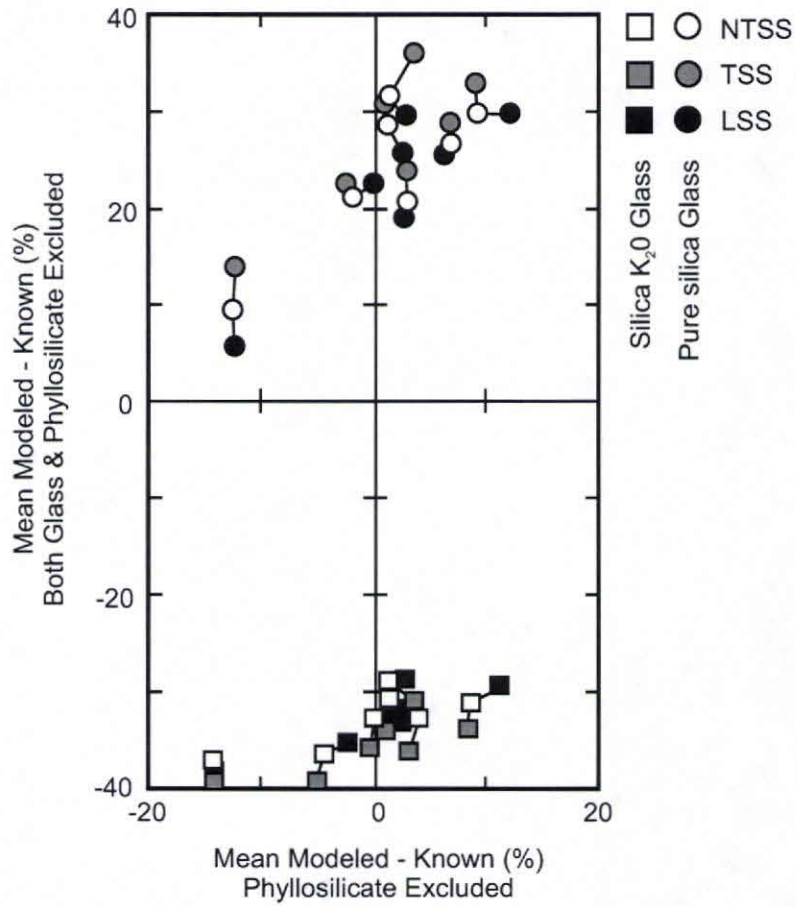


Figure 8. Mean errors (modeled - known) in glass determination for two end-member sets tested on two-component mixtures showing resolution effects on model results: laboratory spectral sampling (LSS), TES spectral sampling with a typical atmospheric CO₂ region removed (TSS), and TES spectral sampling with a narrowed CO₂ region removed (NTSS).

**CHAPTER 3: THE GLOBAL DISTRIBUTION, COMPOSITION,
AND ABUNDANCE OF OLIVINE ON THE SURFACE OF MARS
FROM THERMAL INFRARED DATA**

Published in its present form as Koeppen, W. C., and V. E. Hamilton (in press), Journal of Geophysical Research, manuscript #2007JE002984.

Abstract

We used spectral indexing and linear deconvolution to compare thermal infrared emission spectra of Fo₉₁, Fo₆₈, Fo₅₃, Fo₃₉, Fo₁₈, and Fo₁ olivine samples to Mars Global Surveyor Thermal Emission Spectrometer (TES) data over low-albedo regions of Mars. The Fo₉₁, Fo₆₈, Fo₅₃, and Fo₃₉ spectral end-members were confidently identified on Mars, a range of compositions wider than inferred from Martian meteorites. Small (<hundreds of km²) occurrences of the Fo₉₁ spectral end-member are present in the rims of the Argyre and Hellas impact basins and may represent Martian mantle materials. The Fo₆₈ spectral end-member is common throughout the highlands, chasmata, outflow channels, and Nili Fossae region. The Fo₅₃ spectral end-member occurs in eastern Syrtis Major, the Nili Fossae region, and smooth-floored craters of the highlands. Although less abundant than Fo₆₈ and Fo₅₃, the distribution of the Fo₃₉ spectral end-member suggests that some olivine on Mars is more Fe-rich than olivine in Martian meteorites. Global maps of olivine show that (1) materials containing 10-20% of olivine are common in the southern highlands of Mars, (2) olivine is most common near the topographic dichotomy boundary, and (3) olivine becomes uncommon near the poles suggesting that it may be influenced by topography and/or latitude (climate). Olivine is found in Early Noachian to Amazonian terrains, some of which may be coeval with phyllosilicate and sulfate deposits detected by OMEGA implying that any Early Noachian wet period of Mars' climate history may have been globally inhomogeneous or insufficient to weather the olivine that remains today.

1. Introduction

Olivine is an important rock-forming mineral on Earth, and its presence and composition can be used to place constraints on the origin, evolution, and erosion of its host rock. It is observed on the Moon [e.g., *Pieters, 1982; Tompkins and Pieters, 1999*] and many asteroids [e.g., *Binzel et al., 1997; Lucey et al., 2002*] using remote sensing techniques, and has been measured in lunar meteorites [e.g., *Papike et al., 1998*] and chondrites [e.g., *Brearley and Jones, 1998*]. Olivine is a component of many Martian meteorites including the Shergottite EETA79001 and most Nakhilites, and it comprises up to ~60% of some Iherzolitic Shergottites (e.g., ALH A77005) and 90% of Chassigny [*Mason, 1981; McSween and Treiman, 1998; McSween et al., 2006*, and references therein]. The crystallization of olivine plays a critical role in the chemical differentiation of magma chambers, and its composition and associated minerals record the chemistry of its parent magma, as well as its subsequent evolution due to differentiation, re-equilibration, melting, or alteration.

Olivine is a nesosilicate mineral found in mafic and ultramafic igneous rocks, and has strong spectral features in the thermal infrared (~2000 – 200 cm^{-1}). The molecular structure of olivine contains isolated silica tetrahedra separated by two distinct metal ion sites, which can be filled by Mg, Fe, Ca, and Mn [*Klein and Hurlbut, 1985*]. The most common solid-solution series of olivine ranges from Mg-rich forsterite (Mg_2SiO_4) to Fe-rich fayalite (Fe_2SiO_4). The Mg/Fe content of olivine within this series is denoted by its forsterite number ($\text{Fo}_\#$), which is defined as molar $\text{Mg}/(\text{Mg} + \text{Fe}) \times 100$. Spectral variation in thermal infrared observations of olivine has been documented by several

authors and correlates with its Mg/Fe content [e.g., *Duke and Stephens, 1964; Burns and Huggins, 1972; Salisbury et al., 1991; Fabian et al., 2001; Hoefen et al., 2003; Koike et al., 2003; Hamilton et al., in prep.*], a fact that can be exploited to determine the Mg/Fe content of olivine using astronomical measurements and remote sensing data of planetary surfaces.

The presence of olivine on Mars is inferred from analyses of thermal infrared emission data collected by the Mars Global Surveyor Thermal Emission Spectrometer (TES). *Hoefen and Clark [2001]* searched the TES data set for spectral features characteristic of different compositions of olivine, and presented a preliminary global map of olivine by composition. Their work culminated by showing the compositional variation of olivine in eastern Syrtis Major and a large regional occurrence of olivine in the region surrounding the Nili Fossae [*Hoefen et al., 2003*]. They identified the olivine in these areas as compositions of Fo₄₀₋₇₀. *Bandfield [2002]* used a linear least squares fitting technique to map the distribution of minerals, including olivine, on Mars. He modeled the TES data set using a library of spectra containing two olivine compositions, Fo₉₁ and Fo₁, and found geographic concentrations of olivine spectral shapes around the Nili Fossae and north of Argyre Basin. *Hamilton et al. [2003]* modeled the TES data set with the global spectral surface types 1 and 2 of *Bandfield et al. [2000b]* and spectra of Martian meteorites, including Chassigny and ALH A77005, which are dominantly comprised of Fo₆₈ olivine [*Prinz et al., 1974; McSween et al., 1979*]. *Hamilton et al. [2003]* found spatial concentrations of spectral shapes like those of the olivine-rich

meteorites in many locations across the mid-latitudes and most extensively near the Nili Fossae.

Olivine on the surface of Mars is also inferred from other spacecraft data. Visible near infrared (VNIR) data from the Mars Express Observatoire pour la Minéralogie, l'Eau, les Glaces, et l'Activité (OMEGA) instrument was used to map the presence and location of surficial olivine-bearing deposits [Bibring *et al.*, 2005; Mustard *et al.*, 2005; Poulet *et al.*, 2007]. Direct observations made by the Spirit and Opportunity rovers give strong evidence for olivine in basalts measured by the Mössbauer spectrometer and Mini-TES instruments [Christensen *et al.*, 2004b; Morris *et al.*, 2004], and visual inspection of crystallographic shapes in rock surfaces imaged by the Microscopic Imager (MI) suggests that olivine exists as megacrysts [McSween *et al.*, 2004].

The occurrence of olivine has been used to argue for water-poor histories for large portions of Mars [e.g., Christensen *et al.*, 2003; Hoefen *et al.*, 2003]. Compared to other silicates, olivine has the least polymerized structure and can break down easily in the presence of weathering agents [Goldich, 1938; Deer *et al.*, 1992]. Within the olivine Mg-Fe solid solution series, it has been shown that increasing the Mg content bolsters its resistance to chemical weathering and lowers its kinetic dissolution rate by nearly one order of magnitude over the range from fayalite to forsterite [e.g., Wogelius and Walther, 1992; Pokrovsky and Schott, 2000; Stopar *et al.*, 2006]. Therefore, the Mg content of olivine plays an important role in the calculated timescales during which water may have been present on the Martian surface and influences its preservation [Stopar *et al.*, 2006].

The global distribution, composition, and abundance of olivine on Mars is important information that can be used to synthesize data from its meteorites, ground observations, and models of mantle evolution. For example, estimates based only on Martian meteorites constrain the bulk of olivine on Mars to Fo₆₀ – 90, but ground measurements from the Mars Exploration Rovers (MERs) have normative compositions as low as Fo₅₁ [McSween *et al.*, 2004], suggesting a larger range may exist.

This work examines the global distribution and composition of olivine on Mars inferred from TES data using spectral indexing and deconvolution. We use these techniques together in order to increase the amount of area on Mars covered by TES data and obtain quantitative mineral abundance information from TES spectra. We verify the results with Thermal Emission Imaging System (THEMIS) images, compare and contrast our results with previous analyses, and make inferences about the origin and evolution of olivine-bearing materials on Mars.

2. Methods

The TES instrument is a Fourier transform Michelson interferometer that collects data from ~1700 to 200 cm⁻¹ (~6 – 50 μm) in either 143 or 246 channels [Christensen *et al.*, 1992]. The TES consists of an array of six detectors, each of which has a spatial footprint of 3 × ~8 km on the surface of Mars [Bandfield, 2002]. For this work we utilize single-scan (143 channels, 10 cm⁻¹ spectral sampling) apparent emissivity spectra derived from the calibrated radiance spectra calculated for each detector and observation, except

where explicitly noted. For a complete description of the TES instrument and radiometric calibration, see *Christensen et al.* [2001a].

We selected TES spectra for this study using specific quality criteria including derived surface temperatures >250 K, emission angles $<10^\circ$, albedo values <0.2 (relatively dust free surfaces), atmospheric dust opacities <0.2 (measured at $9 \mu\text{m}$), and water ice opacities <0.15 [*Bandfield et al.*, 2000b; *Pearl et al.*, 2001]. Water ice opacities >0.10 are higher than used by previous studies [e.g., *Bandfield et al.*, 2000b; *Bandfield*, 2002], but including these spectra allowed us to increase spatial coverage over the Martian surface. We single out and discuss the results of our analyses from the high water ice opacity spectra in Section 4.1. We did not include any data that showed risks of major or minor phase inversions, or data collected at times when the spacecraft's solar panels or high gain antenna were moving quickly. In order to avoid spectral regions dominated by atmospheric CO_2 , as well as decreased signal-to-noise at the ends of the measured range, we constrained the data to 73 points per spectrum distributed between $1302 - 825$ and $508 - 240 \text{ cm}^{-1}$ ($\sim 8 - 12$ and $20 - 42 \mu\text{m}$) [*Bandfield et al.*, 2000b; *Christensen et al.*, 2000c; *Hamilton et al.*, 2001]. In this paper, we refer to data from $1302 - 825 \text{ cm}^{-1}$ as the high-wavenumber region and data from $508 - 240 \text{ cm}^{-1}$ as the low-wavenumber region.

A noise anomaly, possibly associated with spacecraft vibrations, affects the high-wavenumber portions of TES data above approximately Orbit Counter Keeper (OCK) 7000 and worsens with increasing OCK [*Bandfield*, 2002; *Hamilton et al.*, 2003]. This anomaly is difficult to detect automatically, and it can result in erroneous mineral

detections in full-spectrum mixture modeling of the data [Hamilton *et al.*, 2003]. For our spectral modeling analyses we only included spectra acquired prior to OCK 8000, $\sim 2.3 \times 10^6$ spectra, to increase spatial coverage of Mars but avoid the most anomaly-prone data. For maps made with spectral indices, we included all the spectra in the TES database up to OCK 22,000, $\sim 9.3 \times 10^6$ spectra, as our indices use only the low-wavenumber regions of TES spectra, which appear to be unaffected by the anomaly [Bandfield *et al.*, 2004a].

2.1 Olivine Samples

To select olivine spectra for our analyses, we examined thermal emission spectra of ten olivine samples ranging from Fo₉₁ to Fo₁ (Table 1). The Fo₉₁ and Fo₁ spectra were obtained from the Arizona State University (ASU) spectral library [Christensen *et al.*, 2000b] and represent samples with a particle size fraction of 710 – 1000 μm measured with ASU's Nicolet 670 FTIR spectrometer. Eight intermediate compositions of olivine from the Kiglapait layered mafic intrusion in north coastal Labrador were provided to us by S. A. Morse, and their compositions are characterized by Morse [1996]. Particulate samples with grain sizes $>100 \mu\text{m}$ are appropriate for the dark regions of Mars [e.g., Ruff and Christensen, 2002], and we sieved each of the Kiglapait samples into discrete particle size fractions between 106 and 246 μm and selected the largest size fraction in each sample for analysis (Table 1). We measured the olivine samples using the University of Hawaii's Nicolet 470 FTIR spectrometer [Hamilton and Lucey, 2005], and used the method described by Ruff *et al.* [1997] to derive emission spectra from the measured voltages. We used a spectrum of atmospheric water vapor to subtract out many

of the spectral features due to humidity in the sample chamber from each measured spectrum. Laboratory data of all ten olivine samples were acquired at 2 cm^{-1} spectral sampling but were convolved to the 10 cm^{-1} spectral sampling of the TES data to determine appropriate band minima and maxima resolvable by the TES instrument (Figure 1). Similar to previous studies, the thermal emission spectra of the olivines in our suite have recognizable minima that linearly decrease in wavenumber with increasing $Fo_{\#}$ (Figure 1) [Salisbury *et al.*, 1991; Hamilton *et al.*, in prep.].

2.2 Spectral Index Analyses

A spectral index is an efficient way to identify spectral shapes in a large data set by mathematically reducing spectral features of interest to a single number [e.g., Kauth and Thomas, 1976; Richardson and Wiegand, 1977; Jackson, 1983; Christensen *et al.*, 2000a]. Typical indices use a few spectral bands over features of interest and a simple mathematical formula to identify the possible presence of those features in each spectrum. Critical absorptions are spectral features consistently present in all of the spectra of a mineral type [Hamilton, 2000], and we created spectral indices to search for a low-wavenumber critical absorption of olivine that shifts in position as a function of Mg/Fe, thereby distinguishing between its compositions [Hamilton *et al.*, in prep.]. Similar to Christensen *et al.* [2000a] and Bandfield *et al.* [2004a], our spectral indices follow the form of:

$$I_{fo\#} = (\epsilon_{\lambda 1} + \epsilon_{\lambda 3}) / 2\epsilon_{\lambda 2}$$

The index value ($I_{fo\#}$) represents the relative depth of the spectral feature defined by comparing its emission minimum ($\epsilon_{\lambda 2}$) to its flanking emission maxima ($\epsilon_{\lambda 1}$ and $\epsilon_{\lambda 3}$). $I_{fo\#}$ is designed to be >1.0 when the feature is present and ≤ 1.0 if the feature is absent or inverted. Ideally, each ϵ_{λ} is the average of measured apparent emissivity values for a pair of adjacent TES channels in order to reduce point-to-point noise present in some data.

We selected spectral bands in the $500 - 300 \text{ cm}^{-1}$ region of TES data because it is relatively free of features associated with suspended dust and atmospheric CO_2 gas, and it serves as a spectral window through which surface emissivity features are observed, even in data that are not atmospherically corrected [Ruff and Christensen, 2002; Bandfield et al., 2004a]. Olivine has relatively narrow spectral features in this wavenumber region that shift with $Fo\#$ and allow us to distinguish between multiple compositions (Figures 1 and 2). However, the narrowness of the olivine's low-wavenumber spectral features prohibits the use of two adjacent emissivity values at every ϵ_{λ} . Where available, we used averages of two adjacent emissivity values, but it was commonly necessary to use only one value at each ϵ_{λ} . Although using a single critical absorption characteristic of olivine for all of the indices was preferable, the spectral feature characteristic of olivine in the low-wavenumber region contains two critical absorptions (Figure 2) [Hamilton et al., in prep.]. The higher-wavenumber critical absorption becomes indistinguishable in the spectra of olivine samples with $Fo < 2.5$, and we had to target the lower-wavenumber critical absorption for those indices.

We created six spectral indices to identify the full range of Mg/Fe in olivine, and the band positions used for each index are listed in Table 2. The compositional accuracy

of our spectral indices is limited by the spectral resolution of the data, because the difference in band minima between similar compositions of olivine is not large and the minima of similar compositions of olivine directly overlap at the 10 cm^{-1} spectral sampling of the TES instrument. Specifically, the low-wavenumber emissivity features of Fo₆₈ and Fo₆₀; Fo₃₉, Fo₃₅, and Fo₂₅; and Fo₁₀ and Fo₁ are indistinguishable using spectral indices (Figure 2). We used the emission minima of olivine's low-wavenumber critical absorptions measured under laboratory conditions to determine a linear function of wavenumber position vs. Fo_# for each critical absorption. We then calculated the range of olivine compositions predicted to have a minimum at the $\epsilon_{\lambda 2}$ TES channel(s) of each index, and titled the index by the full range of Fo-content that it potentially identifies.

The low-wavenumber regions of thermal infrared spectra exhibit features of many minerals other than olivine, and we determined the minerals to which our indices may also be sensitive by calculating the olivine index values for all of the spectra in the ASU mineral library. This analysis identified non-olivine mineral spectral shapes that might return a high olivine index value. Minerals that produced index values of at least half that of the associated olivine are listed in Table 3 and include mostly carbonates along with a few silicates. Carbonates have not been confidently identified in abundances >5% on Mars [Bandfield *et al.*, 2003]; however, clinopyroxene (diopside) is common in TES deconvolution results [e.g., Bandfield *et al.*, 2000b; Christensen *et al.*, 2000c] and may produce false identifications in the Fo₅₈₋₇₄, Fo₄₂₋₅₇, and Fo₂₅₋₄₁ indices. On the other hand, no mineral listed in Table 3 produced an index value greater than that calculated for the

indexed olivine, and false identifications of pyroxene in the spectral index analyses should be recognized by comparing its spatial distributions to the deconvolution analyses of this work, that of *Bandfield* [2002], and the maps of pyroxene-dominated meteorite spectra by *Hamilton et al.* [2003]. Quartz was shown to be ambiguous with the Fo₂₅₋₄₁ index and has been detected on Mars, but in only a few well-known locations that are easily identifiable [*Bandfield et al.*, 2004a]. We did not test the index calculations against combinations of two or more mineral spectra, which generally have less well-defined individual spectral features because of interference between the component spectra but may also add linearly to produce features that return high index values.

Unfortunately, the lower-wavenumber critical absorption we needed to use for the Fo₁₁₋₂₄ and Fo₀₋₁₀ indices encroaches into the <300 cm⁻¹ region, which can have highly variable emission features attributed to atmospheric water vapor and ice [e.g., *Smith et al.*, 2000; *Smith*, 2002]. We calculated the index values for these spectral indices in order to test whether spectral indices could be used to locate occurrences of these compositions even with atmospheric interference. However, we expect most variations in these indices to be dominated by atmospheric components.

2.3 Linear Deconvolution Analyses

We derived the quantitative fractional contributions of mineral components to TES spectra using linear deconvolution. Linear deconvolution is based on the observation that the spectrum of a mixture can be produced by a linear combination of the spectra of its components, referred to here as spectral end-members, in proportion to

their abundance [Lyon, 1959; Johnson *et al.*, 1983; Crown and Pieters, 1987; Gillespie, 1992; Thomson and Salisbury, 1993]. Conversely, the spectrum of a rock mixture may be fit using mineral spectra via a linear least-squares algorithm to derive component compositions and abundances [e.g., Ramsey and Christensen, 1998; Staid *et al.*, 2001; Johnson *et al.*, 2003]. Such modeling has been used by many investigators to study laboratory, meteorite, and TES data with relatively good results [e.g., Hamilton *et al.*, 1997; Feely and Christensen, 1999; Bandfield *et al.*, 2000b; Christensen *et al.*, 2000c; Hamilton and Christensen, 2000; Wyatt *et al.*, 2001; Johnson *et al.*, 2003]. We used the algorithm of Ramsey and Christensen [1998] with modifications by Bandfield *et al.* [2000b], which iteratively models the mixture spectrum using a library of spectral end-members primarily representing pure phases, but not necessarily end-member compositions. The fitting technique allows both positive and negative fractional contributions to the model fit, and the algorithm removes the spectral end-members with negative fractional contributions until a best-fit model that contains only positive (i.e., geologically plausible) fractional contributions is obtained. Outputs of the algorithm include the best-fit model spectrum, the final fractional contributions of each spectral end-member used in the best-fit model spectrum, and an RMS error value.

For TES data, the wavelength-dependent radiance measured at the spacecraft is the sum of the radiance of the atmosphere and the radiance of the surface, which is attenuated by atmosphere. Mixing of the atmospheric and surface spectral components of thermal infrared data is generally nonlinear; however, their respective contributions to TES data can be closely derived by a linear approximation if the Martian surface

temperature is relatively warm (>250 K) compared to the atmosphere during the observation [Bandfield *et al.*, 2000a; Smith *et al.*, 2000]. These conditions are met by all of the TES data selected for our analyses. The atmospheric dust and water ice spectral shapes derived from TES data by target transformation are relatively invariant except for some features attributed to CO_2 and H_2O gas [Bandfield *et al.*, 2000a], and they can be used as spectral end-members in the deconvolution algorithm to simultaneously derive the fractional contributions of the atmospheric and surface spectral end-members to each TES spectrum [Bandfield *et al.*, 2000a; Smith *et al.*, 2000].

We calculated the surface mineral abundances associated with each TES spectrum by normalizing their individual fractional contributions so that the surface components sum to unity [Smith *et al.*, 2000]. Similarly, the atmospheric spectral components can be multiplied by their derived fractional contributions and subtracted from the observed apparent emissivity spectrum to retrieve an atmosphere-removed (surface) emissivity spectrum [Smith *et al.*, 2000], which we use illustrate the spectral features in some olivine-bearing areas. We made maps both of fractional contribution and surface abundance for individual spectral end-members and combinations of spectral end-members by binning the irregularly spaced TES observations according to latitude and longitude. In general, we report the mean value in each bin.

It was not necessary to include all ten of the olivine samples measured here as spectral end-members in the deconvolution analyses because some compositions (e.g. Fo_{68} and Fo_{60}) have very similar band shapes and minima at the 10 cm^{-1} spectral sampling of TES (Figures 1 and 2). The linear independence of such similar end-

members is very weak, and including them in the spectral library can result in variations to their derived fractional contributions that track minor natural differences, noise, and systematic errors rather than significant spectral differences. The corollary is that, like the spectral indices, each olivine spectral shape represents a range of similar compositions dependent on the spectral sampling of TES and the differences in spectral features correlated with Mg/Fe content. However, the compositional range represented by each spectral end-member is difficult to estimate using linear deconvolution because it is dependent on spectral features in the entire range of the spectral end-member. We used only six of the ten olivine spectra (Fo₉₁, Fo₆₈, Fo₅₃, Fo₃₉, Fo₁₈, and Fo₁) as spectral end-members in deconvolution analyses because they have relatively unique spectral shapes among the olivine series, and we list them by their specific Fo_# recognizing that they do not represent exact compositions found on Mars.

Other spectral end-members used in the deconvolution analyses included spectra of pure minerals and glasses, one nearly monomineralic Martian meteorite, atmospheric components, and a blackbody spectrum (unit emissivity at all wavenumbers) (Table 4). The mineral spectral end-members in our set were measured in laboratory conditions [Christensen *et al.*, 2000b] and selected to identify a broad range of olivine compositions as well as commonly associated minerals and weathering products [Michalski *et al.*, 2005; Rogers and Christensen, 2007]. We adjusted the spectral contrast of two potential weathering products, saponite and illite, to match other “solid” clays in the ASU spectral library because those samples had smaller and larger apparent grain sizes than the rest of our clay spectral end-members. A full description of the sample differences and spectral

adjustment for the saponite and illite samples can be found in *Rogers and Christensen* [2007]. We included a spectrum of Martian meteorite ALH 84001 to better approximate orthopyroxene shapes known to be present on Mars [*Hamilton et al.*, 2003]. We utilized atmospheric end-member spectra derived from TES data representing water vapor, water ice clouds, suspended dust, and atmospheric CO₂ [*Bandfield et al.*, 2000a; *Smith et al.*, 2000]. Variations in the total contrast of thermal infrared spectra can result from particle-size effects [e.g., *Aronson et al.*, 1966; *Salisbury and Wald*, 1992; *Moersch and Christensen*, 1995] as well as lava vesicularity [*Ramsey and Fink*, 1999], and the fractional contributions of the end-member spectra in the best-fit model may not sum to 1.0. To account for this possibility, we included a blackbody spectral end-member, which allows the deconvolution algorithm to better match mixture spectra of different total contrasts [*Hamilton et al.*, 1997].

2.4 Estimating the Detection Limit of Olivine

The error in determining most mineral end-member abundances by deconvolution of thermal emissivity data collected in laboratory conditions is estimated to be $\pm 5\text{-}10\%$ [*Feely and Christensen*, 1999; *Christensen et al.*, 2000c; *Wyatt et al.*, 2001]. This estimate includes errors accrued from spectral variability in the precision of the thermal infrared instruments [*Ramsey and Christensen*, 1998], normalizing out the blackbody spectral end-member [*Hamilton et al.*, 1997; *Feely and Christensen*, 1999], and determination of the modal mineralogy of laboratory rock samples using a microprobe [*Wyatt et al.*, 2001]. An additional $\sim 5\%$ uncertainty is added when laboratory data is

resampled to TES spectral sampling [Hamilton *et al.*, 2001], and uncertainties may be even higher when deriving mineral abundances from their fractional contributions in TES spectra that have large atmospheric contributions. However, the uncertainty for each mineral is different depending on the depth, shape, and location of the spectral bands [Christensen *et al.*, 2000c], and minerals with narrow and distinct band minima may be detected at relatively low fractional contributions [Bandfield, 2002].

Compared with the rest of the ASU spectral library, olivine has particularly strong spectral features and its detection limit on Mars has been suggested to be as low as 5% fractional contribution [Hamilton *et al.*, 2003]. As a qualitative example, in Figure 3 we show a representative TES spectrum, its atmosphere-removed spectrum, and models generated by using different fractional contributions of olivine to show that differences of 5% can be visually identified as erroneous. The best-fit model to the TES spectrum derived by deconvolution contains a Fo₉₁ fractional contribution of ~10%. We added or removed 5% increments of the Fo₉₁ spectral shape to the best-fit model, renormalized the other end-member contributions, and recreated the model with the new fractional contributions. A visually poor model fit is identifiable at 900 cm⁻¹ in the TES emissivity spectrum and can be clearly distinguished at 1100, 900, and 325 cm⁻¹ in the atmosphere-removed surface spectrum.

We generated two more empirical examples to estimate the detection limit of olivine and place lower bounds on the believable abundances in our deconvolution analyses. In the first example, we compared the spectral contrast of the olivine features found in observed spectra to those of pure olivine spectra in our samples by using index

values. In theory, the fractional contribution of the olivine spectral shape should be linearly correlated with the index values calculated for each spectrum, i.e. as the olivine concentration increases, the feature deepens and the index value increases. This correlation provides an estimate of the fractional contribution of olivine, assuming that the depth of the feature is based only on fractional contribution of olivine without blackbody/particle size effects or the presence of other phases that might increase or decrease the spectral contrast. For our index maps, the minimum index value empirically found to correlate with olivine-like spectral shapes, 1.015, corresponds to pure olivine spectra with contrasts of 8%, 12%, and 13% for the Fo₉₁, Fo₆₈, and Fo₅₃ spectral end-members, respectively. In practice there is only a weak relationship between Fo₅₈₋₇₄ and Fo₄₂₋₅₇ spectral indices and deconvolved fractions of the Fo₆₈ and Fo₅₃ spectral end-members (Figure 4). In the second example, we deconvolved several TES spectra identified by index values within the range we empirically estimated as valid. The resulting fractional contributions had a mean olivine abundance of $7.8 \pm 3.7\%$ for the Fo₉₁, Fo₆₈, and Fo₅₃ compositions. The minimum value obtained in this calculation, ~4%, represents the lowest limit at which olivine spectral shape was detected independently by the spectral index and deconvolution. Both examples bolster our confidence in detection of olivine at abundances as low as 5%.

2.5 Validation of Isolated Detections

We applied decorrelation stretches (DCS) to data from the Mars Odyssey Thermal Emission Imaging System (THEMIS) to validate potential olivine-bearing materials

identified in small numbers of TES spectra. The THEMIS instrument consists of infrared and visible multispectral imagers that have spatial resolutions of 100 m and 18 m, respectively (see *Christensen et al.* [2004a] for a complete description). The infrared imager of THEMIS records data in 10 bands distributed between 1500 and 650 cm^{-1} and complements the TES because it collects data in the same wavenumber range at higher spatial resolution, albeit with decreased spectral resolution. The DCS enhances the spectral variation in a multi-band image [*Gillespie et al.*, 1986; *Gillespie*, 1992], and, using THEMIS bands 8, 7, and 5 (centered at 850, 905, and 1070 cm^{-1}) mapped as red, green, and blue, olivine appears purple in the processed image [*Hamilton and Christensen*, 2005; *Rogers et al.*, 2005]. It is not yet clear if different compositions of olivine can be distinguished in THEMIS spectra, but DCS images are a quick way to visually scan an area and verify the presence of olivine suggested by a high index value or deconvolution analysis of TES data.

Additionally, we visually inspected many distinct occurrences of olivine identified by TES spectra to verify the presence of the olivine spectral shape in the apparent emissivity and atmosphere-removed emissivity TES spectra. In some cases we made spectral ratios of olivine-bearing materials to non-olivine bearing materials in order to confirm that the band minima in the ratio matched those of the olivine composition identified by indices or deconvolution.

3. Results

3.1 Spectral Index Analyses

We calculated the six spectral indices shown in Table 2 for $\sim 9.3 \times 10^6$ TES spectra (OCKs 1583 to 22,000) meeting our quality constraints, as described above. We performed an extensive manual evaluation of individual spectra with index values >1.0 and determined that values between ~ 1.015 and 1.060 represent what we believe to be valid detections of the olivine-like shape for most cases. Although any index value >1.0 should indicate the presence of a feature in that spectrum, small point-to-point emissivity differences, which may be due to noise or minor spectral components other than olivine, also produce values slightly >1.0 . Unfortunately, this range also excludes from identification some spectral mixtures that contain olivine, but whose olivine spectral features are diminished because of other spectral components in the mixture. For example, the surface type 1 spectral shape derived by *Bandfield et al.* [2000b], which likely contains 5-10% olivine [*Rogers and Christensen, 2007*], produces olivine index values >1.0 , but <1.015 . In a few cases, some index values between 1.015 and 1.060 may also be erroneous where they are correlated with the same detector number(s) in the same OCK and sequential Incremental Counter Keepers (ICKs). Values $>\sim 1.060$ are strongly correlated with orbit track-dependent noise and are not reliable.

We removed from the data set any index values outside of the valid range as well as those suggesting detector-correlated noise, and we mapped the remaining values into a spatial context (Figure 5). Strictly interpreted, index values do not represent abundance, but merely identify the presence of olivine-like spectral contributions to the total signal

measured by the TES. Therefore, we mapped only the locations of values that fell within the acceptable range. Because we calculated six indices for every spectrum, it was possible for a single spectrum to be identified by more than one index within the valid range. The index values for different compositional indices are not directly comparable as they use different band positions, and the mean index value of the spectra changes with each index (Figure 4); for example, most of the F_{042-57} index values are >1.0 while most of the $F_{075-100}$ values are <1.0 . In order to present the spatial distributions of valid olivine index identifications and eschew the bias of higher index values associated with a particular index we show only the highest $F_{0\#}$ identified for each spectrum in this map.

The $F_{075-100}$, F_{058-74} , and F_{042-57} spectral indices identify spectra in spatially coherent patterns and are shown in Figure 5 as red, yellow, and blue points, respectively. The $F_{075-100}$ index is the least ambiguous of the six indices with respect to other minerals in the ASU spectral library (Table 3) and identifies 161 spectra in the region surrounding the Nili Fossae, 76 spectra in the northern portion of Argyre rim, and 22 spectra in the northern portion of Hellas rim. Spatial groupings containing fewer spectra are located in two craters in Aurorae Planum, and in Ganges Chasma, Simud Vallis, and Oxia Palus. Possible olivine-bearing materials identified by only one or two spectra, but validated using THEMIS DCS images (described in Section 3.2), are located in Chryse Planitia, northern Terra Sirenum, and Terra Tyrrhena. The F_{058-74} index identifies a large grouping of spectra in the area surrounding the Nili Fossae, similar to previous work using spectral feature identification [Hoefen et al., 2003; Martinez-Alonso et al., 2006]. The F_{058-74} index also identifies many spectra inside the southwest rim of Isidis Basin, in

two craters in Aurorae Planum, in Ganges and Eos Chasmata, southern Xanthe Terra, and on the northern portions of the Hellas and Argyre Basin rims. Small groupings of one to five TES spectra are located in Chryse Planitia and throughout the southern highlands of Terrae Tyrrhena and Cimmeria. The F_{042-57} index identifies many more total spectra than the $F_{075-100}$ and F_{058-74} indices combined; however, it also shows less spatial coherence suggesting that it is influenced by noise in the spectra. Spatial groupings of spectra identified by the F_{042-57} index are found in the region surrounding the Nili Fossae and two craters in Aurorae Planum. Groupings of fewer spectra are found distributed across Syrtis Major, Xanthe and Tyrrhena Terrae, and inside craters in northern Noachis and Cimmeria Terrae.

The F_{025-41} , F_{011-24} , and F_{00-10} indices also produce values between 1.015 and 1.060, but the spatial distributions of spectra they identify suggest that they are inaccurate, and we do not show them. Specifically, the distribution of spectra identified by the F_{025-41} index lacks spatial coherence, perhaps because it uses only one emissivity value at each ϵ_λ making it prone to spectral noise. The F_{011-24} index also lacks spatial coherence, and appears to be dominated by highly variable emission features associated with water vapor and ice in the $<300 \text{ cm}^{-1}$ region [e.g., *Smith et al.*, 2000; *Smith*, 2002]. The F_{00-10} index produces values in the valid range that exhibit spatial coherence in Terra Meridiani, Aram Chaos, and the Valles Marineris. However, those regions and the spatial outlines of the distributions of spectra identified correspond directly to regions previously identified as hematite-rich [*Christensen et al.*, 2001b]. A similar correlation was pointed out by *Bandfield* [2002], who noted the lack of independent evidence for olivine in those

areas. Hematite was not identified a priori as a potential source of ambiguity in Table 3, because the hematite sample in the TES spectral library (BUR-2600), which we tested, has minima at slightly higher wavenumbers than the spectral shape derived for hematite on Mars by *Christensen et al.* [2000a].

As an additional component to the index analyses, we explored the possibilities of using the double-scan (286 channels, 5 cm^{-1} spectral sampling) apparent emissivity TES spectra to confirm and improve the $Fo_{\#}$ determination. The increased spectral resolution would be particularly useful for further refining the Mg-rich (Fo_{75-100}) olivine identification. Some double-scan TES spectra do exist over the occurrences of olivine identified by the Fo_{75-100} and Fo_{58-74} olivine indices in northern Argyre and Terra Tyrrhena, respectively, but the spectra are too few (<10) and too noisy to be useful. As a broader test case, we attempted to find and average a number of double-scan TES spectra over Nili Fossae and generated one of the most promising spectral shapes by averaging over 20 spectra (covering a total of nearly 500 km^2) in the area. The overall shape of olivine is obvious in the resulting average spectrum, and, consistent with the single scan TES data, it does appear qualitatively to be more like Fo_{58-74} than Fo_{75-100} or Fo_{42-57} . However, the exact band minimum, which is necessary to refine the $Fo_{\#}$ determination beyond what is possible from the single-scan TES data, was still obscured by the increased noise inherent to double-scan TES data, especially in the low-wavenumber features. Averaging even more spectra may allow these data to be used to refine $Fo_{\#}$ determinations, but it also increases the danger of averaging locations that have multiple compositions of olivine and defeating its purpose.

3.2 Deconvolution Analyses

We made fractional contribution maps of surface mineral classes (feldspar, high-calcium pyroxene, low-calcium pyroxene, olivine, silica/phyllsilicate, and sulfate) by summing the contributions of their individual end-members to each TES spectrum, binning the data at 2 pixels per degree, and reporting the mean fraction for each bin/pixel (Figure 6). These data represent the mean fractional contributions of each mineral group to the apparent emissivity spectra, which include contributions from atmospheric and blackbody (spectrally neutral) components. Data are mapped wherever they meet the criteria for this study, e.g., no data with albedo values <0.2 were available over large portions of the Tharsis region, Arabia Terra, Utopia and Elysium Planitae, Vastitas Borealis, or the central Hellas Basin. Mean fractional contributions higher than the $\pm 10 - 15\%$ detection threshold of TES are present in all of the maps. The feldspar, pyroxene, olivine and sulfate maps broadly correlate with the surface type 1 maps of *Bandfield et al.* [2000b] whereas the silica/phyllsilicate map correlates with both surface type 1 and surface type 2 maps. In general, high fractional contributions for all mapped phases are found over Syrtis Major, Xanthe and Tyrrhena Terrae, and portions of Cimmeria and Sirenum Terrae. Fractional contributions $>15\%$ are common in the feldspar and silica/phyllsilicate maps. An RMS error map stretched from 0.00 to 0.01 emissivity exhibits RMS errors that are lowest near the equator and increase toward the higher latitudes, but nearly all areas have RMS errors <0.01 suggesting that they are relatively well modeled using the end-member set chosen for this study. RMS error values >0.01

emissivity are associated with orbit tracks implying a spacecraft or atmospheric anomaly for those data rather than poorly modeled surface mineralogies. Detailed analyses of the non-olivine maps are ongoing and will be useful in examining refinements to the mineralogy of the surface enabled by including a wider compositional range of olivine spectral end-members.

In order to map the distribution of olivine in terms of surface abundance, we normalized the fractional contributions of the olivine spectral end-members to exclude the atmospheric and blackbody contributions to the spectra [Hamilton *et al.*, 1997; Feely and Christensen, 1999; Smith *et al.*, 2000]. We summed the abundances of all the olivine spectral end-members, binned the resulting total olivine abundance data at 2 pixels per degree and present maps of the mean value and standard deviation within each bin/pixel (Figure 7). The total mean olivine abundance map shows that materials containing 10 – 20% olivine are relatively common in the low-albedo regions of Mars and have clear regional variations (Figure 7a). For example, Syrtis Major shows less total olivine than Terra Tyrrhena directly to the south, the western third of Syrtis Major has mean olivine abundances almost ~10% less than central and eastern Syrtis Major, and the region northeast of Syrtis that contains the Nili Fossae has olivine abundances >20%. There are notably low standard deviations over most of Syrtis Major (Figure 7b) suggesting that olivine is modeled with similar abundances for the TES spectra within each bin. Broad regions of elevated olivine abundance with values >10% are observable in Tyrrhena, Cimmeria, Sirenum, and Xanthe Terrae. Within these regions, the map shows discrete occurrences (1 – 5 pixels across) with up to 20% total olivine abundance. The northern

and eastern rims of the Argyre and Hellas Basins also have localized enhancements of olivine; however, they also have elevated standard deviations, suggesting that both high and low abundances of olivine are modeled for spectra present in those bins and exposures of olivine may be smaller than the bin size in these regions. The data also identify regions of low olivine abundance, e.g. the olivine abundances <5% across much of central and eastern Acidalia and the region of southern highlands west of Hellas basin.

Approximately 6% of the pixels mapped from our linear deconvolution results show fractional contributions >0.05 for more than one composition of olivine suggesting that, at least in some locations, multiple compositions may be spatially coexistent. One possible explanation is simply that olivine of different compositions are spatially distinct but adjacent in the same TES footprint (~3 x 8 km); e.g., the boundary between two abutting lava flows. Another possibility is that olivine of different compositions is spatially mixed and interspersed; e.g., if olivine grains of different compositions are collecting together in a sedimentary basin. A third possibility is that different compositions of olivine are present in the same grains, e.g., chemical zoning, such as the thin Fe-rich rims over Mg-rich cores found in some Martian meteorites [*McSween and Treiman, 1998*]. Alternatively, the olivine detected may be of an intermediate composition relative to the end-members used and require more than one spectral end-member to properly model. These scenarios cannot be distinguished with remote sensing data alone and linear deconvolution requires an assumption of “checkerboard” mixing, which may be violated by zoned mineral grains. For simplicity in this work, we interpret

multiple olivine compositions modeled in the same TES spectrum as intergrain compositional variations.

We created abundance maps for the six olivine compositions in our end-member set (Fo₉₁, Fo₆₈, Fo₅₃, Fo₃₉, Fo₁₈, and Fo₁) to illustrate their individual distributions on Mars (Figure 8). Similar to the total olivine abundance map, we mapped the mean value in each 2 pixels per degree bin after normalizing the fractional contributions to remove the atmosphere and blackbody end-members. These maps illustrate not only the abundance of the olivine spectral end-members as a function of location, but also the wide range of Mg/Fe content in olivine interpreted from TES data. Globally, the two intermediate compositions, Fo₆₈ and Fo₅₃ dominate these maps at abundances >5%. However, the Fo₃₉ map also shows spatially coherent occurrences >5% when binned at this resolution. Abundance maps binned at 16 pixels per degree for the six olivine end-members used in this study show more detail than the figures presented here but are too large to be provided as auxiliary material. Therefore, we provide them online at http://www.higp.hawaii.edu/datasets/koeppen/JGR_TES_olivine.

Inspection of the 16 pixels per degree Fo₉₁ spectral end-member abundance map reveals that only a few small locations on Mars show spectral signatures matching the most forsteritic sample in our olivine suite, and most occurrences are not visible in the 2 pixels per degree maps. For example, the largest area modeled with Fo₉₁ olivine is <900 km² but exhibits Fo₉₁ abundances >10% in some spectra. THEMIS DCS images of the area show olivine-like signatures throughout the hills, massifs, and rim of a small crater (32.3°W, 44.2°S) that excavated into the Argyre rim materials (Figure 9). Other

occurrences of the Fo₉₁ spectral end-member appear as groupings of 4 – 8 pixels located almost exclusively in and around the northern rims of Argyre and Hellas basins.

The Fo₆₈ spectral end-member is the most common olivine spectral shape identified on Mars and has a distribution similar to the results of *Hamilton et al.* [2003], who used spectra of the Martian meteorites, including olivine-rich ALH A77005 and Chassigny, as spectral end-members. In both 2 and 16 pixel per degree maps, many spatially coherent occurrences of Fo₆₈ correlate with surface features at all scales including craters, channel floor materials, and volcanic plains. As in previous studies, the Fo₆₈ spectral end-member is the dominant composition of olivine within the materials in the region surrounding the Nili Fossae, and many of the pixels in that area show >10% Fo₆₈ content even at 2 pixels per degree (Figure 8) [*Hamilton et al.*, 2003; *Hoefen et al.*, 2003]. Fo₆₈ also occurs on the Isidis basin rim south of Syrtis Major [*Hamilton et al.*, 2003; *Hoefen et al.*, 2003], in knobs, mesas, and channel floor materials within many of the chasmata of the Valles Marineris, in the floor of Ares Vallis [*Rogers et al.*, 2005], north of Argyre basin, and in the floor materials of two craters in Aurorae Planum [*Hamilton et al.*, 2003]. The Fo₆₈ spectral end-member map shows broad spatially coherent occurrences north of Argyre and in Noachis and Tyrrhena Terrae (though notably less over Tyrrhena Patera). It is commonly observed in discrete occurrences between -60 and 30°N, and small groupings of 5 – 10 pixels occur in isolated mesas, crater floor materials of Sirenum, Aonia, Tyrrhena, and Cimmeria Terrae, Noctis Labyrinthus, Amazonis, north and northwest Hellas, east Argyre, Chryse Planitiae, and in the ridged plains southeast of Elysium Planitia. The Fo₆₈ spectral end-member is also

modeled globally in many isolated pixels, but we did not manually validate each occurrence using THEMIS data.

The Fo₅₃ olivine end-member map shows occurrences in numerous areas throughout the equatorial and southern highlands (Figure 8). The Fo₅₃ spectral shape is abundant in the region surrounding the Nili Fossae, though pixels modeled with Fo₅₃ olivine >10% are spatially confined to the northeastern portion of the area similar to the distributions of *Hoefen et al.* [2003]. Small occurrences <2 pixels across are located in the northern rims of Argyre and Hellas Planitiae; however, Fo₅₃ is not as pervasive as Fo₆₈ in these regions, and only rarely do both compositions have high values in the same pixel. Similarly, we observe the Fo₅₃ spectral end-member in the Valles Marineris floor materials and in the channel floors of Chryse Planitia coincident with Fo₆₈, but the abundances of Fo₅₃ are typically less than the abundances of Fo₆₈ in these regions. Finally, the Fo₅₃ spectral shape is present in numerous craters throughout the Sirenum, Noachis, Tyrrhena, and Cimmeria Terrae, many of which contain smooth interior materials at THEMIS scales (e.g., Figure 10).

The Fo₃₉ spectral end-member is less common than the Fo₆₈ and Fo₅₃ end-members in terms of areal distribution and abundance (Figure 8), and the Fo₃₉ spectral shape is identifiable in many of the atmosphere-removed spectra over these occurrences (e.g., Figure 11). The deconvolution results show broad occurrences of Fo₃₉ over Syrtis Major and much of the equatorial and southern highlands. Aonia, Xanthe, Noachis, Tyrrhena, and Cimmeria Terrae show Fo₃₉ abundances >5% and some locations have

abundances >10%. Almost all discrete enhancements of Fo₃₉ occur in the smooth-floored interiors of craters.

In general, derived abundances for the Fo₁₈ spectral end-member in TES data are less spatially coherent than those calculated for Fo₆₈, Fo₅₃, and Fo₃₉, and in fact appear somewhat randomly distributed at both the 2 and 16 pixel per degree resolutions. Many values >10% follow orbit tracks suggesting that atmospheric effects or noise may complicate identification of Fo₁₈ (Figure 8). Finally, a number of Fo₁₈ abundances >5% are commonly associated with identifications of other olivine end-members, making us less confident in the compositional precision of those results. We examined THEMIS DCS images over a number of small groupings of pixels that identified Fo₁₈, but none of the locations we checked showed the olivine spectral shapes in both TES and THEMIS data. Fo₁₈ is one of the few compositions found in TES data over high northern latitudes, and olivine was observed in OMEGA data of lobate crater ejecta in those regions [Bibring *et al.*, 2005]. However, even those locations identified by OMEGA data did not produce evidence of unambiguous olivine detections of any composition at the scale of TES observations. The lack of validated Fo₁₈ spectral end-member detections from TES does not preclude the presence of similar compositions on Mars, but our manual inspection of many individual TES spectra did not reveal any unambiguous occurrences of this spectral end-member.

Fayalite, represented by the Fo₁ spectral end-member, was modeled only at very low abundances except for a few isolated pixels (Figure 8). Although every case was not checked, most abundance values >5%, e.g. a group of pixels between Terra Tyrrhena and

Hellas Planitia, did not correlate with olivine-like spectral shapes in THEMIS data. However, ten TES spectra from OCK 6918 over an intercrater plain in the northern rim of Hellas Basin (62°E, 28°S) show very weak (~3%) fractional contributions of olivine that expand to >10% after conversion to abundance (Figure 12). These spectra appear noisy and show contributions less than our typical threshold of confidence, but the derived surface temperatures for the spectra are ~275 K and a Fo₁-like shape appears observable in the surface emissivity spectra (Figure 12b). Spectral variations identified in THEMIS DCS images over the potential occurrence indicate the presence of olivine in knobs and plains. This detection requires more analyses to ensure a confident detection of fayalite, but it is compelling enough to state that the presence of fayalite on the surface of Mars deserves further study.

3.3 Distribution of Olivine with Latitude, Elevation, and Age

We made histograms of the pixels mapped with >5% fractional contribution of each olivine spectral end-member to more clearly visualize the distribution of olivine by composition. First, we binned the data as a function of elevation to look for any trends in global stratigraphy. To avoid areal biases, we normalized each 100 m elevation bin by the total number of pixels containing usable TES data at that elevation, and the resulting data represent the percentages of pixels modeled with a specific olivine spectral end-member greater than our empirically determined detection limit (Figure 13). In general, the Fo₆₈, Fo₅₃, Fo₃₉, and Fo₁₈ spectral end-member histograms crest at -1000 m and taper off towards higher and lower elevations (the non-normalized elevation histogram of all

pixels mapped in this study crests at 2000 m suggesting that areal biases have been successfully removed). These histograms show that olivine is relatively common between -2500 and 2500 m, a range that includes most of the southern highlands and excludes the northern lowlands and most of Hellas basin. The only discrete stratigraphic enhancement in olivine fractional contribution is most visible in a 500 m thick peak at -2300 m to -1800 m in the FO_{53} histogram, but it is also visible in the FO_{68} , FO_{39} , and FO_{18} histograms. This elevation primarily corresponds to Xanthe Terra, a region the spectral end-member maps show to have elevated olivine of all compositions in both discrete (crater and channel floors) and regional occurrences. The histogram of the FO_{91} spectral end-member map shows that it is the least commonly modeled olivine composition at any elevation. The FO_1 spectral end-member is the second least common olivine modeled over the detection limit, less than 2% of pixels were mapped with $>0.05 FO_1$, and its histogram does not vary with elevation indicating that the pixels mapped as FO_1 are randomly distributed.

Second, we binned the data as a function of latitude to look for potential climatic influences on the surface mineralogy and normalized each one-degree latitude bin by the total number of pixels containing usable TES data at that latitude (Figure 14). The histograms of the FO_{68} , FO_{53} , FO_{39} , and FO_{18} spectral end-member maps all show that olivine is most common (4-12% of the pixels mapped) between $60^\circ S$ and $30^\circ N$, which correspond primarily to highland regions. The FO_{68} spectral end-member is the most common olivine mapped and contributes >0.05 to over 12% of the spectra at $10^\circ S$, tapering off towards the higher and lower latitudes. The peak in the FO_{68} histogram at

~22°N corresponds to the latitudes containing the Nili Fossae region. The Fo₁₈ histogram shows the highest percentages of spectra containing olivine at latitudes between 60°S and 45°S, and >30°N; however, we reiterate that none of the Fo₁₈ olivine identified by linear deconvolution or high spectral index values could be manually verified. Like the latitudinal histograms, the Fo₉₁ and Fo₁ spectral end-member maps show very few fractional contributions of olivine >0.05.

We plotted the locations where olivine was modeled over geologic maps of Mars to roughly estimate the age of the materials in which they reside [*Scott and Tanaka, 1986; Greeley and Guest, 1987*]. The Fo₉₁ spectral end-member, present in the rims of the ancient basins, lies almost exclusively within the Nplh and Nm units, the oldest geologic units on Mars. In the northern Hellas basin the Fo₉₁ signature also appears to occur on younger Hesperian plains (Hr) encroaching from Tyrrhena Patera, but inspection of DCS images show that the olivine signatures are commonly present in kipukas, older hills and massifs that are surrounded by smooth, younger-looking lava flows. The Fo₆₈ spectral end-member was modeled in materials with a wide range of mapped ages, but it was identified many times in Noachian cratered highlands and Hesperian channel floor units (e.g., Nplh, Nple, Npl₁, Npl₂, Hch, and Hcht). The age of the channel floor materials are particularly ambiguous because they may have been emplaced earlier in Martian history and exposed to impact cratering only in the Hesperian. The Fo₅₃ and Fo₃₉ spectral end-members are found throughout the southern highlands in a variety of Noachian and Hesperian-aged terrains; however, both compositions also appear at least locally concentrated within craters lying in Noachian terrains. These craters commonly have

smooth floors and appear to be filled in by lavas or sediment that are younger than the Noachian Fo₆₈-dominated intercrater plains by superposition. Although quantitative crater counts have not been done within the smooth-floored craters, typical examples (e.g., Figures 10 and 11) have only a few small (<2 km diameter) craters on their surfaces suggesting that their fill is Amazonian in age [*Hartmann and Neukum, 2001; Hartmann, 2005*], which coincides with the timing of volcanism implied by most of the Martian meteorites excluding Chassigny (180 Ma – 1.4 Ga) [*McSween and Treiman, 1998*].

4. Discussion

4.1 Comparisons to Previous Work

A few authors have explored the distribution of olivine on Mars using spectral index approaches. *Hoefen et al. [2003]* conducted a thermal infrared study of the composition of olivine in the region containing the Nili Fossae using spectral feature identification, which is essentially a complex spectral index. They found slightly more Fe-rich olivine compositions (Fo_{~70-40}) around the Nili Fossae than our index analyses (Fo_{~100-45}), which was expected because we mapped the highest Fo_# implied by valid index values. However, the olivine compositions found by *Hoefen et al. [2003]* in the Nili Fossae region are virtually identical to those found by our deconvolution analyses (Fo_{~75-50}), and the spatial distributions they mapped match up quite well with our deconvolution maps. Searching for smectite clays, *Ruff and Christensen [2007]* mapped the distribution of materials on Mars that have an emission minimum at 530 cm⁻¹, and one such material is olivine. The position of the 530 cm⁻¹ feature is outside the TES

spectral range that we analyzed by deconvolution because it is influenced by atmospheric CO₂, and the 530 index map gives a somewhat independent look at the distribution of materials that include olivine-rich locales [Ruff and Christensen, 2007]. However, although many of the small occurrences seen in their 530 index map are also observed in our 16 ppd total olivine fractional contribution and abundance maps, some areas highlighted by the 530 index are mapped as relatively olivine poor (e.g., Syrtis Major) suggesting that methods that discriminate multiple spectral features (e.g., spectral feature fitting or linear deconvolution) are necessary to confidently identify olivine-rich areas.

The fractional contribution maps of Figure 6 are directly comparable to the mineral maps of *Bandfield* [2002]. In general, the results correlate rather well, however some differences exist. First, our results indicate fractional contributions of total olivine >20% whereas the olivine map of *Bandfield* [2002] shows enhancements only slightly >10%. This difference is almost certainly due to the increased number of olivine spectra in our end-member set vs. those of *Bandfield* [2002], who only had access to spectra of Fo₉₁ and Fo₁ olivine compositions. Second, we modeled fractional contributions of 10-20% low-calcium pyroxene end-members throughout the southern highlands (Figure 6) compared to ~5% fractional contributions modeled by *Bandfield* [2002]. This may be due to our inclusion of pigeonite and ALH 84001 spectral end-members, which were not used by *Bandfield* [2002]. High abundances of low-calcium pyroxene have not been a common result of previous studies using TES data; however, recent work by *Rogers and Christensen* [2007] also modeled low-calcium pyroxene as 5-15% and it may be more common than previously thought. Additionally, studies using OMEGA data have

concluded that many regions in the Noachian highlands contain low-calcium pyroxene [Bibring *et al.*, 2005; Kanner *et al.*, 2005; Mustard *et al.*, 2005], and many areas that contain high-calcium pyroxene are best modeled by a combination of both high- and low-calcium pyroxene [Mustard *et al.*, 2005].

We included TES data that exhibited a larger range of water ice opacities (<0.15) than many previous studies including those of Bandfield [2002] (<0.10). Additionally, Rogers *et al.* [2007] suggest that water ice opacities as low as 0.06 can affect the surface emissivity spectra. Less than 2.5% of the spectra selected for our analyses had water ice opacities >0.10 , but we verified that including these data would not adversely affect our mapped results. To do this, we created global fractional contribution and abundance maps of olivine using only spectra with water ice opacities from 0.10 – 0.15, and we compared them to maps made using spectra with water ice opacities <0.10 . There were very few (and very small) differences in the resulting values and spatial relationships of olivine making us confident that including those spectra do not significantly distort the global-scale distribution of olivine on Mars.

Our mean total olivine abundance map (Figure 7a) is similar to the olivine abundance map of McSween *et al.* [2006]. However, our map shows occurrences of olivine in the northern lowlands (e.g., Kasei Valles), across Terra Tyrrenna, and in central Noachis Terra that do not appear in their study. Many differences likely stem from our inclusion of the Fo₅₃ olivine spectral end-member, which was not available to McSween *et al.* [2006], and our inclusion of a larger number of TES spectra.

Rogers et al. [2007] mapped the distributions of fine scale differences in TES-derived global surface types, and *Rogers and Christensen* [2007] modeled the mineralogy of these global surface types using both linear deconvolution [*Ramsey and Christensen*, 1998] and least squares fitting with non-negativity constraints [*Lawson and Hanson*, 1974]. *Rogers and Christensen* [2007] used a group of olivine spectral end-members similar to *McSween et al.* [2006], but they too only reported only the total derived olivine content. Similar to the results of our work, these studies mapped surface types modeled with high olivine contents (10-15%) in Tyrrhena, Cimmeria-Iapygia, Hesperia, and Meridiani surface types modeled with low olivine contents (<5%) in the high latitudes such as Solis Planum and Northern Acidalia.

Poulet et al. [2007] mapped the distribution of forsterite and fayalite on Mars using spectral parameters (i.e., spectral indices) that utilized a one-micron band absorption in OMEGA data to infer the presence of olivine. They used OMEGA data to identify a number of olivine occurrences between -50 and 50° at a spatial resolution of 2 – 5 km/pixel (~12 – 32 pixels per degree) [*Poulet et al.*, 2007], and most of the olivine occurrences they identified appear to be corroborated by our study. They did not identify regional enhancements of olivine; however, by using spectral indices alone, olivine contained in mixtures may not be accurately identified [*Poulet et al.*, 2007] and modeling the abundance of olivine requires radiative transfer modeling [*Poulet and Erard*, 2004]. *Poulet et al.* [2007] appears to infer more abundant Fe-rich olivine on Mars than our study; however, the near infrared spectra of forsterite and fayalite are very similar, especially if the grain size of fayalite is smaller than the grain size of forsterite [*Poulet et*

al., 2007]. On the other hand, the distribution of Mg-rich olivine inferred from OMEGA data in the northeastern rim of Argyre [Poulet *et al.*, 2007] matches very well with the distribution of the Fo₉₁ spectral end-member that we infer from spectral indices and linear deconvolution modeling in that area.

Mustard and Cooper [2005] searched the Syrtis Major region for spectral variations in TES data which might correspond to slope differences observed in NIR data from the Imaging Spectrometer for Mars (ISM). ISM observations from the eastern portion of Syrtis Major have a relatively strong spectral slope compared to the western portion that have been interpreted as the presence of ferric cement and fine coatings of dust [Mustard *et al.*, 1993; Murchie *et al.*, 2000], or penetrative oxidation [Mustard and Cooper, 2005]. *Mustard and Cooper* [2005] interpreted virtually no differences in the TES data between the two parts of Syrtis Major leading them to additionally suggest that dust may have been redistributed between the two instruments' scientific campaigns. However, our maps show up to 10% more total olivine in the eastern portion of Syrtis Major than in the western portion implying that at least some TIR spectral differences are evident in TES data. Furthermore, if relatively Fe-rich olivine (a mix of the Fo₆₈, Fo₅₃, and Fo₃₉ spectral end-members) is more abundant in the east, perhaps it provides a mechanism to fuel penetrative oxidation in that region, giving rise to the NIR spectral slopes observed in ISM data.

There is not a clear correlation between the total olivine abundance nor Fe-content in olivine from our maps and the distribution of Fe on the surface from Gamma Ray Spectrometer (GRS) data [Taylor *et al.*, 2006]. For example, GRS data show that Syrtis

Major contains ~5% more Fe than Terra Tyrrhena directly to the south, a trend mirrored by higher Fo₃₉ contents over Syrtis and higher Fo₆₈ and Fo₅₃ contents over Terra Tyrrhena. On the other hand, Tyrrhena and Noachis Terrae show variations in Fe from GRS data that do not spatially correlate with maps of the total olivine or its individual compositions. Similarly, the fractional contributions of other Fe-bearing minerals such as pyroxene do not match up well with the distribution of Fe observed by GRS. The lack of correlation suggests that the top 100-500 μm of the surface measured by the TES may not be representative of the meter or so depth measured by GRS, or that the Mg/Fe content in olivine (and perhaps other minerals) is independent of the bulk composition of the near surface. One possibility that might explain this discrepancy is that oxides or weathering products enriched in Fe are more abundant in some regions, thereby increasing the total Fe content independent of the observed olivine content or its compositions.

4.2 Implications of Latitude, Elevation, and Age Correlations

Our analysis of olivine as a function of elevation reveals that, regardless of the data biases based on our albedo constraints, olivine is much more common in the mid-elevations of the southern highlands than in the northern lowlands, Hellas Basin, or Tharsis bulge. Additionally, olivine is most common near the hemispherical dichotomy boundary at -1000 m, an elevation that includes the floors of many outflow channels and related features, suggesting that olivine is more common in the once-buried materials that have been exposed there. Xanthe Terra, which has even more channels and outflow features at a slightly lower elevation, has a strong peak in the Fo₅₃ elevation histogram

(Figure 13) that may also stem from materials exposed in channels, or olivine-rich materials eroding from higher elevations. In either case, it is difficult to tell if these enhancements represent a semi-global olivine-rich layer or merely the region where olivine is most commonly exposed resulting from relatively recent geologic events. Interestingly, many of the regions at these elevations are subjected to relatively strong surface winds [Joshi *et al.*, 1997; Fenton and Richardson, 2001], especially during periods of high obliquity [Armstrong and Leovy, 2005], which could work both to expose olivine-rich surfaces and mechanically weather olivine grains in situ.

The latitude histograms of olivine (Figure 14) strongly suggest that there is at least some latitudinal control on the distribution of olivine. Olivine of any composition is virtually non-existent at latitudes poleward of 30°N, which corresponds to the highland-lowland dichotomy boundary. If the bedrock materials of the relatively young northern lowlands are inherently less mafic than those of the southern highlands [Bandfield *et al.*, 2000b], olivine may have never been present at all in the north. Alternatively, if olivine was present in the northern lowlands, it may now be heavily altered or covered in dust [Bibring *et al.*, 2006]. Olivine is also extremely uncommon at latitudes poleward of 60°S suggesting that olivine is not merely correlated with southern highland materials. If we disregard the histogram of the Fo₁₈ spectral end-member (and the peak in its latitude histogram at 50°S, because this composition could not be manually verified), then olivine becomes significantly less common poleward of 45°S – the latitude at which the porous Martian regolith is modeled to contain steady state ground ice [Mellon and Jakosky, 1995]. This region is characterized the constant (and balanced) process of sublimation of

ground ice to the surface and condensation of water vapor from below [*Mellon and Jakosky, 1995*], which could aid in the alteration of olivine grains in the southern latitudes. Distinguishing between these scenarios will require lithologic observations and mapping of northern lowland bedrock to determine if olivine was ever present, or is present and hidden, and/or kinetic modeling of olivine dissolution by water in an icy environment that includes sublimation and condensation.

The age of the olivine deposits can be used to place constraints on the origin and evolution of olivine as well as the climatic history of Mars. Olivine has been used to argue for a long-lived dry climate for much of Martian history [e.g., *Christensen et al., 2003; Hoefen et al., 2003*]; however, the presence of hematite, phyllosilicates, and sulfates indicates that at least some regions on Mars may have harbored episodic surface and/or groundwater [*Christensen et al., 2001b; Squyres et al., 2004; Bibring et al., 2005*]. A key discovery of the OMEGA instrument is the presence of phyllosilicate deposits in the ancient intercrater plains near the Nili Fossae that are overlain by olivine-bearing flows from Nili Patera [*Bibring et al., 2006; Mustard et al., 2007a*]. *Bibring et al.* [2006] interpret this stratigraphy as evidence of a global, long-lived “wet” climate during the early Noachian followed by a globally dry climate from the late Noachian until present day. However, we found olivine exposed in a number of locations mapped as early Noachian (e.g., Argyre Planitia, Hellas Planitia, and many intercrater plains) suggesting that some olivine-bearing materials may have been coeval with the phyllosilicate deposits mapped by OMEGA. If the olivine-bearing materials and phyllosilicates were coincident, it implies that the early Noachian, wet climatic conditions proposed by

Bibring et al. [2006] were not globally homogenous, or at least were not so wet as to alter all of the early Noachian olivine. More detailed geologic mapping of olivine-bearing materials and phyllosilicate deposits is necessary to more clearly reveal the geologic distribution and chronology of the two climate regimes.

4.3 Possible origins of olivine on Mars

Our maps can be used to identify relatively small occurrences of olivine, constrain their composition, and distinguish broad geochemical provinces. In turn, the distributions and compositions can give clues to the provenance and evolution of olivine and its host rock. In this section we explore possible origins of different olivine compositions on Mars.

The most forsteritic spectral end-member used in this study, Fo₉₁, was found in small occurrences within the rims of the Argyre, Hellas, and Isidis basins using both spectral indexing and deconvolution. Although this spectral end-member represents a range of Fo_# compositions (see section 2.3), it is clear that it indicates a more Mg-rich composition of olivine than is found in most Martian meteorites and nearly all of the Martian surface in general as observed by remote sensing. The nature of forsteritic olivine suggests that it may have come from a very early, undifferentiated magma source with a Mg/Fe ratio higher than we might expect given the high Fe content estimated for the Martian mantle [*Wänke et al.*, 1994; *Lodders and Fegley*, 1997]. However, if majoritic garnet was a significant early crystallizing phase in the Martian magma ocean, the residual liquid would have been enhanced in Mg [*Borg and Draper*, 2003]. The

presence of forsteritic olivine in the rims of the two largest impact basins on Mars as well as around the Nili Fossae, an area at the intersection of the Utopia and Isidis basins, suggests a relationship between that composition and the formation of the impact basins; the impacts that formed the Argyre, Hellas, and Isidis basins may have excavated deeply enough to expose mantle materials. However, the abundance of the Fo₉₁ spectral end-member in these occurrences (~10%) is lower than expected for rocks purely of mantle origin, and the olivine-bearing materials there may be partially eroded or mixed with crustal materials as impact breccia.

The areas in which Fo₉₁ spectral end-member is identified are ancient and geologically complex. For example the olivine-rich materials near the Nili Fossae have been suggested to be the result of igneous intrusives [*Hoefen et al.*, 2003], subaerial flows [*Hamilton and Christensen*, 2005], and Isidis-related impact melt [*Mustard et al.*, 2006]. The diversity of olivine compositions identified near the Nili Fossae suggests that perhaps all these processes have occurred in the region. Forsterite is up to ten times more resistant to low-temperature weathering by water than fayalite [*Wogelius and Walther*, 1992; *Stopar et al.*, 2006], which may have played a part in its long-term preservation in the proximity of more Fe-rich, and potentially younger, olivines. Detailed studies of these locations may reveal clues to the nature and composition of the mantle at the time of basin formation.

The compositions of the Fo₆₈ and Fo₅₃ spectral end-members closely resemble the composition of olivine in most Martian meteorites [e.g, *McSween and Treiman*, 1998] as well as observations from MER [*McSween et al.*, 2006], and they are the most widely

distributed compositional range on Mars. If the materials that bear the Fo₆₈ and Fo₅₃-like spectral signatures are petrogenetically related to the Martian meteorites as their olivine-composition suggests, it points to a single process that created most of the olivine-bearing materials on Mars. Work by *Borg and Draper* [2003] has shown that the chemistry of the Martian shergottites can be modeled by melting a depleted component of the Martian mantle and adding trapped late stage liquid interacting with the cumulate stack, and perhaps this process formed the parent magmas of all the materials bearing the spectral signatures of Fo₆₈ and Fo₅₃. The Fo₆₈, Fo₅₃, and Fo₃₉ spectral end-members are found in broad occurrences throughout the highlands (Figure 8), and discrete occurrences are found in channels, chasmata, intercrater plains, and smooth crater floors. Although there are exceptions, Fo₆₈ is the most common spectral end-member found in the chasmata, channels, and intercrater plains, whereas Fo₅₃ is more common in the smooth crater floors. Discrete occurrences of the Fo₃₉ spectral end-member are found exclusively within smooth crater floors. This may suggest that the Fo₆₈-like olivine is a more dominant constituent of intrusive or buried extrusive materials being exposed in the chasmata and channels, and of crustal surface materials as a whole. Slightly more Fe-rich olivine (represented by the Fo₅₃ and Fo₃₉ spectral end-members) is more common in lava or sediment filled craters.

The relatively Fe-rich Fo₃₉ spectral end-member is less common in our deconvolution results than Fo₆₈ or Fo₅₃, but it still has significant fractional contributions to TES data in spatially coherent occurrences (Figure 8). The presence of olivine this Fe-rich is enigmatic compared to the more Mg-rich compositions typical of olivines found in

the lherzolitic shergottites, Fo₇₆₋₆₀, [McSween and Treiman, 1998] or compositions typical of olivines in ultrabasic terrestrial rocks, Fo₉₁₋₈₆ [Deer et al., 1992] such as those commonly erupted from Mauna Loa [e.g., Garcia et al., 1995]. However, Fe-enrichment of olivine is not entirely unexpected as the Martian mantle is thought to contain more FeO than that of Earth by at least a factor of two based on measurements of the density and moment of inertia of Mars [Wood et al., 1981; Bertka and Fei, 1998a; b] and estimates of its bulk composition [Wänke and Dreibus, 1988; Longhi et al., 1992; Lodders and Fegley, 1997; Taylor et al., 2006]. Additionally, the MER Spirit measured some average olivine compositions as Fe-rich as Fo₄₀ [McSween et al., 2006]. The disconnect between the compositions of olivines measured in Martian meteorites and those measured here by remote sensing echoes the conclusions of Hamilton et al. [2003], that the Martian meteorites likely are not representative of the surface as a whole.

We did not confidently identify the Fo₁₈ and Fo₁ spectral end-members on the Martian surface at the spatial scale of the TES observations above our detection limits. In terrestrial settings, Fe-rich olivines are constituents of alkaline and acidic plutonic rocks but only occur in small amounts in volcanic rocks [Deer et al., 1992], and they do not form at all if there is water present in the magma. The formation of magnetite in a magma, which is controlled by the oxygen fugacity in the melt, can also remove Fe from the liquid and prevents the formation of high-Fe olivines. Fayalite is found in banded iron formations, but occurs as the result of high-grade metamorphism [Klein, 1983; 2005], a process not yet identified on Mars. In Martian rocks, olivine in some Martian Nakhrites and has compositions as Fe-rich as Fo₃₀ to Fo₁₇ composing up to 15% of the

rock [Friedman Lentz *et al.*, 1999]; however, the Fe-rich (Fo₁₇) compositions are only found in the rims of more magnesian olivines [McSween and Treiman, 1998]. A more detailed search through those spectra identified as containing the Fo₁₈ or Fo₁ spectral shapes may reveal confident identifications of these compositions, but if these Fe-rich olivines are present on Mars, they are relatively rare on its surface.

4.4 Comparison to a Model of the Martian Mantle

The olivine compositions we have observed on Mars can be compared to the compositions predicted by modeling of the mantle's formation. Recent models by *Elkins-Tanton et al.* [2005] propose a scenario in which Mg-rich olivine forms in a magma ocean and sinks to the core-mantle boundary, thereby enriching the residual magma in Fe. Subsequently forming (and sinking) olivine crystals are increasingly Fe-rich as well as increasingly dense. The resulting density profile is gravitationally unstable and will reorganize to achieve a gravitationally stable interior placing Mg-rich olivine near the surface and Fe-rich olivine at depth [Elkins-Tanton *et al.*, 2005]. In this scenario, the Mg-rich olivine we observe in the rims of Argyre and Hellas Basins may represent olivine-bearing materials excavated from the top of the mantle after overturn was completed. However, the ubiquity of relatively Fe-rich olivine in the current Martian crust requires a more complex scenario. According to the post-overturn model, olivines as Fe-rich as the Fo₅₃ and Fo₃₉ spectral end-members must have originated from very deep within the Martian mantle, but their widespread distribution on the surface would seem to require significant volcanism tapping the same layer on a global scale.

Alternatively, perhaps overturn was not complete or the entire mantle and crust did not participate in overturn; however, these scenarios are argued against using dynamical models [Elkins-Tanton *et al.*, 2005].

We suggest that overturn of the cumulate pile took place and all layers participated, but the resulting solid layers remained overlain by a leftover magma, which was relatively Fe-rich. After reorganization, the mantle from bottom to top would have consisted of a Fe-rich crystalline olivine layer, an Mg-rich crystalline olivine layer, a relatively Fe-rich liquid, and a secondary crust solidified from the Fe-rich liquid. In this scenario, the upper layer of the adolescent mantle, whether it overturned again or not, may have enriched the surface olivine in Fe to the degree we observe with TES. Observed occurrences of modeled basalt in the southern highlands that include the most Fe-rich olivines may then record the last vestiges of this Fe-enriched magma layer as it froze. Even if this scenario was not exactly reproduced, it is clear that magma ocean crystallization and overturn may have produced a complex, heterogeneous mantle with the variety of Mg/Fe contents we observe in the olivine of Mars.

5. Conclusions

Our deconvolutions of TES data used an expanded suite of intermediate composition olivine spectra and support previous work, which found that materials containing 10 – 20% olivine are relatively common throughout most of the southern highland surfaces of Mars. We identified a wide range of spectral end-members, Fo₉₁ to Fo₃₉, on Mars that exist at the spatial scales of TES observations and larger.

The total compositional range includes occurrences of olivine that are both more Mg- and Fe-rich than previously inferred from Martian meteorites and remote sensing. Occurrences of Mg-rich olivine occur almost exclusively in the ancient Noachian rims of large impact basins (Argyre and Hellas) and may represent primitive or re-homogenized mantle material; detailed studies of these locations could provide insights into the composition of the Martian mantle. Fo₆₈ and Fo₅₃ are the most commonly occurring spectral end-members, consistent with observations from MER and of Martian meteorites. These compositions are found in a variety of terrains, but are most common in outflow channel floors and smooth-floored craters. We identified olivine as Fe-rich as Fo₃₉ on Mars in both regional enhancements and discrete occurrences. The occurrence of this Fe-rich olivine spectral end-member at all suggests that some olivine-bearing materials on the surface of Mars may be more Fe-rich than indicated by the Martian meteorites. It also may suggest the existence of an early, Fe-rich magma layer that overlaid the overturned cumulate stack in an early Martian magma ocean and may have become a significant component of the Martian crust.

Olivine is most common in the southern highlands near the topographic dichotomy boundary, an elevation that contains many outflow channels exposing subsurface materials. Xanthe Terra, an area on Mars riddled with outflow channels shows a definitive increase in the pervasiveness of the Fo₅₃ spectral shape. These may represent semi-global, relatively olivine-rich layers, or be a result of the actions of outflows and strong surface winds that erode and abrade the areas.

Olivine is uncommon in the northern lowlands implying either that it was never present in the younger terrains of Mars, or it has been altered or covered by dust. Olivine also decreases in prevalence in the poleward of 45°S suggesting that latitudinal climate variations (e.g., the presence of steady state ground ice) may have played a role in weathering olivine out of the southern highland materials in those regions.

We correlated the olivine spectral end-members found in this study with their mapped geologic ages and found that olivine appears to have been brought to the surface throughout Martian history (early Noachian to Amazonian). If early Noachian olivine was coeval with the deposition of phyllosilicates and sulfates identified by OMEGA, it implies that the early climate of Mars was either (1) inhomogeneous, with both wet and dry regions existing on the surface simultaneously, or (2) the wet conditions required to produce the phyllosilicates and sulfates were not wet enough or long-lived enough to completely alter the olivine present on the surface of Mars today.

Acknowledgments

The authors wish to thank S. A. Morse for providing the olivine-rich mafic concentrates from which the pure olivine samples were extracted. J. Taylor, H. McSween, and M. Garcia added useful discussions and petrological insights to our results and interpretations. J. Bandfield and T. Hoefen produced thoughtful reviews that helped clarify and improve the manuscript. This research was supported by NASA grant NAG5-13421, and it is HIGP publication 1493 and SOEST publication 7165.

Tables

Table 1. Sample, Fo-number, particle size, and source of olivine samples used in this study.

| Sample | Fo _# | Part. Size (μm) | Reference |
|-------------|-------------------|-----------------|----------------------------|
| BUR-3720A | 91 | 710 – 1000 | Christensen et al. [2000b] |
| KI 3115 | 68.0 | 106 – 175 | Morse [1996] |
| KI 3362 | 60.4 | 175 – 246 | Morse [1996] |
| KI 3372 | 52.5 | 175 – 246 | Morse [1996] |
| KI 4143 | 38.8 | 246 – 355 | Morse [1996] |
| KI 3373 | 34.9 | 175 – 246 | Morse [1996] |
| KI 3352 | 25.0 | 175 – 246 | Morse [1996] |
| KI 3354 | 18.1 | 106 – 175 | Morse [1996] |
| KI 3008 | 9.7 | 175 – 246 | Morse [1996] |
| WAR-RGFAY01 | 1.22 ^a | 710 – 1000 | Christensen et al. [2000b] |

^aAlthough the WAR-RGFAY01 in the ASU spectral library is listed as fayalite, the Fo_# here is based on from our own microprobe analyses of the sample.

Table 2. Wavenumbers (cm⁻¹) and channels for each index value.

| Samples | ε ₁ | | ε ₂ | | ε ₃ | | Index |
|------------------------|----------------|------------|----------------|------------|----------------|------------|----------------------|
| Fo ₉₁ | 370.3 (22) | 380.9 (23) | 412.7 (26) | 423.2 (27) | 455.0 (30) | 465.6 (31) | Fo ₇₅₋₁₀₀ |
| Fo _{60/68} | 370.3 (22) | 380.9 (23) | 402.1 (25) | | 433.8 (28) | 444.4 (29) | Fo ₅₈₋₇₄ |
| Fo ₅₃ | 359.8 (21) | 370.3 (22) | 391.5 (24) | | 433.8 (28) | | Fo ₄₂₋₅₇ |
| Fo _{25/33/39} | 359.8 (21) | | 380.9 (23) | | 402.1 (25) | | Fo ₂₅₋₄₁ |
| Fo ₁₈ | 285.7 (14) | | 328.0 (18) | | 349.2 (20) | | Fo ₁₁₋₂₄ |
| Fo _{1/10} | 253.9 (11) | 264.5 (12) | 296.3 (15) | 306.8 (16) | 349.2 (20) | | Fo ₀₋₁₀ |

Values listed in parentheses are the TES channels corresponding to the wavenumber listed. If one value for ε is listed, the emissivity value at that band was used in the index calculation. If two values are listed, the average emissivity value for the two bands was used.

Table 3. Minerals that give high index values for each olivine index by composition.

| FO₇₅₋₁₀₀ | FO₅₈₋₇₄ | FO₄₂₋₅₇ | FO₂₅₋₄₁ | FO₁₁₋₂₄ | FO₀₋₁₀ |
|--|---|---|--|--|---|
| Dolomite ^a Mg ₅₄ Fe ₃₉ CO ₃ | Dolomite ^a Minrecordite Fe ₆₆ Mg ₃₄ CO ₃ FO ₅₃ Diopside Mg ₅₄ Fe ₃₉ CO ₃ | Dolomite ^a Minrecordite Fe ₆₆ Mg ₃₄ CO ₃ FO ₆₀ Magnesite ^a Mg ₅₄ Fe ₃₉ CO ₃ FO ₆₈ Diopside | Almandine Quartz Pyrope Meta-variscite ^a Dolomite ^a Magnesite ^a Minrecordite Kyanite Chlorite | Calcite ^a Apatite ^a Smithsonite ^a Kutnahorite Rhodochrosite FO ₂₅ FO ₃₅ | Calcite ^a Smithsonite ^a Rhodochrosite Flourite |

^aMultiple samples of these phases produced index values higher than the threshold

Table 4. List of end-members used for deconvolution analyses.

| End-member | Class | Sample ID | Reference |
|--|---------------|-------------------------------|------------------------------------|
| CO ₂ | Atmosphere | | <i>Bandfield et al.</i> [2000a] |
| Dust, low CO ₂ | Atmosphere | | <i>Bandfield et al.</i> [2000a] |
| Dust, high CO ₂ | Atmosphere | | <i>Bandfield et al.</i> [2000a] |
| Water vapor | Atmosphere | | <i>Bandfield et al.</i> [2000a] |
| Water ice cloud (high latitude) | Atmosphere | | <i>Bandfield et al.</i> [2000a] |
| Water ice cloud (low latitude) | Atmosphere | | <i>Bandfield et al.</i> [2000a] |
| Olivine, Fo ₉₁ | Olivine | BUR-3720A | <i>Christensen et al.</i> [2000b] |
| Olivine, Fo ₆₈ | Olivine | KI-3115 | <i>Hamilton et al.</i> [submitted] |
| Olivine, Fo ₅₃ | Olivine | KI-3372 | <i>Hamilton et al.</i> [submitted] |
| Olivine, Fo ₃₉ | Olivine | KI-4143 | <i>Hamilton et al.</i> [submitted] |
| Olivine, Fo ₁₈ | Olivine | KI-3354 | <i>Hamilton et al.</i> [submitted] |
| Olivine, Fo ₁ | Olivine | WAR-RGFAY01 | <i>Christensen et al.</i> [2000b] |
| Albite | Feldspar | WAR-0244 | <i>Christensen et al.</i> [2000b] |
| Oligoclase | Feldspar | WAR-0234 | <i>Christensen et al.</i> [2000b] |
| Andesine | Feldspar | BUR-240 | <i>Christensen et al.</i> [2000b] |
| Labradorite | Feldspar | WAR-4524 | <i>Christensen et al.</i> [2000b] |
| Bytownite | Feldspar | WAR-1384 | <i>Christensen et al.</i> [2000b] |
| Anorthite | Feldspar | BUR-340 | <i>Christensen et al.</i> [2000b] |
| Diopside | High-Ca Pyx | WAR-6474 | <i>Hamilton</i> [2000] |
| Augite | High-Ca Pyx | NMNH-9780 | <i>Hamilton</i> [2000] |
| Augite | High-Ca Pyx | NMNH-122302 | <i>Hamilton</i> [2000] |
| Hedenbergite, mangoan | High-Ca Pyx | DSM-HED01 | <i>Hamilton</i> [2000] |
| Pigeonite (Wo ₁₀ En ₃₆ Fs ₅₄ 33,34) | Low-Ca Pyx | | <i>Hamilton</i> [2000] |
| Enstatite | Low-Ca Pyx | HS-9.4B | <i>Hamilton</i> [2000] |
| Bronzite | Low-Ca Pyx | BUR-1920 | <i>Hamilton</i> [2000] |
| ALH84001 (Orthopyroxene) | Low-Ca Pyx | | <i>Hamilton et al.</i> [2003] |
| Gypsum | Sulfate | ML-S6 | <i>Lane</i> [2007] |
| Kieserite | Sulfate | C5492-1 | <i>Lane</i> [2007] |
| Anhydrite | Sulfate | ML-S9 | <i>Lane</i> [2007] |
| Quartz | Silica/Phyllo | BUR-4120 | <i>Christensen et al.</i> [2000b] |
| K-rich glass | Silica/Phyllo | | <i>Wyatt et al.</i> [2001] |
| SiO ₂ glass | Silica/Phyllo | | <i>Wyatt et al.</i> [2001] |
| Serpentine | Silica/Phyllo | HS-8.4B | <i>Christensen et al.</i> [2000b] |
| Illite | Silica/Phyllo | IMt-2 (granular) ^a | <i>Christensen et al.</i> [2000b] |
| Ca-montmorillonite | Silica/Phyllo | STx-1 (solid) | <i>Christensen et al.</i> [2000b] |
| Saponite | Silica/Phyllo | <0.2 μm ^b | <i>Michalski et al.</i> [2005] |
| Crystalline heulandite | Silica/Phyllo | | <i>Ruff</i> [2004] |
| Crystalline stilbite | Silica/Phyllo | | <i>Ruff</i> [2004] |
| Calcite | Carbonate | C40 | <i>Christensen et al.</i> [2000b] |
| Dolomite | Carbonate | C20 | <i>Christensen et al.</i> [2000b] |
| Hematite | Hematite | | <i>Bandfield et al.</i> [2000b] |

^aMinus 60% blackbody

^bPlus 60% blackbody

Figures

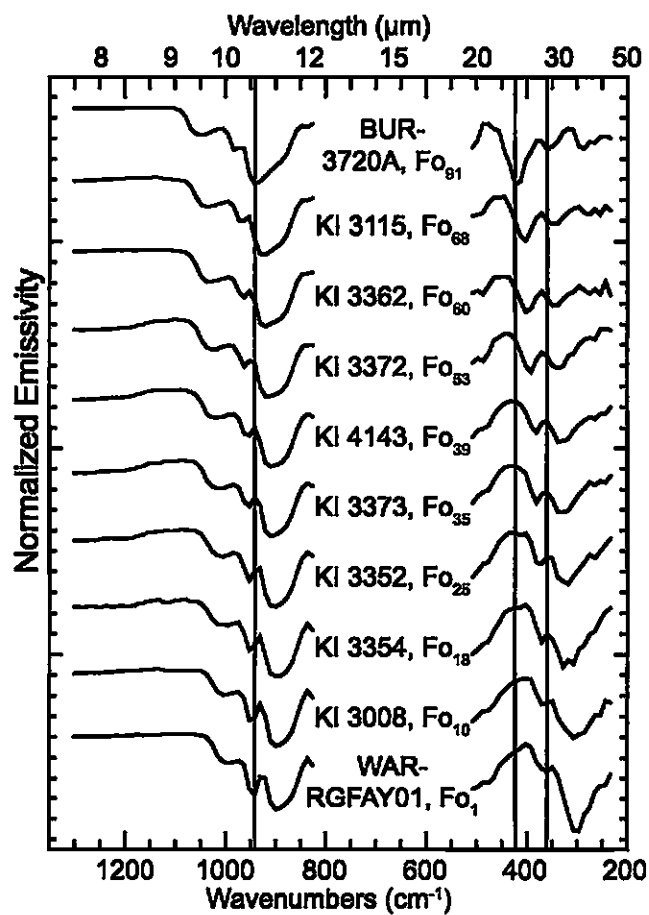


Figure 1. Thermal emission spectra of olivine samples at TES 10 cm^{-1} spectral sampling.

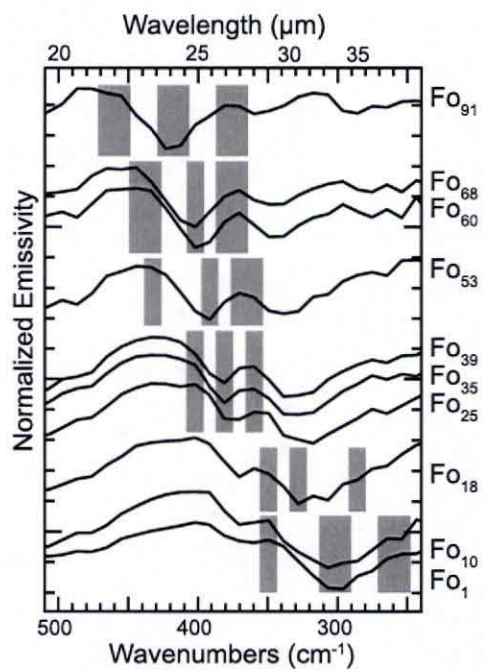


Figure 2. Position of bands used for olivine spectral indices.

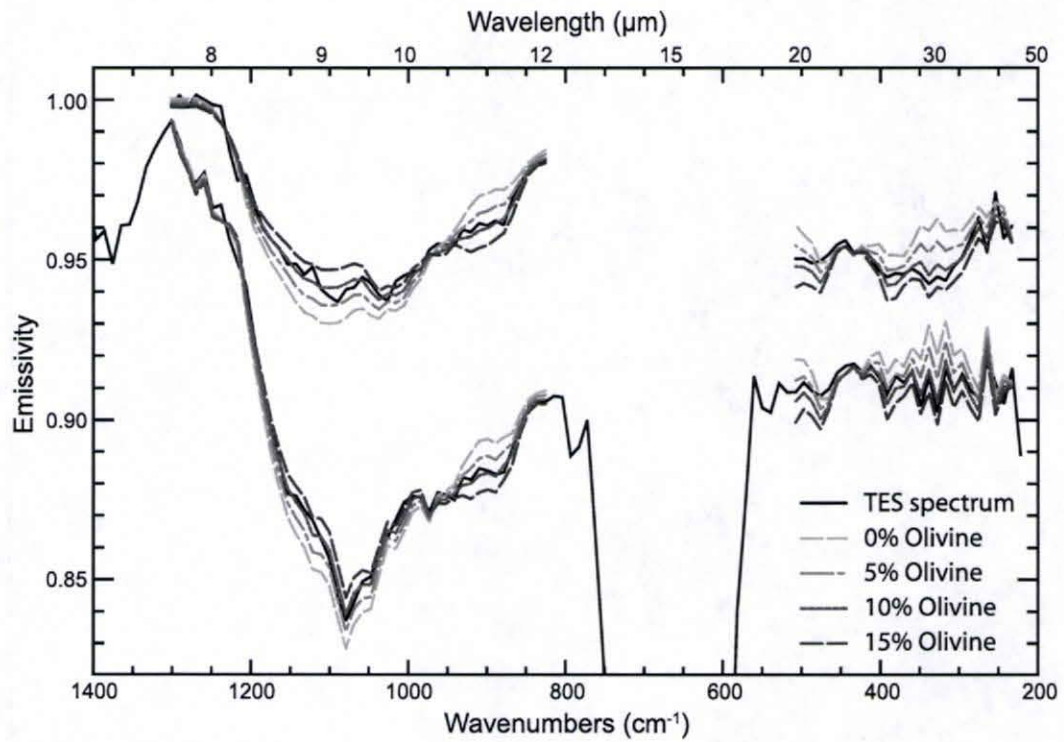


Figure 3. ICK-averaged TES spectrum from OCK 3740, ICK 1638. Lower spectra include the TES apparent emissivity spectrum and models with varying amounts of olivine. Upper spectra include the atmosphere-removed TES spectrum and its models. The best-fit model contains 10% olivine.

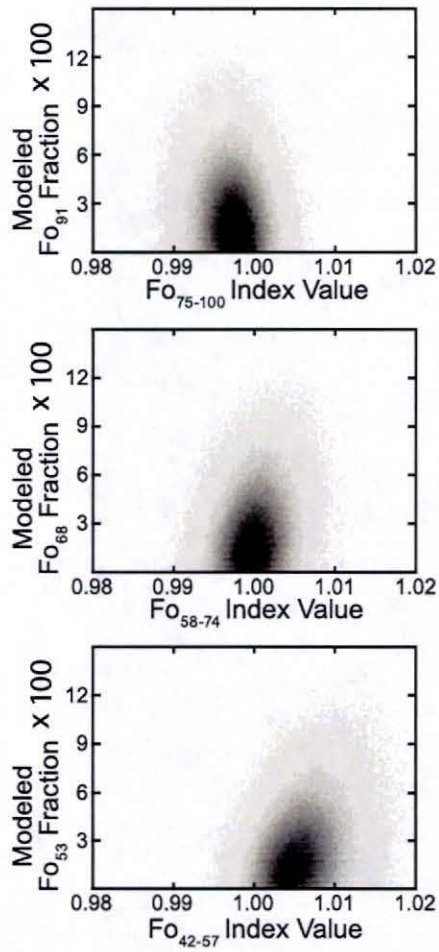


Figure 4. Density distributions of calculated index values vs. modeled olivine fractions from linear deconvolution. Color represents data densities from 5 (white) to >300 (black).

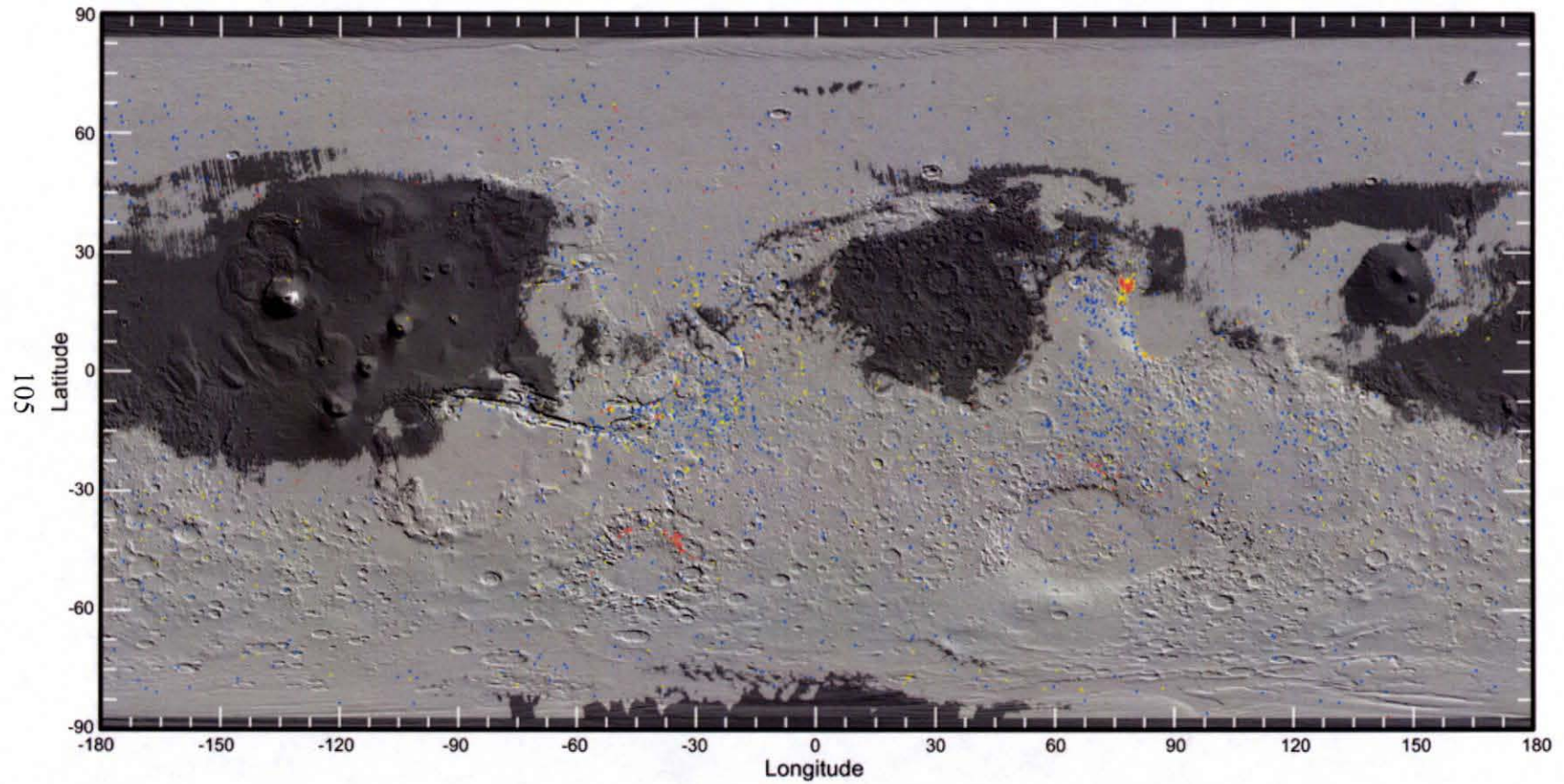


Figure 5. Index identifications of Fo₇₅₋₁₀₀ (red), Fo₅₈₋₇₄ (yellow), and Fo₄₂₋₅₇ (blue) olivine overlain on a MOLA global shaded-relief map. Points are shown larger than actual TES footprints; dark shaded regions have albedo >0.2.

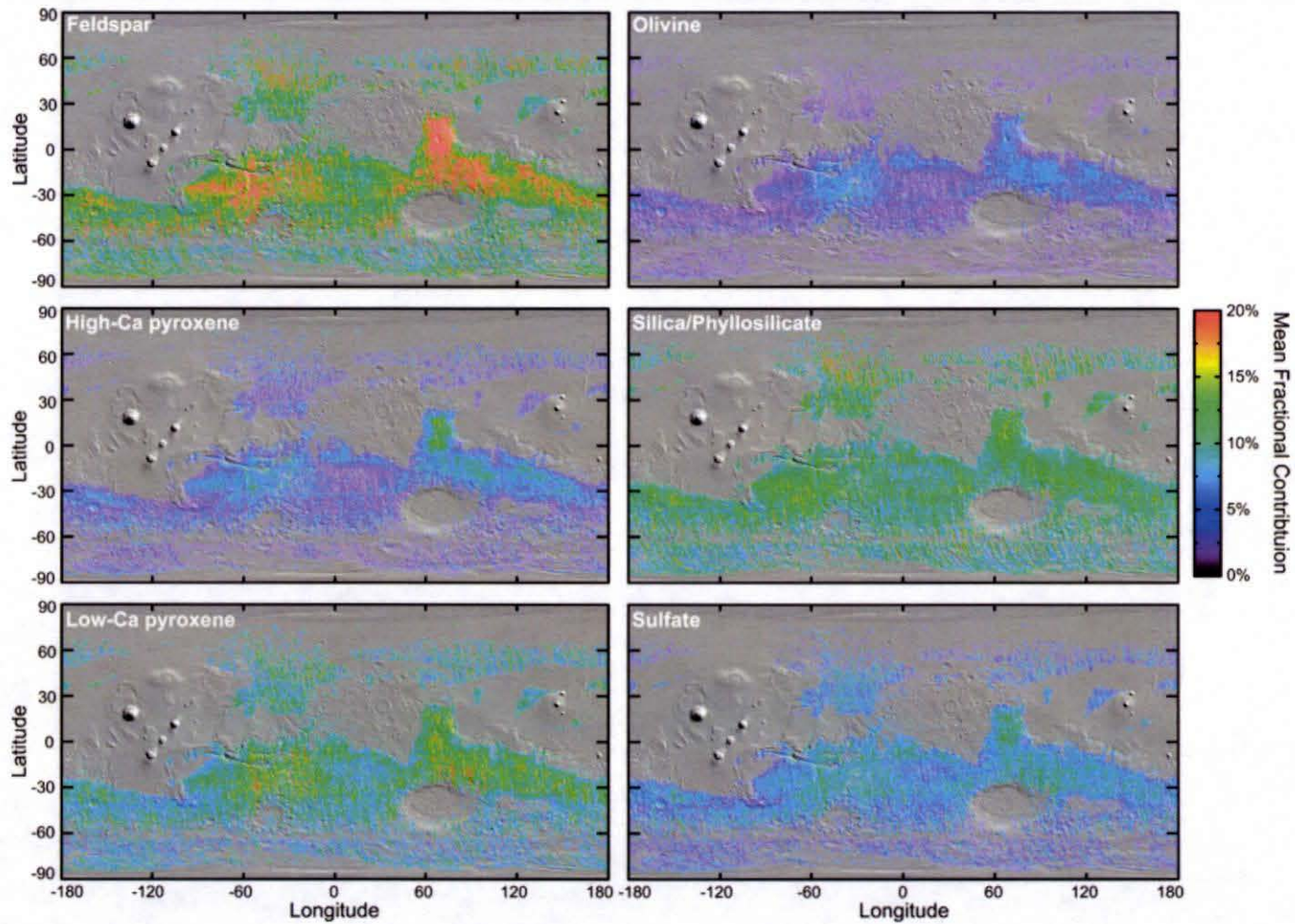


Figure 6. Mean fractional contribution maps of mineral classes binned at 2 pixels per degree for feldspar, high-calcium pyroxene, low-calcium pyroxene, olivine, silica/phyllosilicate, and sulfate.

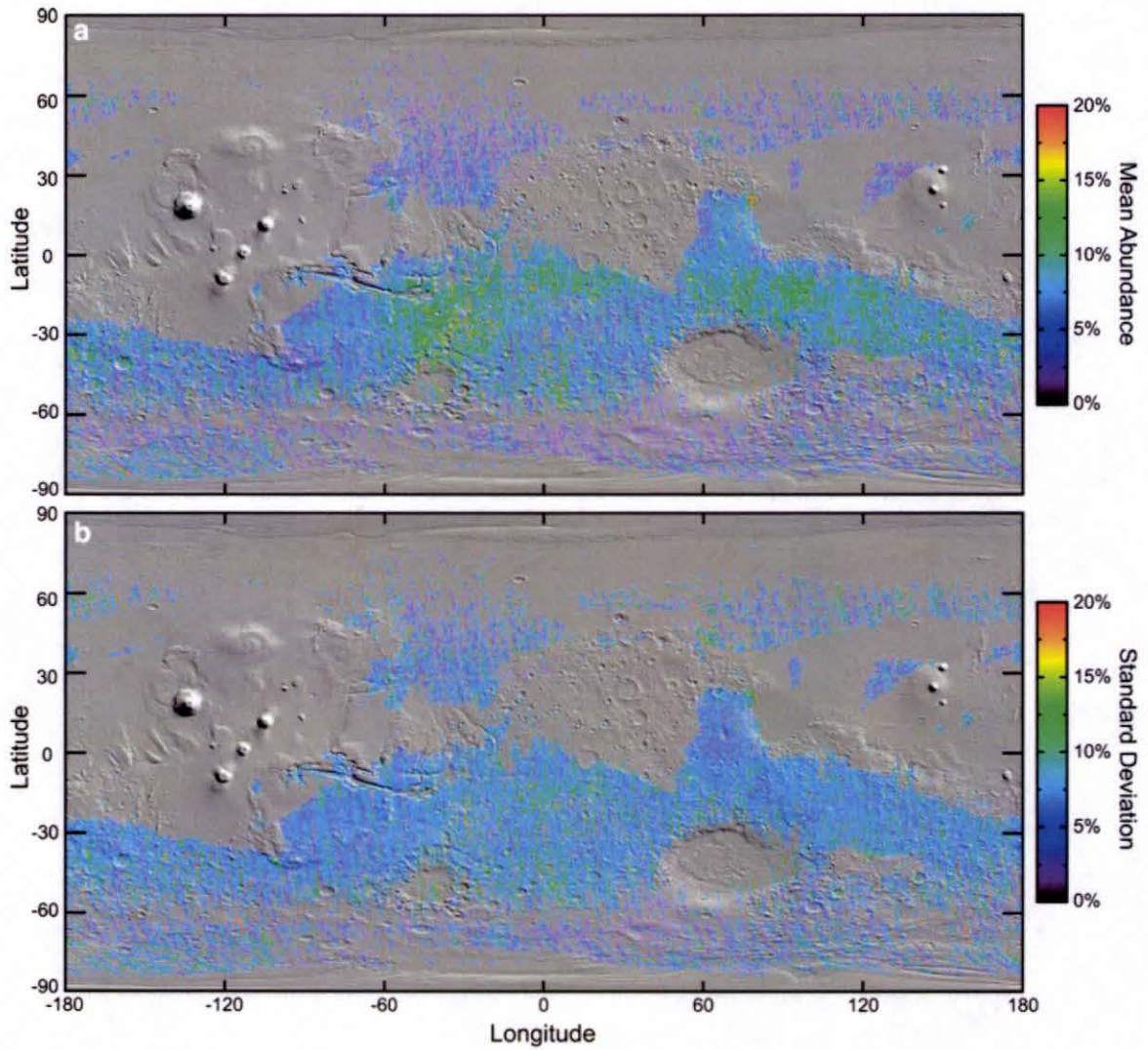


Figure 7. Two pixel per degree maps derived from deconvolution representing (a) the total mean surface-normalized abundance of olivine, and (b) the standard deviation within each pixel.

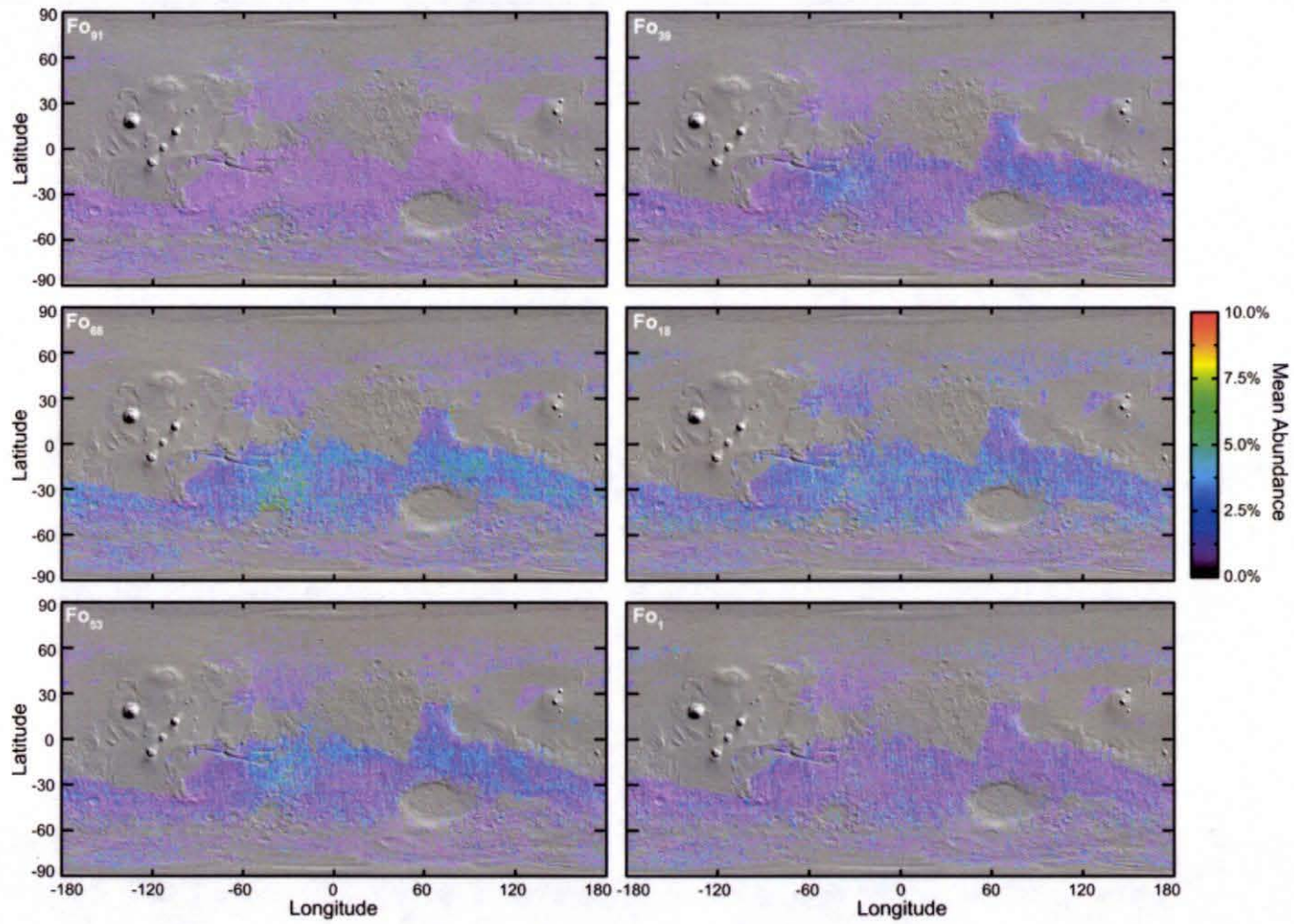


Figure 8. Mean deconvolved abundance maps of olivine spectral end-members binned at 2 pixels per degree.

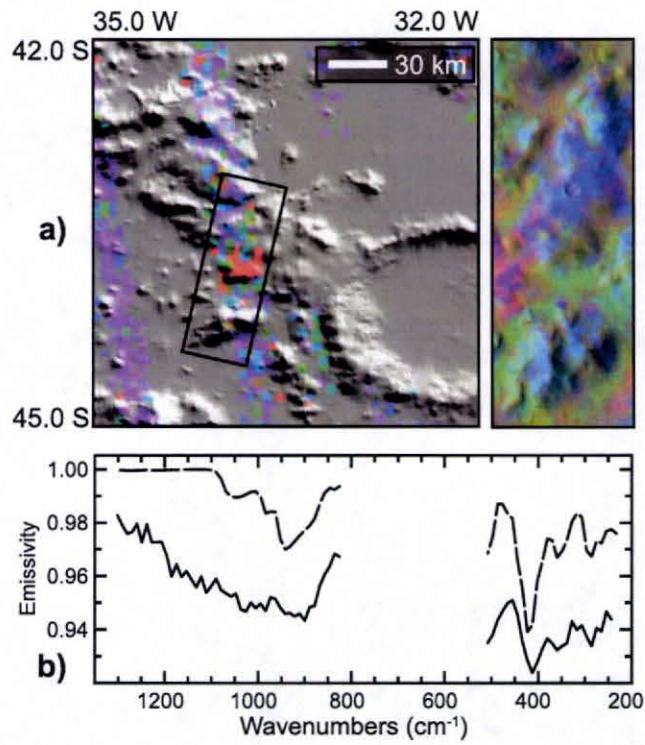


Figure 9. (a) TES-derived Fo_{91} olivine abundance stretched from 0 (purple) to $\geq 10\%$ (red) in Argyre Planitia with THEMIS DCS image I07991003, and (b) average of 10 atmosphere-removed TES spectra over the occurrence (solid) and the Fo_{91} spectrum scaled to 20% contrast (dashed).

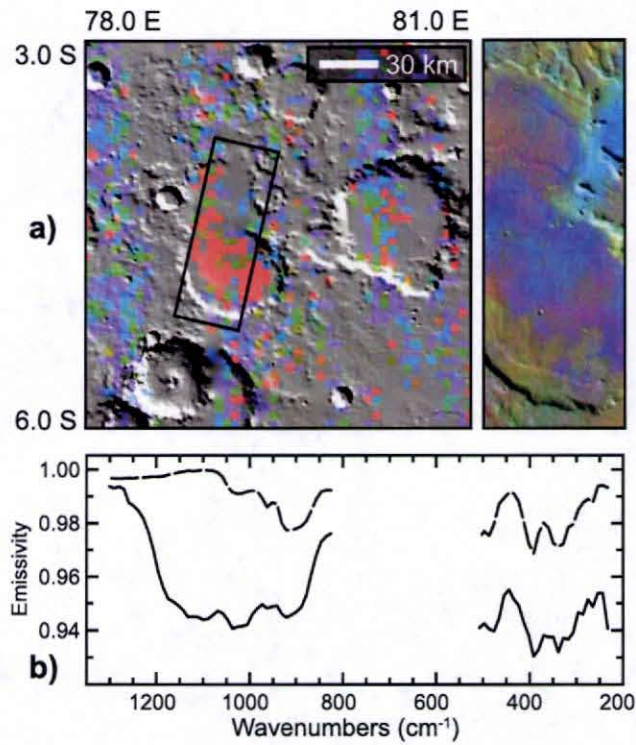


Figure 10. (a) TES-derived Fo_{53} olivine abundance stretched from 0 (purple) to $\geq 10\%$ (red) in a smooth-floored crater southwest of Syrtis Major with THEMIS DCS image I08186015, and (b) average of 18 atmosphere-removed TES spectra inside the crater (solid) and the Fo_{53} spectrum scaled to 20% contrast (dashed).

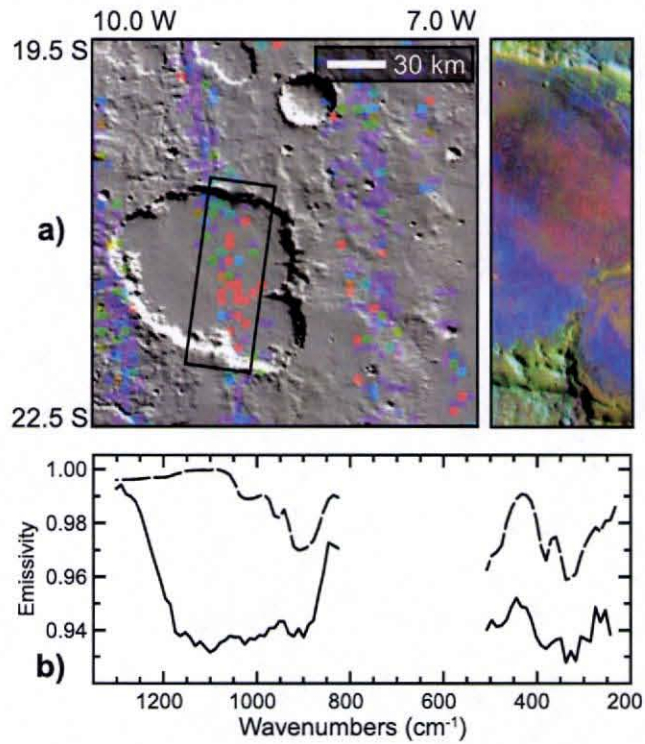


Figure 11. (a) TES-derived $F_{O_{39}}$ olivine abundance stretched from 0 (purple) to $\geq 10\%$ (red) in Noachis Terra with THEMIS DCS image I16851002, and (b) average of 41 atmosphere-removed TES spectra near 9 W, 22 S (solid) and the $F_{O_{39}}$ spectrum scaled to 20% contrast (dashed).

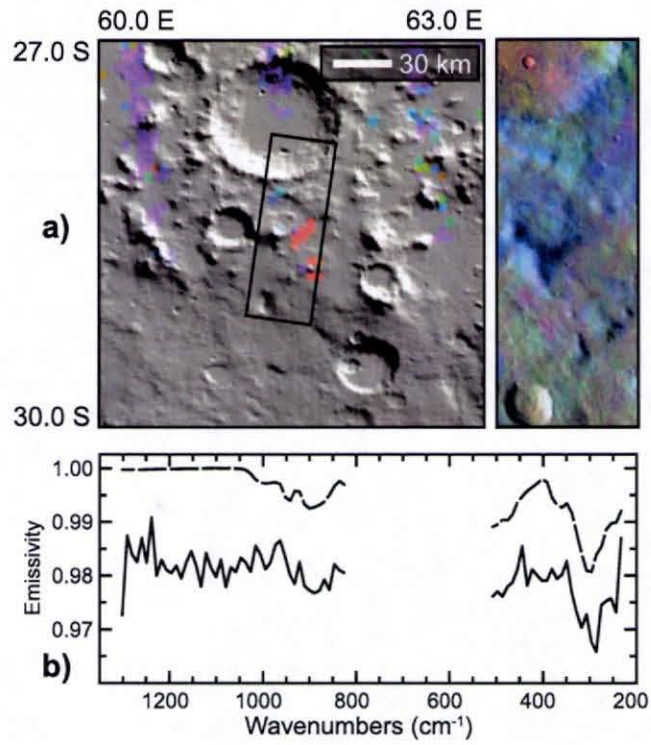


Figure 12. (a) TES-derived Fo_1 olivine abundance stretched from 0 (purple) to $\geq 10\%$ (red) on the northern rim of Hellas Basin with THEMIS DCS image I08587002, and (b) average of 10 atmosphere-removed TES spectra from OCK 6918 (solid) and the Fo_1 spectrum scaled to 5% contrast (dashed).

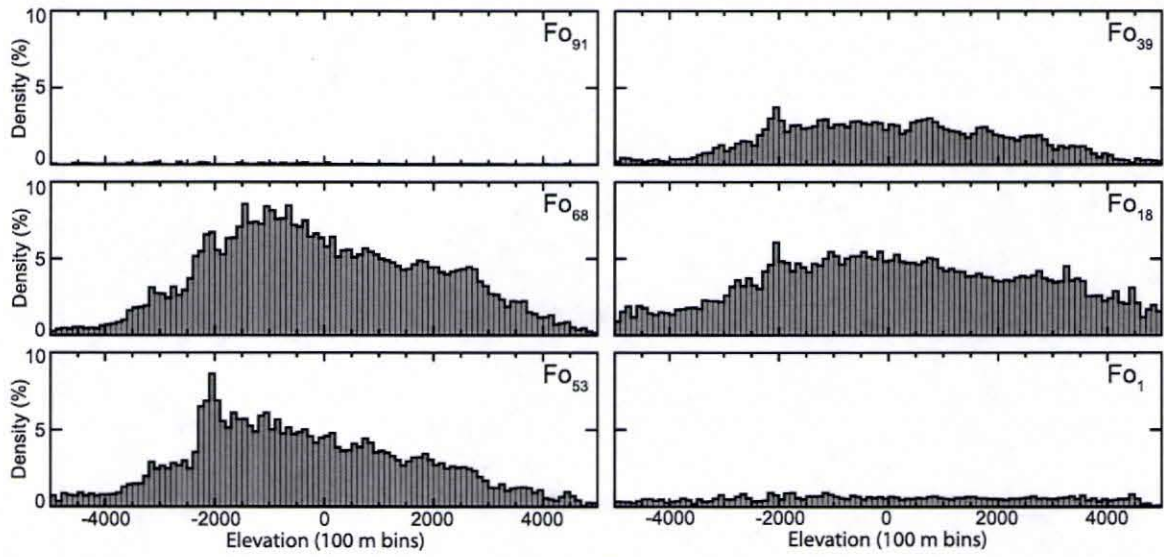


Figure 13. Densities of mapped pixels that have >5% fractional contribution of olivine binned by elevation.

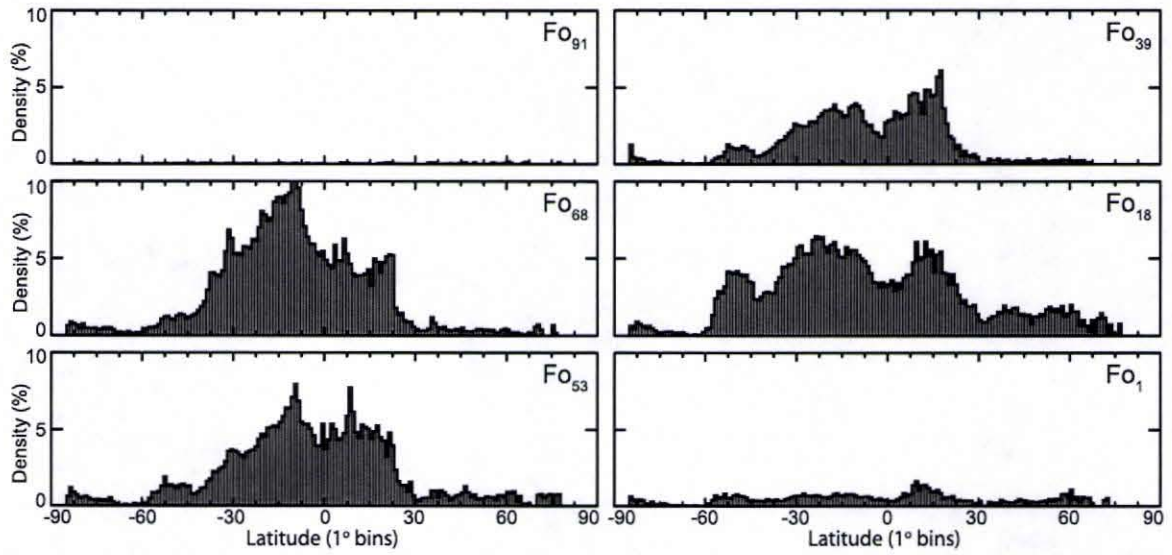


Figure 14. Densities of mapped pixels that have >5% fractional contribution of olivine binned by latitude.

**CHAPTER 4: THE GEOLOGIC SETTING OF OLIVINE-ENRICHED
MATERIALS IN TERRA TYRRHENA**

Abstract

We conducted a multi-dataset analysis of four relatively olivine-enriched locales in Terra Tyrrhena, each of which was identified by a different composition of olivine (FO_{91} , FO_{68} , FO_{53} , and FO_{39}) at abundances $>10\%$. Our geologic interpretation of each site encompasses its mineralogy, thermophysical properties, elevation, stratigraphy, and visual character. FO_{91} -enriched materials, found in only one location in Terra Tyrrhena, are interpreted as a thin layer of Noachian lava flows that tapped an undifferentiated magma chamber. Low abundances (5 to 10%) of FO_{68} are common across Terra Tyrrhena, and the FO_{68} -enriched locale we examined contained olivine abundances of up to $\sim 20\%$ present in alluvial fans; the presence of olivine constrains the total time of aqueous fan-building activity to $<\sim 40,000$ years. FO_{53} -enriched materials are interpreted as the volcanic Hesperian ridged plains unit, Hr, and may represent an extension of lavas more common to the north of Terra Tyrrhena. FO_{39} -enriched materials are rare in Terra Tyrrhena and appear to be post-Noachian lavas erupted into the floors of craters. The settings of the olivine-enriched materials we studied suggest that the surface of Terra Tyrrhena may have been more enriched in olivine before aqueous activity associated with the end of the Noachian. Noachian olivine exists in the surface materials of Terra Tyrrhena today either because it was protected in the subsurface during this period, or the total duration of aqueous activity was relatively short. Hesperian olivine was erupted after the abatement of regional aqueous activity and perhaps never interacted with liquid water.

1. Introduction

Terra Tyrrhena lies north of the Hellas basin and is a mixture of dissected Noachian highlands (Npld), Hesperian ridged plains (Hr), and Hellas rim materials that have accumulated over four billion years of geologic information about the Martian surface layer [e.g., *Leonard and Tanaka*, 2001; *Mest and Crown*, 2006]. Its terrains are representative of many southern highland terrains that lie circumferential to Hellas, which correspond to a large portion of the southern highlands as a whole. However, although numerous studies have been undertaken to understand the geomorphology of Terra Tyrrhena [*Greeley and Guest*, 1987; *Craddock and Maxwell*, 1990; *Leonard and Tanaka*, 2001; *Crown et al.*, 2005; *Mest and Crown*, 2006], they did not have available or did not incorporate compositional information.

Similarly, visible (VIS), near infrared (NIR), and thermal infrared (TIR) remote sensing observations reveal that olivine is relatively common on Mars and olivine-enriched materials (which we define here as containing olivine abundances >10%) make up many surfaces in the southern highlands [*Hamilton et al.*, 2003; *Hoefen et al.*, 2003; *Poulet et al.*, 2007; *Koeppen and Hamilton*, in press]. However, little work has been done to study and understand their provenance and evolution. *Koeppen and Hamilton* [in press] specifically identified Terra Tyrrhena as having numerous olivine-enriched occurrences, and they identified a wider range of olivine compositions there (Fo₉₁, Fo₆₈, Fo₅₃, and Fo₃₉) than anywhere else on the planet.

Olivine is a common and important rock-forming mineral in mafic igneous rocks throughout the solar system [e.g., *Mason*, 1981; *Brearley and Jones*, 1998; *McSween and*

Treiman, 1998; Papike et al., 1998], and it can be used to constrain the origin and evolution of the magma chambers that were the sources of igneous materials in Terra Tyrrhena. The most common igneous olivines exhibit a solid solution between Mg-rich forsterite ($\text{Mg}_2\text{Si}_2\text{O}_4$) and Fe-rich fayalite ($\text{Fe}_2\text{Si}_2\text{O}_4$), and the abundance and composition of olivine in such rocks is indicative of the chemistry of the magma from which it formed. Additionally, the grain size and abundance of olivine crystals in igneous rocks can be used to determine how long the magma took to cool and if the magma stagnated during its ascent and formed cumulates. Via remote sensing, the abundance and composition of various minerals, including olivine, can be used to distinguish rock units and petrogenetically relate diverse materials, which we will demonstrate for Terra Tyrrhena.

Previous workers have discussed the presence and composition of olivine in the southern highlands of Mars from a global standpoint using VIS/NIR and TIR data. *Hoefen et al. [2003]* used TIR data from the Mars Global Surveyor Thermal Emission Spectrometer (TES) to map the distribution of olivine in the Nili Fossae region, and they identified olivine with compositions of Fo_{~40} to Fo_{~70}. *Hamilton et al. [2003]* modeled data from the TES instrument with TIR emission spectra of Martian meteorites. They mapped materials with spectral shapes similar to Chassigny and ALH A77005 meteorites, which are dominated by the Fo₆₈ olivine composition, in Nili Fossae region as well as many other smaller locations. *Poulet et al. [2007]* used the VIS/NIR spectral differences between forsterite and fayalite to map spectral indices (parameters) representing Mg- and Fe-rich outcrops using data from the Mars Express Observatoire pour la Minéralogie,

l'Eau, les Glaces et l'Activité (OMEGA) instrument. They found areal concentrations of Mg-rich olivine in the low-albedo regions of Aonia Terra and Terra Tyrrhena as well as northeast of Argyre Basin, the western rim of Isidis basin, and in many craters in the southern highlands. *Koeppen and Hamilton* [in press] used TES data to map the global distribution of olivine using both spectral indices and numerical modeling to identify six compositions of olivine (Fo₉₁, Fo₆₈, Fo₅₃, Fo₃₉, Fo₁₈, Fo₁) on Mars. They identified Terra Tyrrhena, along with Cimberia, Sirenum, and Xanthe Terrae, as broad regions of olivine-enrichment with total olivine abundances >10%. *Koeppen and Hamilton* [in press] also found discrete occurrences of individual olivine compositions with abundances >20% in these regions suggesting diverse Mg/Fe contents of their source magmas.

To date, only a few olivine-enriched locales have been studied in detail including the region surrounding the Nili Fossae [*Hoefen et al.*, 2003; *Hamilton and Christensen*, 2005; *Mustard et al.*, 2007b], Ares Vallis [*Rogers et al.*, 2005], and exposures in southern Isidis Basin [*Tornabene et al.*, submitted]; however, none of these studies focus on olivine-enriched locales that are typical of the southern highlands where olivine is most common. The region surrounding the Nili Fossae is the largest exposure of olivine-rich materials on Mars [*Hamilton et al.*, 2003; *Hoefen et al.*, 2003; *Bibring et al.*, 2005; *Mustard et al.*, 2005] and occurs in the southern highlands despite its northerly latitude. However, the abundance of olivine and extent of olivine-enriched materials suggest that the Nili Fossae region is unique on Mars, and it may not be representative of smaller occurrences in the southern highlands. Materials in the Nili Fossae region typically contain olivine abundances of 20 to 30% [*Hamilton et al.*, 2003; *Hoefen et al.*, 2003] and

are spatially extensive, covering a region $>113,000 \text{ km}^2$ [Hamilton and Christensen, 2005]. Several mechanisms that may be broadly applicable to the southern highlands have been proposed for the olivine-enrichment near the Nili Fossae, including an igneous intrusive complex predating the Isidis impact [Hoefen et al., 2003], a layered stack of olivine-rich basalt flows [Hamilton and Christensen, 2005], and an impact melt sheet [Mustard et al., 2007b]. Exposures of olivine-rich materials in the Ares Vallis outflow system were studied by Rogers et al. [2005], and olivine-rich materials in southern Isidis Basin were mapped by Tornabene et al. [submitted]. Both studies used Mars Odyssey Thermal Emission Imaging System (THEMIS) multispectral data, TES hyperspectral data, and geologic mapping to make inferences about the presence, composition, and stratigraphy of olivine-enriched layers. Rogers et al. [2005] found a ~250 m thick olivine-rich rock layer exposed in the Ares Vallis channel wall as well as in isolated locations outside the channel, a finding that would not have been possible without mineralogical information from the THEMIS instrument. However, Ares Vallis and Isidis Basin are not globally representative terrains, and the formative processes described in those locations may not be applicable to the diverse occurrences of olivine-enriched materials in the southern highlands.

In this study, we examine the geologic setting of olivine-enriched materials in the southern highlands of Terra Tyrrhena (60 to 93°E, -30 to -10°N). We identified 25 discrete olivine-enriched occurrences in Terra Tyrrhena from the maps of Koeppen and Hamilton [in press], and we present four in detail here. We place the four sites in the regional context of Terra Tyrrhena by relating geologic mapping by previous workers to

the fractional contribution maps of *Koeppen and Hamilton* [in press]. We describe and compare the geologic nature of the materials in terms of regional mineralogy, thermophysical properties, relative age, and topographic and stratigraphic relationships, and we suggest a possible geologic history for each locale. Finally, we propose scenarios for the emplacement of olivine-enriched materials in Terra Tyrrhena that provide insights into the origin, evolution, and degradation of olivine in the southern highlands of Mars.

This work will add quantitative mineralogic information to the geology derived from visible images and topographic profiles over Terra Tyrrhena [e.g., *Greeley and Guest*, 1987; *Craddock and Maxwell*, 1990; *Leonard and Tanaka*, 2001; *Crown et al.*, 2005; *Mest and Crown*, 2006]. Integrating mineralogy derived from spectroscopy with traditional geologic mapping tools is a fundamental step towards further understanding Martian geology. This work demonstrates the utility of using spectral TIR spectral data to help relate and delineate geologic units in a regional context. It doubles the number of olivine-enriched sites on Mars that have been studied in detail with multiple datasets, and it is the first such study to be conducted on olivine-enriched sites typical of southern highland materials.

2. Data and Methods

2.1 Instruments

2.1.1 Mars Global Surveyor Thermal Emission Spectrometer (TES)

The TES instrument is composed of a Fourier transform Michelson interferometer, a TIR bolometer, and a VIS/NIR bolometer [*Christensen et al.*, 2001a].

The interferometer of TES consists of a 3×2 array of uncooled detectors, wherein each detector collects hyperspectral data from ~ 1650 to 200 cm^{-1} (~ 6 to $50 \text{ }\mu\text{m}$) in 143 or 246 channels (10 or 5 cm^{-1} spectral sampling, respectively) over a $3 \times \sim 8 \text{ km}$ area on the Martian surface. The TIR and VIS/NIR bolometers of TES also have 3×2 configurations of detectors and are bore sighted with the interferometer array. The TIR bolometer measures the integrated thermal radiance from 5.1 to $150 \text{ }\mu\text{m}$ and the VIS/NIR bolometer measures integrated solar reflectance from 0.3 to $2.9 \text{ }\mu\text{m}$. For a complete description of the TES instrument and its radiometric calibration, accuracy, and error, see *Christensen et al.* [1992; 2001a].

2.1.2 Mars Odyssey Thermal Emission Imaging System (THEMIS)

The THEMIS instrument on board Mars Odyssey contains VIS/NIR and TIR multispectral imagers [*Christensen et al.*, 2004a]. The TIR imager collects data in $1 \text{ }\mu\text{m}$ -wide bands centered at $\sim 7.9, 8.6, 9.4, 10.2, 11.0, 11.8, 12.6,$ and $14.9 \text{ }\mu\text{m}$ (~ 1475 to 670 cm^{-1}) and has a spatial resolution on the surface of Mars of $\sim 100 \text{ m/pixel}$. The THEMIS VIS/NIR imager collects data in five bands distributed from 0.425 to $0.86 \text{ }\mu\text{m}$ and has a spatial resolution of $\sim 18 \text{ m/pixel}$. A complete description of the THEMIS instrument can be found in *Christensen et al.* [2004a].

2.1.3 Mars Global Surveyor Mars Orbiter Laser Altimeter (MOLA)

The Mars Orbiter Laser Altimeter (MOLA) is a laser ranging instrument on board Mars Global Surveyor [*Zuber et al.*, 1992; *Abshire et al.*, 2000; *Smith et al.*, 2001].

MOLA emits a pulse from its 1.064 μm laser, and it records the time the pulse requires to travel from the spacecraft to the surface of Mars and back. Precise knowledge of the spacecraft's orbital trajectory is used to determine the planetary radius (elevation) at the location of the pulse reflection. Over smooth surfaces MOLA achieves estimates of elevation with errors of <40 cm, but errors may increase to ~ 10 m on 30° slopes [Abshire *et al.*, 2000]. Errors may also be higher in gridded data products where they interpolate through regions missing MOLA measurements (e.g., near the equator where cross-track distances are greater).

2.1.4 Mars Global Surveyor Mars Orbiter Camera (MOC)

The Mars Orbiter Camera is an imager that collects visible-wavelength data using one narrow angle and two wide angle cameras [Malin *et al.*, 1992; Malin and Edgett, 2001]. In this work we only utilize images from the narrow angle assembly, which provides images integrated over the 0.5 to 0.9 μm wavelength range at a high spatial resolution of ~ 1.5 to 3 m/pixel.

2.2 Data and Derived Products

2.2.1 TIR Spectroscopy of Minerals and Linear Least Squares Modeling

Fundamental vibrations in the molecular bonds and crystal lattices of most minerals absorb energy in TIR wavelengths, and emissivity spectra of minerals are diagnostic of their chemistry and structure. In the thermal infrared, the emissivity spectrum of a mixture (e.g., a rock) can be well modeled by a combination of the

emissivity spectra of its components (e.g., minerals) in proportion to their abundance [Lyon, 1959; Johnson *et al.*, 1983; Crown and Pieters, 1987; Gillespie, 1992; Thomson and Salisbury, 1993]. Linear least squares fitting has been developed to derive the compositions and abundance of minerals within rock mixtures from their emissivity spectra [e.g., Ramsey and Christensen, 1998; Staid *et al.*, 2001; Johnson *et al.*, 2003], and it is used by numerous authors to obtain quantitative mineral abundances of rocks under laboratory conditions [e.g., Hamilton *et al.*, 1997; Feely and Christensen, 1999; Hamilton and Christensen, 2000; Wyatt *et al.*, 2001] and on the Martian surface [e.g., Bandfield *et al.*, 2000b; Christensen *et al.*, 2000c; Hamilton *et al.*, 2001; Bandfield, 2002]. In previous work, we used linear least squares fitting to model the apparent emissivity spectra calculated from the TES instrument with surface and atmospheric components [Koeppen and Hamilton, in press]. In that work, we used the method of Ramsey and Christensen [1998] with modifications by Bandfield *et al.* [2000b] to determine the fractional contributions of 35 mineral components and 6 atmospheric components to single-scan TES spectra (143 channels, 10 cm^{-1} spectral sampling). The fractional contributions of mineral components were converted to surface abundances by subtracting the fractional contributions of atmospheric components to the TES spectra and normalizing the remaining (mineral) fractional contributions so that these surface-only components summed to unity [Smith *et al.*, 2000]. We presented global fractional contribution maps of feldspar, high-calcium pyroxene, low-calcium pyroxene, olivine, silica/phyllsilicate, and sulfate at 16 pixels per degree. We also presented global, surface-normalized abundance maps for the six individual olivine compositions (FO_{91} , FO_{68} , FO_{53} , FO_{39} , FO_{18} ,

Fo₁) and demonstrated that distinct compositions of olivine are distinguishable on the Martian surface. In this study, we use the mineral fractional contribution and abundance maps of *Koeppen and Hamilton* [in press] to examine the mineralogy of surfaces in Terra Tyrrhena.

2.2.2 Thermal Inertia and Maximum Effective Particle Size

Thermal inertia is the key property that governs the thermal response of a surface due to solar heating [*Jakosky et al.*, 2000; *Mellon et al.*, 2000]. It is controlled by the density (ρ), specific heat capacity (c), and thermal conductivity (κ) of the materials in the upper few centimeters of the surface [e.g., *Kieffer et al.*, 1977; *Mellon et al.*, 2000] and is defined as:

$$I = \sqrt{\kappa\rho c}$$

where thermal inertia (I) is in units of $\text{J m}^{-2} \text{K}^{-1} \text{s}^{-1/2}$ (which we abbreviate in this paper as “SI units”). However, under Martian surface temperatures and pressures the thermal inertia of particulates is controlled primarily by the thermal conductivity of the material [*Wechsler et al.*, 1972; *Jakosky*, 1986]. Thermal conductivity is in turn controlled by physical characteristics of the surface material such as effective particle size, exposure of rocks, porosity, and grain sorting [*Presley and Craddock*, 2006]. Therefore, the thermal inertia of a surface is indicative of the physical properties of the planetary surface such as particle size, rock abundance, degree of induration, etc. High thermal inertias are indicative of materials that can effectively store heat away from the Martian surface

during the day and release it at night [Mellon *et al.*, 2000]. A high thermal inertia is expressed by relatively low amplitude temperature changes on a planetary surface due to solar heating during the day and cooling during the night compared to materials with low thermal inertia. For example, materials with a high effective particle size and low porosity (e.g., rocks) have a high thermal inertia and display low amplitude temperature oscillations between day and night. Conversely, materials with a low effective particle size and high porosity (e.g., dust) have a low thermal inertia and display high amplitude temperature oscillations.

For this work we use thermal inertias calculated from the thermal bolometer of TES using the method of *Mellon et al.* [2000] and stored in the TES database. *Mellon et al.* [2000] uses a thermal model to generate a multi-dimensional lookup table relating values of latitude, time of day, season, albedo, surface pressure, dust opacity, and thermal inertia to a modeled surface temperature. The latitude, time of day, and season are derived from the position of Mars Global Surveyor at the time of observation, albedo is derived from daytime TES observations, surface pressure is estimated from MOLA data combined with a surface pressure model, and the IR dust opacity is assumed to be 0.1 [Mellon *et al.*, 2000, and references therein]. These data are combined with single nighttime temperature measurements to find the closest corresponding thermal inertia value, and a final thermal inertia for that location on the Martian surface is obtained by interpolation between the closest points in the table [Mellon *et al.*, 2000]. Thermal inertia values are also calculated for temperatures derived using a 20- μm band measured with the spectrometer of the TES instrument. However, spectrally-derived temperatures have

a higher uncertainty due to instrument noise [Christensen *et al.*, 1992], and variable, non-unity emissivity in surface units, which renders their corresponding thermal inertias less representative of the physical character of the Martian surface than those derived from the bolometer [Mellon *et al.*, 2000]. Current thermal inertia values in the TES database (used here) do not take into account recent updates including surface heterogeneity and layering modeled on Mars [Putzig and Mellon, 2007].

Presley and Christensen [1997] conducted laboratory studies on simple glass beads of varying sizes and compositions under Martian atmospheric conditions, and they showed that thermal conductivity of a material (κ , in $\text{W m}^{-1} \text{K}^{-1}$) on Mars is related to its particle sizes (d , in μm) and atmospheric pressure (P , in Pa) via the following equation:

$$\kappa = CP^{0.6}d^{-0.11 \cdot \log(P/K)}$$

where C and K are the empirically derived constants 0.0015 (no units) and 1.07973 pascals, respectively. This equation can be combined with the equation for thermal inertia and solved for d to obtain a direct relationship between a material's effective particle size and its thermal conductivity, density (ρ , in g/m^3), specific heat capacity (c , in $\text{J g}^{-1} \text{K}^{-1}$) and thermal inertia (I , in $\text{J m}^{-2} \text{K}^{-1} \text{s}^{-1/2}$, or SI units):

$$d = \left(I^2 / \rho c C P^{0.6} \right)^{1 / -0.11 \cdot \log(P/K)}$$

where ρc is $1 \times 10^6 \text{ J m}^{-3} \text{ K}^{-1}$ [Neugebauer *et al.*, 1971]. This relationship has been used to derive the particle sizes of units on Mars from thermal inertias measured from the Mini-Thermal Emission Spectrometer (Mini-TES) on the Mars Exploration Rovers [Fergason *et al.*, 2006]. Fergason *et al.* [2006] used a value of 600 Pa for the atmospheric pressure (P) based on the Martian surface pressure calculated at a subsolar longitude of 0° and -1.5 km elevation [Smith and Zuber, 1998], and that elevation is valid for most of our study locations in Terra Tyrrhena.

Caution should be used in deriving the effective particle size from remotely sensed thermal inertia values. Presley and Christensen [1997] note that materials with thermal inertias >350 SI units (~ 1.8 mm particle sizes) may be difficult to interpret and extrapolating their empirical relationship to higher values of thermal inertia can be presumptive. For example, at higher thermal inertias compaction of sediments, the abundance of large rocks, or partially exposed bedrock may complicate the distribution of sediments. Additionally, the relationship between thermal conductivity and particle size was initially developed with samples of uniform particle size and shape. However, Presley and Craddock [2006] re-tested this relationship with natural samples that had varying degrees of grain sorting. They found that the particle size calculated from thermal conductivity (and in our case, thermal inertia) is indicative of the largest particle sizes in the distribution rather than the mean particle size, and $\sim 90\%$ of the measured grains are smaller than d . With those caveats, we provide both the thermal inertia and the more intuitive maximum effective particle size for each area we analyze, as both provide

useful estimates of thermophysical properties and grain sizes between and within the sites we studied.

2.2.3 Decorrelation Stretched (DCS) Mosaics

Although TES spectra are useful for determining the quantitative mineralogy of relatively large areas (a TES spectrum covers $\sim 24 \text{ km}^2$), THEMIS is useful for mapping spatial variations as small as 0.01 km^2 in emissivity differences indicative of mineralogic differences. We highlighted the spectral signatures suggestive of olivine-enriched materials in Terra Tyrrhena by creating mosaics of decorrelation stretched THEMIS daytime TIR radiance images. In un-enhanced daytime TIR radiance images, variations due to emissivity differences are typically overshadowed by the comparatively large temperature differences due to sunlit or shaded facets of the terrain. However, these temperature effects are highly correlated between multiple bands returned by the THEMIS instrument, and differences due to emissivity can be enhanced independently of the highly correlated information [*Soha and Schwartz, 1978*]. Decorrelation stretching is one such color enhancement that exaggerates the contrast of uncorrelated multispectral information [*Gillespie et al., 1986; Gillespie, 1992*]. It involves the following steps: (1) a principal component transformation is performed on the multi-band images, (2) the transformed image bands with the highest signal-to-noise are contrast-enhanced to equalize their values, and (3) the principal component images are transformed back into radiance space and displayed, typically as 3-band false-color images [*Gillespie et al., 1986*]. Olivine is particularly suited to being identified in decorrelation stretched images

because it exhibits a strong and relatively narrow emission feature at ~ 10.65 to $11.25 \mu\text{m}$ [Salisbury *et al.*, 1991; Hamilton *et al.*, in prep.], which corresponds to the $11.0 \mu\text{m}$ band of the THEMIS TIR instrument. Although other surface minerals may also contribute to spectral variations at this wavelength, olivine appears to be the most common agent of spectral variability, and olivine-enriched materials are easily seen in decorrelation stretched images that include the $11.0 \mu\text{m}$ band [e.g., Hamilton and Christensen, 2005; Rogers *et al.*, 2005].

We selected THEMIS daytime TIR images for decorrelation stretching using simple temperature constraints, and we processed the images to remove sources of error and noise via the methods outlined in Bandfield *et al.* [2004b]. THEMIS daytime TIR images have the highest signal-to-noise when the surface is warm ($>245 \text{ K}$) compared to the atmosphere [Bandfield *et al.*, 2004b]. Most of the images we used show average temperatures $>245 \text{ K}$, but in order to achieve complete spatial coverage over some locations of our study areas, we needed to use data with surfaces as cold as $\sim 235 \text{ K}$. Decorrelation stretches using these images were not significantly different than higher temperature images, and we selected the images based on their lack of noise rather than strict temperature rules. Processing the THEMIS images included correcting for the time-dependent changes in the temperature of the THEMIS detector array known as “wobble”, as well as “drift”, which occurs because the instrument’s position is changing relative to the sun during the measurement [Bandfield *et al.*, 2004b].

We projected the processed images into a simple cylindrical Martian reference frame and created mosaics of the individual THEMIS image bands. The mosaicking

process makes slight adjustments to the spectral values of adjacent images (e.g., feathering) and manipulates the spectral contrast of each image in order to create a consistent areal scene. Even though we chose images for each mosaic that minimized the adjustments needed, this process makes the THEMIS spectra in the mosaic unusable for more quantitative spectral analyses such as linear least squares fitting. However, the method does lend itself well to creating relatively coherent decorrelation stretches over large areas. We created false color, decorrelation stretched (DCS) mosaics using the 11.8, 11.0, 9.4 μm wavelength THEMIS images (bands 8, 7, and 5) and displayed them as red, green, and blue channels, respectively. Spectral variations indicative of materials enriched in olivine show minima in the 11.0 μm (green channel) compared to the rest of the scene and appear purple or magenta in these images.

2.2.4 Elevation, Geology, and Visual Character

We used MOLA elevation data gridded at 128 pixels/degree (~ 460 m/pixel) to examine the regional and local stratigraphic relationships of different surface units. On regional scales we suggest stratigraphic relationships based on the elevation differences between sites by assuming that the layers of Terra Tyrrhena are, to first-order, horizontal or near-horizontal. At local scales, we made geologic cross-sections for some of the study areas based on topographic transects. Unfortunately, the orientation of the orbit tracks for Mars Global Surveyor did not correspond to any transects we examined, and transects in this study are based on the gridded elevation data. On these transects we plotted the

location of olivine-enriched materials observed in THEMIS decorrelation stretched images, which are geo-referenced to the MOLA dataset.

Geologic maps for Terra Tyrrhena provided a fundamental basis for placing the olivine-enriched materials in a regional and temporal geologic context. We compared the DCS mosaics, thermophysical properties, mineralogy from TES, and visual character to mapped age and geomorphology from *Greeley and Guest* [1987] and *Leonard and Tanaka* [2001], both of which are based on Viking Orbiter Camera images. Newer maps based on MGS data are available for some of the Terra Tyrrhena study region [e.g., *Mest and Crown*, 2006] and others are in progress, but none of the newer mapping efforts have overlapped the region where our four study sites are located.

High-resolution visual images were used to examine surface textures, weathering style, and contacts between units in Terra Tyrrhena. We utilized 0.654 μm (band 3) images from the THEMIS VIS/NIR camera [*Christensen et al.*, 2004a] and narrow-angle images acquired by the MOC [*Malin and Edgett*, 2001]. Images were selected and precisely located on the Martian surface using the JMARS data application [*Gorelick et al.*, 2003]. For this study, the projected images from both THEMIS and MOC were contrast enhanced to show surface variability and do not represent quantitative radiance or albedo values.

2.3 Study Site Selection

We chose four olivine-enriched sites in Terra Tyrrhena to study in detail with the combined datasets produced by TES, THEMIS, MOLA, and MOC. We first identified

25 spatially coherent, olivine-enriched occurrences in Terra Tyrrhena (60 to 93°E, 10 to 30°S) from the 16 pixel per degree total olivine fractional contribution map of *Koeppen and Hamilton* [in press] (Figure 1). Each location contains spatially coherent groupings of pixels with total olivine fractional contributions >0.10 that cover an area >150 km². We then compared these locations to the surface-normalized abundance maps of individual olivine compositions to determine the dominant composition of olivine at each olivine-enriched location. We surveyed the most distinctive sites in terms of olivine abundance that were associated with the Fo₉₁, Fo₆₈, Fo₅₃, and Fo₃₉ olivine compositions, and narrowed our analyses by selecting one site associated with each composition. We selected sites that show the geologic diversity of olivine-enriched materials in Terra Tyrrhena and attempted to select locations that were geographically close to each other; however, this was not possible with the Fo₅₃ olivine composition, which is found primarily in the north of Terra Tyrrhena. We also surveyed potential occurrences of Fo₁₈ and Fo₁ compositions; however, distinct occurrences of these compositions are rare in Terra Tyrrhena (and globally) [*Koeppen and Hamilton*, in press], and they occur only in low abundances and in conjunction with other olivine compositions. This makes the positive identification of Fo₁₈- and Fo₁-enriched materials suspect, and we do not discuss them here.

3. Results

3.1 Fo_{91} Study Area

Only one location in Terra Tyrrhena shows a distinct occurrence in the Fo_{91} olivine fractional contribution maps of *Koeppen and Hamilton* [in press], and it lies in the south of Terra Tyrrhena near the rim of the Hellas impact basin at 70.8°E, 24.0°S (Figures 1 and 2). The western third of the Fo_{91} study area is mapped as the rugged Noachian highland units Nh and Nm [*Leonard and Tanaka, 2001*]. The relatively smooth topography in the east is mapped as the smooth plains-forming unit Hpl₃ [*Leonard and Tanaka, 2001*], which regionally sits in a shallow (~700 m) topographic low that is ~800 km wide and ~1500 km long and extends from the Hellas Basin rim to the highland materials south of Syrtis Major. The smooth terrains of the Hpl₃ unit embay the rugged Noachian units as well as an unnamed, ~80 km diameter Noachian crater in the southwest of the study area at 71.8°E, 25.3°S [*Leonard and Tanaka, 2001*], referred to here as FO91A. The interior of FO91A contains smooth materials that were mapped as a geologic unit separate from Hpl₃ (AHps) [*Leonard and Tanaka, 2001*]. However, the morphology of a breach the crater's northern rim suggests that material flowed out of the FO91A, wrapped around small pre-existing knobs (Figure 3), and contributed to the Hpl₃ plains, implying that they are the same unit (Hpl₃).

The TES-based mineral maps of *Koeppen and Hamilton* [in press] suggest that most of the Fo_{91} study area contains 5 to 10% olivine (Table 1). The rugged Noachian terrains contain ~10% more feldspar and ~5% less olivine than the smooth Hpl₃ terrains. Olivine identified in the Fo_{91} fractional contribution map *Koeppen and Hamilton* [in

press] occurs with abundances as high as ~20% corresponding to the rims of two small craters at 70.8°E, 23.9°S, and one section of the rim of FO91A.

In the THEMIS DCS mosaic, olivine-enriched materials (identified by the purple/magenta color) are apparent in the two small craters and the section of the large crater identified by TES, but additionally they are observed in low knobs and hills located in the Hpl₃ plains and on the Hpl₃ unit in wispy strands. In the two olivine-bearing craters (white arrow, Figure 2), olivine-enriched material occurs from the top of their rims to where the crater floors are filled with smooth materials. The floor of the crater at 70.6°E, 23.9°S (referred to as FO91B) appears filled with a smooth unit that covers the crater rim to its north. The floor of the crater at 70.8°E, 23.8°S (referred to as FO91C) contains a small fan that has distributed olivine-poor materials from the adjacent massif onto the crater floor. However, no image data over the rims are available to determine whether olivine is present throughout the interior wall of FO91B and FO91C, or only in discrete layers with associated talus. The FO91A crater shows olivine-enriched materials in its rim (gray arrow, Figure 2), which appear to be eroding from resistant ridges and then dispersing into the crater (Figure 4A) and collecting in strands across the smooth Hpl₃ plains outside the crater. The olivine-enriched “wisps” appear to collect at topographic barriers. Like the rims of FO91B and FO91C craters, the olivine-enriched low knobs and hills (black arrows, Figure 2) also show olivine from their base to their peak. However, image data over one of the knobs suggest that olivine-enriched materials are associated with dark-toned materials that are eroding out of layers in the knobs and traveling down slope as a debris apron (Figure 4B). The apron covers the lower

exposures of the knob and the total thickness of olivine-enriched layers in the knob cannot be determined. Although the proximity and morphologic similarity of the hills to the FO91B and FO91C crater rims suggest that they are part of the same olivine-enriched unit, high-quality TES data over the knobs are not available, so the specific mineral abundances and compositions of the knob materials are not known.

The presence of debris aprons is problematic for determining the thickness of olivine-enriched materials in this area; however, topographic profiles based on the MOLA gridded elevation may provide some clues (Figure 5). For example, profile a-a' shows that the FO91B and FO91C are superimposed on irregular topography, and olivine-enriched materials must be eroding from the top of each rim peak to cover the entire rim with olivine-enriched debris (Figure 5A). If the tops of all three rims present in profile a-a' represent olivine-enriched layers that are approximately horizontal it provides a minimum estimate of ~900 m thickness for a package of materials that contain olivine. On the other hand, if the layers are not horizontal, they may be relatively thin (tens of meters) but must follow the pre-existing topography. Profile b-b' over four of the olivine-rich knobs (Figure 5B) shows that although the regional topography follows a very gentle slope ($<0.25^\circ$) climbing to the northwest, the peak elevation of the hills are surprisingly consistent over the ~100 km in lateral distance. Like the olivine in FO91B and FO91C, the olivine-enriched materials must come from near the top of each knob to cover it in debris (e.g., Figure 4B). The peak elevations overlap by ~200 m, which is another minimum estimate for the thickness of the olivine-enriched materials, assuming they are horizontal. However, a relatively thin olivine-enriched layer that was emplaced

on a slightly irregular surface could also lead to the same observations, and there is no upper bound for the olivine-enriched layer, leaving its thickness relatively unconstrained.

The Noachian units, Nm and Nh, typically display thermal inertias <300 SI units suggesting particle sizes of 0.9 mm and smaller in the Fo₉₁ study area. By contrast, the Hpl₃ unit shows thermal inertias >500 SI units, and values >600 SI units are common in the smooth materials of the FO91A crater and materials directly to the north that appear to have flowed out of the breach in the crater rim. These thermal inertias suggest large maximum particle sizes (over 1 cm) or a mixture of large cobbles and smaller particulates. The area containing the FO91B and FO91C craters has intermediate thermal inertias of 375 SI units and maximum particle sizes of ~2.4 mm. The olivine-enriched low knobs and hills are too small to be discriminated in the TES thermal inertia map.

3.2 Fo₆₈ Study Area

The largest and most distinctive occurrences of the Fo₆₈ olivine composition in Terra Tyrrhena are identified in the Saheki Crater, centered at 73.3°E, 21.7°S, and a nearby unnamed crater centered at 74.3°E, 23.0°S (Figures 1 and 6). Saheki Crater is ~85 km in diameter and the unnamed crater, which we refer to in this study as FO68A, is ~60 km in diameter. Both Saheki and FO68A are located in Noachian terrains (units Nh and Npld), but are filled with younger sediments [*Greeley and Guest, 1987; Leonard and Tanaka, 2001*]. The craters lie just inside a ~160,000 km² high stand of materials that rises 0.5 to 1.0 km above the smooth Hpl₃ plains to the southeast. However, the floors of

both craters currently sit ~2.5 km and ~1.0 km (respectively) below the level of the smooth Hpl₃ plains.

The mineral maps of *Koeppen and Hamilton* [in press] suggest that the materials inside of Saheki and FO68A contain ~15% more olivine and ~15% less feldspar than the materials that make up its ejecta (Table 1). Materials with total olivine abundances of ~20% occur in the western portions of both craters; however, high quality TES data over the eastern portions of the craters are not available and *Koeppen and Hamilton* [in press] did not map the mineralogy there.

The DCS mosaic of the FO₆₈ study area shows that the olivine-rich materials identified in *Koeppen and Hamilton* [in press] occur throughout the floors of both Saheki and FO68A, and confirms that olivine is relatively uncommon in the craters' ejecta (Figure 6). However, olivine is observed in small occurrences within the incised rims of the craters (gray arrow, Figure 6), and the troughs of the craters' rims appear to be the sources of large, olivine-enriched sedimentary fans that emanate into the craters (white arrows, Figure 6). Both Saheki Crater and FO68A were studied by *Moore and Howard* [2005] (labeled craters K and L in their work). They noted that channels on the fan deposits have their fine-grained side beds preferentially eroded compared to their coarse-grained central beds leading to relief inversion of the channels (e.g., Figures 7 and 8A). They interpreted the fans as fluvial rather than debris-fed based on the fans' length, branching sinuous channels, apparent presence of scroll bar deposits, and lack of armored flow lobes [*Moore and Howard*, 2005]. In FO68A, the floor is completely covered by a series of overlapping fans that have embayed the central peak of the crater from all sides.

In Saheki Crater, fans cover the western portion of its floor, but the eastern half is more heavily cratered and appears to have been protected from fans encroaching from the west by the crater's central peak complex (black arrow, Figure 6). The fans and the crater floor are morphologically dissimilar (e.g., Figure 8B), but both apparently contain olivine-enriched materials. Olivine-enrichment in this part of the crater floor could be due to eolian deposition of the nearby olivine-enriched fan materials, or the floor of Saheki Crater may have been enriched in olivine before deposition of the fans. Unfortunately, no image data are present over the eastern portion of Saheki's floor.

MOLA elevation data over the fans in Saheki Crater suggest that they bury the crater floor to a depth of 1200 m near their proximal ends, and their inverted relief suggests that they were even thicker at the time of emplacement. The fan shown in Figure 7 shows a slope of only $\sim 1.8^\circ$ that is consistent along the entire ~ 35 km length of the fan [Moore and Howard, 2005] until it meets the lowest part of the crater floor in the east. If olivine-enriched materials are found in both the apex region of the fans and in the crater floor and represent a homogenous unit, it may imply a ~ 2500 m package of materials. This package may contain discrete olivine-enriched layers amongst olivine-poor layers; however, each fan shows a uniform olivine distribution across its surface suggesting that the fans draw material from a homogenous source region. If the total fan area continuously covered by olivine-enriched materials (>2000 km²) is any indication of the volume of original materials derived from the fans' source regions, it suggests that such a thick estimate may be appropriate. However, a thinner package of materials that contain even higher olivine abundances than what we now observe ($\sim 20\%$), may also fit the

observations if aeolian transport has played a role in homogenizing olivine in the surface materials of Saheki and FO68A.

The fans and their source valleys have slightly elevated thermal inertia values of ~375 SI units (2.4 mm maximum particle size) compared to those of the surrounding plains at ~275 SI units (~0.65 mm), consistent with a higher resistance to weathering implied by the inverted relief of the fan deposits. The lowest part of the Saheki Crater's floor, which may predate the fans, has thermal inertia values >450 SI units, suggesting a component of large particle sizes (0.5 cm) or induration, making eolian homogenization of the olivine-enriched materials in the floors of Saheki Crater and FO68A less likely.

3.3 Fo₅₃ Study Area

The Fo₅₃ study area is in the northern part of Terra Tyrrhena (76°E, 11.5°S) (Figures 1 and 9), and consists of two irregularly shaped surface features that correspond to two isolated occurrences of the volcanically emplaced Hesperian ridged plains unit, Hr [Greeley and Guest, 1987]. All of the terrain on which the ridged plains units reside is mapped as the Noachian unit Npld by Greeley and Guest [1987], and they identified the east-west trending ridge that separates the ridged plains in this area (crossing Figure 9 at ~11.0° latitude) as being part of an escarpment over 1500 km long. The northern ridged plains unit abuts the escarpment and was mapped as the Hr unit by Greeley and Guest [1987]. They did not identify any ridged plains units south of the escarpment from Viking imagery; however, a shaded relief map based on MOLA topography shows that smooth ridged plains breach the escarpment in a number of locations, and we delineated

approximate boundaries of what we interpret as the Hr unit south of the escarpment in Figure 9. The ridged plains unit has relatively smooth surfaces compared to the Npld terrain and contain semi-parallel, arcuate, asymmetric ridges on their surfaces (white arrows, Figure 9). Palimpsests inside the ridged plains (e.g., Figure 10) appear to be craters that have been completely filled in by the ridged plains materials. Palimpsests outside the current border of the ridged plains show that the features were once more extensive, and the irregular borders of the ridged plains units suggest that the feature is in a state of erosion.

The Fo_{53} fractional contribution maps of *Koeppen and Hamilton* [in press] show that Fo_{53} -enriched materials are most abundant in the eastern portion of the southern ridged plains unit have olivine abundances of ~20% (Table 1). The Noachian (Npld) terrain of the escarpment has comparatively less olivine (~10%), but is otherwise mineralogically very similar to the ridged plains (Table 1). In fact, if olivine is removed from the model and the remaining mineral abundances renormalized, the composition of the Fo_{53} -enriched materials is indistinguishable from the Noachian escarpment.

The DCS mosaic shows that olivine-enriched materials in the Fo_{53} study area reside almost exclusively inside the bounds of the Hesperian ridged plains, and they are not observed in the Noachian terrains of the escarpment. Some olivine-enriched materials occur in the surrounding Noachian plains (e.g., to the west of the southern ridged plains unit near 77.0°E, 11.4°S); however, these occurrences appear to be remnants of the ridged plains unit that has since been eroded. In the northern ridged plains unit, olivine appears to be localized on and near the low ridges in the interior of the deposit,

whereas the southern ridged plains unit shows that olivine occurs most prominently in the topographically low east (black arrow, Figure 9). Olivine-enriched materials are not typical of the palimpsests; however, a few palimpsest craters near 76.1°E, 12.1°S contain olivine-enrichments (e.g., gray arrow, Figure 9 and shown in Figure 10). Compared to “olivine-poor” palimpsest craters, the olivine-enriched palimpsests are small, near the interior of the surface feature, and close to the olivine-enriched east of the southern ridged plains unit. Linear least squares modeling of TES spectra over the palimpsests suggests that they contain up to ~25% olivine.

The escarpment rises 400 to 800 m above the surrounding terrain, and its northern slope is steeper (~5°) than its southern slope (~1°), perhaps indicative of a thrust fault morphology. No elevation difference is observed between the Noachian plains on either side of the escarpment; however, the ridged plains units fill in the relative topographic lows on either side of the escarpment and may have equalized their elevation. We observe an embayment relationship on the north side of the escarpment that implies escarpment predates emplacement of the ridged plains.

Thermal inertias over the Fo₅₃ study area are lower than in the other study areas. The escarpment and surrounding Noachian terrains have values of ~200 SI units (0.1 mm maximum particle sizes), but the semi-parallel, arcuate ridges have thermal inertias of ~400 SI units (3 mm maximum particle sizes). Craters that have impacted into the ridged plains suggest that they are relatively coherent with intact interior layers (Figure 11), even though the surface of the unit is in a state of erosion. The olivine-enriched palimpsest craters are at the limit of being too small to use thermal inertia derived by

TES. However, the palimpsest of Figure 10 shows a relatively low thermal inertia (250 SI units, 0.4 mm maximum particle sizes) compared to the rest of the ridged plains suggesting that it may be covered with olivine-enriched eolian sediment.

3.4 Fo_{39} Study Area

Large distinct occurrences of Fo_{39} olivine are uncommon in the fractional contribution maps of *Koeppen and Hamilton* [in press], and all occur in the floors of craters such as the ~70 km diameter unnamed crater centered at 68.6°E, -18.7°S, referred to here as FO39A (Figures 1 and 12). The entire area, including FO39A, is mapped as the dissected Noachian unit Npld [*Greeley and Guest*, 1987], and channels characteristic of the dissected terrains are visible throughout the Fo_{39} study area. However, no channels are visible inside FO39A, and its walls are not visibly incised suggesting that it was formed after the end of the period of dissection.

The mineral fractional contribution maps of *Koeppen and Hamilton* [in press] suggest that the entire Fo_{39} study area is mineralogically uniform if the composition of olivine is not considered. The materials in the western floor of FO39A show only ~10% total olivine abundance, which is only marginally higher than the surrounding Npld plains units (Table 1). However, these materials are distinctive in the Fo_{39} olivine fractional contribution maps of *Koeppen and Hamilton* [in press], whereas the surrounding plains primarily contain the Fo_{68} olivine composition.

The DCS mosaic shows olivine-enriched materials the western floor FO39A corroborating the TES detection of the Fo_{39} composition (white arrow, Figure 12).

Olivine-enriched materials are also observed in a few small (~100 to 200 km²) surface features in the Fo₃₉ study area that appear to be present in channels (black arrows, Figure 12), but there are no coincident high quality TES data to confirm their mineralogy, and they have no clear relationship to the olivine in the crater floor. An enlarged portion of the DCS mosaic shows that eastern rim of the FO39A crater was excavated by three smaller impact events, and ejecta from the largest one (FO39B) now obscures nearly two-thirds of the floor of FO39A (dark grey lines, Figure 13). The bulk of the ejecta from FO39B and the other small craters does not appear enriched in olivine suggesting that the olivine-enriched materials do not occur in abundance in the rim or wall materials of FO39A; however, flow lines in the ejecta emanating from FO39B do intersect the Fo₃₉-enriched materials (small yellow arrows, Figure 13).

The purple/blue unit in the DCS mosaic of the FO39A crater is also notable (black arrow, Figure 13), though TES data show it is not particularly enriched in olivine. The unit displays very low values in daytime TIR images used to make the DCS mosaic implying cold temperatures during the day. This unit is light-toned in visible images and highly fractured (e.g., Figure 14). However, the relationship of the visibly light-toned unit to the Fo₃₉-enriched materials at its contact is difficult to interpret. For example, at the bottom of the visible image in Figure 14 it appears that dark-toned sediments overtop the light-toned unit; however, in the top of the image it appears that they grade into each other or the light-toned unit overtops the olivine-enriched materials. Two pieces of evidence suggest that this visibly light-toned unit is surficial and superposes the Fo₃₉-enriched materials. First, the Fo₃₉-enriched portion of the floor of FO39A is the deepest

location in the crater suggesting it is stratigraphically lower than the visibly light-toned unit. Second, a small crater (<0.5 km in diameter) in the northeastern portion of FO39A (gray arrow, Figure 13) appears to have penetrated the ejecta blanket of FO39B and excavated olivine-enriched materials from the floor of the FO39A crater. If Fo₃₉-enriched materials make up the entire floor of FO39A, it suggests they are not merely an eolian deposit that overtops the visibly light-toned unit.

The floor of the FO39A crater is ~960 m below the surface of the surrounding plains, a depth that is shallow for a crater of its size [e.g., *Melosh*, 1989]. Fo39A also has a very flat floor suggesting that it has been subjected to significant modification and infilling, perhaps at least in part to the Fo₃₉-enriched materials.

Most of the floor of the FO39A crater has thermal inertias of ~350 SI units (~1.8 mm maximum particle size), slightly higher than the surrounding plains. However, the olivine-enriched materials of the crater floor and the light-toned surface unit have thermal inertia values >450 SI units, implying that they are coarse particulates with maximum particle sizes of >0.5 cm, or a mixture of larger cobbles and smaller particulates.

4. Geologic Interpretation and Discussion

Igneous olivine-enriched materials can be thought of as occurring on or near the surface of Mars through three main processes: (1) they may be extruded onto the surface as effusive lava flows, (2) they may be in the form of tephra and ash deposits from explosive volcanic eruptions, and (3) they may be intruded into the shallow subsurface as an igneous pluton, for example a dike or sill. Although these are relatively disparate

emplacement scenarios, distinguishing between them can be difficult given the Noachian and Hesperian age of the surfaces in Terra Tyrrhena. The length of time that has elapsed from the emplacement of some olivine-enriched materials during the Noachian to today has allowed materials emplaced on the surface to be buried, and materials emplaced in the subsurface to be exposed. Olivine-enriched materials have been excavated and redistributed by craters and incorporated into ejecta deposits and melt sheets, and they may have been eroded and remobilized, perhaps multiple times. The end result is that many surface features such as flow lobes or surface textures that could be used to discern the origin of the olivine-enriched materials have been destroyed. Nonetheless, in this section, we investigate possible emplacement scenarios for olivine-enriched materials within the four sites we studied in detail and in Terra Tyrrhena as a whole.

4.1 Fo₉₁ Study Area

The Fo₉₁-enriched materials of Terra Tyrrhena appear confined to a single layer or stack of layers that was once more extensive than it is today. The thickness of this layer is relatively unconstrained depending on whether the olivine-enriched layers were laid onto irregular topography (a thickness as small as tens of meters is possible) or were relatively horizontal (suggesting a thickness of ~200 to 900 m). However, a rough minimum estimate of the surface area of the Fo₉₁-enriched materials surface area can be derived if we assume that the rims of the Fo₉₁-bearing FO91A, FO91B, and FO91C craters and the low knobs and hills of the Fo₉₁ study area were once part of a continuous

layer. If these exposures were once connected, they represent the remnants of FO₉₁-enriched materials that once covered at least 20,000 km².

The FO₉₁-enriched materials appear to be relatively thin or occur at the base of a once thicker unit, and they exhibit characteristics indicative of a series of lava flows. Olivine-enriched materials are not observed in the units stratigraphically below the base of the crater rims of FO91B and FO91C or the low knobs and hills suggesting they are currently relatively thin. If the olivine-enriched unit was thick and merely buried in some places, channel systems observed on both the Noachian and Hesperian terrains might be expected to expose and transport olivine-enriched materials from deeper in the unit, but they do not. Since there is no upper bound on the olivine-enriched materials in this area, it is not known if these materials were emplaced as a thin layer, or if they occur at the base of a once thicker stack of materials. A thin sheet of olivine-enriched materials like those observed could have been emplaced by a series of volcanic events, or remobilized and laid onto the surface as a thin sheet of olivine-enriched crater ejecta. However, the olivine-enriched materials appear to have distinct layering (e.g., Figure 4), and coherent, planar boundaries between separate volcanic events, either effusive or armored explosive deposits, are the most likely explanation.

In terms of age, the FO₉₁-enriched FO91B and FO91C craters sit on Noachian aged terrain, and, like the rim of the FO91A crater, appear old and degraded. The FO₉₁-enriched low knobs and hills are also interpreted as Noachian in age based on their embayment by the Hesperian Hpl₃ unit. The relatively thin, FO₉₁-enriched Noachian units must have already been in place and substantially eroded (to create erosional morphology

of the knobs) before lava flows of the Hpl₃ unit flooded the FO91A crater, breached its northern rim, and covered the rest of the Fo₉₁ study area. Today, the Fo₉₁-enriched materials in the knobs and rims of these Noachian craters are in a state of exposure and eolian erosion, traveling down slope as talus and being strewn across the plains as sediment.

4.2 Fo₆₈ Study Area

The morphology of Fo₆₈-enriched materials in the Saheki and FO68A Craters does not provide many clues to its igneous origin. It appears that Fo₆₈-enriched materials were present in the Noachian subsurface as a relatively thick (~2500 m) package of materials. These materials were exposed by the Saheki and FO68A impact events, and appear to make up most the floor of Saheki Crater. The walls of the two craters were incised by channels that formed large sedimentary fans, presumably by fluvial processes [Moore and Howard, 2005], which are composed of Fo₆₈-enriched materials from the craters' rims and the subsurface of nearby terrains. The surface area and pervasiveness of olivine-enriched materials throughout the fans of Saheki and FO68A suggest that the ~2500 m package of materials may be relatively uniform, and relatively olivine-enriched. A layer this thick implies that the Fo₆₈-enriched materials in the subsurface near Saheki and FO68A may have been part of an igneous intrusion or stacks of many overlapping, and relatively homogenous, olivine-enriched surface flows.

Crater distributions based on fan deposits in the southern highlands (including those of Saheki and FO68A) led Moore and Howard [2005] to estimate that the

sedimentary fans were formed at the boundary of the Noachian and Hesperian (3.3 to 3.7 Ga). From scaling relationships based on alluvial fans in the White Mountains of California, they surmise that the Martian sedimentary fans needed a minimum of 1000 years to form and may reasonably have taken ~100,000 years. This time frame may have been even longer if the precipitation and runoff necessary to drive sediment transport into the fan were intermittent [*Moore and Howard, 2005*].

The presence of olivine in the fans can be used to place independent constraints on the evolution of the fans and the duration of aqueous activity at the end of the Noachian. Using data from laboratory analyses, *Stopar et al.* [2006] calculated minimum residence times for olivine on Mars for a variety of conditions including the particle size and composition of olivine grains, and the pH and temperature of the dissolving solution. They found that 1 mm grains of FO₆₅ olivine completely dissolve in 42,000 years in neutral solutions (pH 7) at 5° C. Smaller grain sizes, more iron-rich compositions, non-neutral solutions both acidic and basic, and higher temperatures all serve to increase the rate of dissolution and decrease the residence time of olivine on Mars. Mineral dissolution rates measured in the field can be 2 to 4 orders of magnitude slower than rates measured in experimental studies because of the lack of mineral surface area, the formation of surface coatings, low fluid/mineral ratios, and solutions that become saturated and approach equilibrium around the mineral grains [e.g., *White and Brantley, 2003*]. However, the olivine-enriched materials of the sedimentary fans in Saheki Crater and FO68A are almost certainly granular (thermal inertias suggest maximum particle sizes of 2.4 mm, and ~90% of the grains are likely smaller) and were probably deposited

by liquid that likely did not have time to chemically saturate during each aqueous event. Granular particles interacting with flowing, unsaturated water represent conditions like those used to calculate dissolution rates in laboratory studies, and 42,000 years may be an appropriate estimate of the minimum residence time of olivine in these fans.

The survival of olivine-enriched materials throughout the sedimentary fans suggests that the fans may have been built relatively quickly, burying olivine-enriched materials before dissolution could take place. However, this process alone would not preserve the olivine-enriched eastern floor of Saheki Crater that appears to predate the sedimentary fans. This part of the crater floor may have been hydrologically isolated and did not interact with water building the fans, or it may have been able to better withstand interaction with water because of larger particle sizes (0.5 cm maximum particle sizes are implied by its thermal inertia). If both the floor of Saheki Crater and the sedimentary fans were part of the same hydrologic system and had similar interactions with water, it suggests that the total duration of aqueous activity, including the activity that built the fans, lasted only tens of thousands of years at the end of the Noachian. Furthermore, water must have been relatively sparse after the end of the fan-building episode in order to preserve olivine in its particulate form, which is most prone to weathering, since its deposition in the fan. This interpretation agrees the findings of *Irwin et al.* [2005] and *Howard et al.* [2005], who suggest that aqueous activity ceased relatively abruptly after the fans' formation based on lack of fan-head trenching and restriction of deposition near the apex of the fans.

4.3 Fo₅₃ Study Area

The ridged plains of the Fo₅₃ study area are the only locations we studied in detail at which olivine-enriched volcanic surface flows appear unambiguous. The parallel, arcuate ridges on the features are characteristic of Hesperian ridged plains (Hr), and we observed layering and embayment relationships consistent with the interpretation of the ridged plains as a layered stack of Hesperian-aged sheet flows. There is no obvious volcanic edifice that serves as the source of the Fo₅₃-enriched volcanic plains, but that is not uncommon in ancient Martian volcanic terrains and the ridged plains in particular. The palimpsest craters of the Fo₅₃ study area appear to have been filled by same ridged plains-forming lavas (Hr), and palimpsests outside of the ridged plains suggest that these surface flows were once more extensive.

The ridged plains units of the Fo₅₃ study area are currently being eroded to expose the underlying Noachian plains. It appears that *in situ* olivine-enriched materials are localized around the arcuate ridges of the plains, and they may be the source of the low thermal inertia olivine-enriched materials, probably sediments, residing in the topographic lows of the ridged plains and palimpsest craters. There is no evidence of fluvial transport in the Fo₅₃ study area and eolian transport of olivine-bearing grains is the most likely agent. Olivine-enriched materials are uncommon outside of the ridged plains units suggesting that if they are being transported off the ridged plains, they are being dispersed in relatively short order.

It seems likely that the ridged plains may have once completely covered the escarpment in the Fo₅₃ study area, as tendrils of the ridged plains irregular border come

close to the escarpment's ridgeline in some areas (Figure 9). If volcanic materials of the ridged plains came from the north, inflated to overtop the escarpment (creating the embayment relationship in the northern ridged plains as they paused), and then deflated, they would have left the high-topography lavas on the escarpment as the first to erode. This possible scenario could also explain the mineralogic similarity between the Fo₅₃-ridged plains and the escarpment; the only mineralogical difference between the two units being the abundance of olivine, which would have been the first mineral to erode from the materials topping the escarpment.

4.4 Fo₃₉ Study Area

The occurrence of Fo₃₉-enriched materials in the floor of the FO39A crater is demonstrative of how spectral (and therefore mineralogical) information can be used to find interesting materials in rather nondescript terrains on Mars. The FO39A crater sits in the middle of the Noachian dissected unit, Npld, the most common unit mapped in the southern highlands. However, in a small location in the western portion of its floor sits some of the most iron-rich olivine observed on Mars.

The Fo₃₉-enriched materials are only visible in one portion of the crater floor, and they appear to be covered by both a light-toned surface unit and ejecta from the FO39B crater. However, their location in the deepest part of FO39A, and a small crater that has excavated olivine-enriched materials from beneath the FO39B ejecta, suggest that Fo₃₉-enriched materials cover the entire floor of FO39A. The flat and shallow topography of FO39A suggests significant infill from crater collapse or volcanic materials, but crater

collapse can be ruled out because olivine on the floor of FO39A is compositionally different from the materials in its walls. Olivine-enriched materials do not occur in other topographic lows near the FO39A crater and lava flows do not appear to have breached the crater walls of FO39A. This suggests that olivine-enriched lavas may have erupted directly into the crater, perhaps aided to the surface by fracturing of the subsurface by the impact.

The presence of olivine-enriched materials in the Npld unit of the FO₃₉ study area suggests that the crater and ensuing eruption took place after the end of precipitation that caused the channel systems dissecting the Npld unit. This is supported by the observation that channels are not found within the crater, nor do they incise the rim of FO39A, such as occurred in the FO₆₈ study area. If the crater and its volcanic products were formed during the era of dissection during the Noachian, perhaps the crater was buried, protected from modification, and exhumed only recently; however, there is little evidence of this today.

4.5 Olivine in Terra Tyrrhena

In terms of composition, the FO₉₁-enriched materials that we studied are unique in Terra Tyrrhena; no other materials in the region contain such Mg-rich olivine. Their location is relatively close to the Hellas rim materials, but *Koeppe and Hamilton* [in press] pointed out that the 25% olivine abundance in these rocks is probably too low to be simply mantle materials excavated by the Hellas impact event. Our observations suggest instead that they may be volcanic materials that tapped magma chambers with a high

Mg/Fe ratio during the Noachian era. If the volcanic materials and Hellas Basin are linked, perhaps the Hellas impact event fractured the subsurface in southern Terra Tyrrhena enough that eruptions could draw from relatively undifferentiated magma near the mantle. If this magma was present in discrete magma chambers, or at least not homogeneously distributed beneath the Hellas basin, it could help to explain the lack of widespread occurrences of the Mg-rich olivine throughout Terra Tyrrhena near the Hellas basin rim.

The Fo₆₈ composition is the most common olivine composition identified in the olivine-enriched materials of Terra Tyrrhena. Fo₆₈-enriched materials occur in crater floors, crater ejecta, Hesperian ridged plains units, and in smaller occurrences than we included in this study throughout Noachian terrains of the region. Like the rest of the southern highlands, the Fo₆₈ composition appears to be the main rock-forming olivine of Terra Tyrrhena throughout its history.

The Fo₅₃-enriched materials of the ridged plains are also relatively common. However, while the units we studied have the distinctive signature of Fo₅₃, other examples of Hesperian ridged plains units in Terra Tyrrhena (e.g., the area directly to the east of the Fo₅₃ study area in Figure 1) exhibit the Fo₆₈ composition. To the north of Terra Tyrrhena near the Isidis Basin, Fo₅₃ is even more common, and Terra Tyrrhena may be on the margin of what was a large episode of Fo₅₃-enriched volcanism during the Hesperian. The timings of the Fo₆₈-enriched and Fo₅₃-enriched ridged plains, if they are indeed separate volcanic episodes, appear to be coeval.

Materials with >20% olivine of the Fo₃₉ composition do not exist in Terra Tyrrhena; however, a few craters, including the Fo₃₉ study area, that we surveyed show Fo₃₉ abundances up to ~10%. The locations of these craters do not appear to be correlated with geography, topography, or previously mapped geology. However, their morphology suggests that many of the craters containing this composition have formed after the fluvial dissection of the Noachian. For example, the FO39A crater does not show incised rims even though it occurs in the dissected Npld terrain. If these Fo₃₉-bearing craters and their associated Fo₃₉-bearing materials are Hesperian in age, it implies a relatively late episode of Fe-rich olivine in Terra Tyrrhena consistent with an evolving magma source that persisted beneath the region.

Regardless of composition, the ubiquity of olivine in Terra Tyrrhena is curious because so many of the terrains in this region contain geomorphic signs of liquid water. The presence of olivine has been used to argue for a water-poor history for Mars [Christensen *et al.*, 2003; Hoefen *et al.*, 2003], and yet in Terra Tyrrhena we observe olivine at 5 to 10% abundances throughout the Noachian terrains dissected by fluvial channel systems, some of which are rather well-developed [e.g., Malin and Edgett, 2003]. This study provides three insights into the history of olivine and water in Terra Tyrrhena.

The first insight is that olivine appears to be more common in the subsurface of Terra Tyrrhena than on its surface. Fifteen of the twenty-five olivine-enriched sites we surveyed are associated with craters or crater ejecta that have no obvious source of volcanic input. All of the craters we examined have excavated into the Martian crust and exposed materials that were previously protected from the processes acting on the surface

of Mars during the Noachian. These craters are morphologically similar to FO39A, and they look relatively “middle-aged”; none of the craters look fresh, but they do not have incised rims and their walls are more intact than the oldest craters of the Noachian dissected terrains. This would imply that the olivine-enriched materials in these craters were excavated and exposed only after the end of Noachian dissection. Even if subsurface olivine-enriched materials did interact with Noachian ground water systems, olivine grains sequestered in the Martian subsurface during the Noachian probably had a higher survival potential than olivine at the surface. *Stopar et al.* [2006] suggest that olivine in basaltic rock has a residence time at least 33 times longer than particulate olivine grains, and if the ground water reaches chemical equilibrium while percolating through the rock, residence times may be up to four orders of magnitude longer. This suggests that the olivine-enriched mineralogy of materials excavated from the Noachian subsurface of Terra Tyrrhena may be more representative of its original bulk mineralogy than its Noachian surface, which was subjected to aqueous activity.

The second insight is that most olivine-enriched materials that are *in situ* in Terra Tyrrhena today appear to have been emplaced after the end of Noachian dissection. Nine of the twenty-five sites we surveyed are associated with Hesperian ridged plains materials like those of the FO₅₃ study area, or craters that have been filled with relatively young-looking volcanic materials that display morphology similar to the ridged plains units. These *in situ* materials are emplaced on top of Noachian terrains, and none show evidence of fluvial activity. It is apparent that these materials did not interact with the water that carved the Noachian-aged channels present in Terra Tyrrhena.

The Fo_{68} study area, with its olivine-enriched alluvial fans, provides the third insight. The olivine-enriched materials at this location were in the subsurface and exposed before the abatement of fluvial activity during the Noachian. They may have been exposed toward the end of this period, but judging from the size and morphology of the fans, aqueous activity had far from ceased. At least in this location, evidence suggests that olivine-enriched materials have interacted with liquid water and survive today.

5. Conclusions

In this study we identified twenty-five examples of olivine-bearing materials on Mars in Terra Tyrrhena and we analyzed four in detail using data from the TES, THEMIS, MOC, and MOLA instruments. Of the sites we studied we determined the following:

(1) The Fo_{91} composition of olivine is rare in Terra Tyrrhena and makes up a relatively thin but areally extensive layer, probably composed of one or more volcanic flows erupted during the early Noachian. These volcanic events tapped a relatively undifferentiated magma chamber that may have been accessed using fractures created by the Hellas impact event.

(2) Olivine with the Fo_{68} composition is omnipresent in Terra Tyrrhena at abundances of 5 to 10%, and materials containing abundances of olivine >20% are common. We analyzed two craters that exposed a relatively thick (>2000 m) and homogenous layer of Fo_{68} -enriched materials that now make up a number of large alluvial fans inside the craters. Dissolution times for olivine indicate that the total

duration of aqueous fan-building activity must have lasted less than tens of thousands of years.

(3) The FO_{53} and FO_{68} compositions commonly occur in the previously mapped Hesperian ridged plains unit, Hr. The FO_{53} -enriched materials of the ridged plains unit may represent an extension of volcanic materials more common to the southern highlands north of Terra Tyrrhena.

(4) FO_{39} -enriched materials are rare in Terra Tyrrhena and occur mostly in the floors of craters. Although few clues are available, it appears that Fe-rich volcanic materials erupted into a few craters that were formed after the end of aqueous activity during the Noachian.

The geologic setting and inferred timing of the locations we studied in Terra Tyrrhena suggest that olivine-enriched materials may have been more common on the surface of Mars before aqueous activity during the Noachian. Noachian-aged olivine in Terra Tyrrhena exists on the surface of Mars today either because it was protected from aqueous processes in the subsurface and was not exhumed until after or near the end of the Noachian, or the total duration of aqueous activity in Terra Tyrrhena was relatively short. Olivine-enriched materials associated with the Hesperian ridged plains units appear to have been emplaced after the end of aqueous activity on Mars, and do not appear to have interacted with liquid water.

Acknowledgements

The authors would like to profusely thank Christopher Edwards, Noel Gorelick, and Keith Nowicki for developing and providing the mosaicking software used in this work.

Tables

Table 1. Percent abundances of mineral groups retrieved from linear least squared modeling of TES spectra in the terrains of each study area.

| Unit | Olivine | Feldspar | High-Ca Pyroxene | Low-Ca Pyroxene | Sulfate | Silica + Phyllo. |
|-----------------------------|---------|----------|---------------------|--------------------|---------|---------------------|
| Fo₉₁ site | | | | | | |
| Rugged Terrain | 5 | 34 | 7 | 24 | 15 | 11 |
| Smooth Plains | 11 | 25 | 10 | 22 | 13 | 11 |
| Fo ₉₁ -enriched | 26 | 21 | 9 | 14 | 12 | 9 |
| Fo₆₈ site | | | | | | |
| Crater Ejecta | 6 | 34 | 5 | 23 | 14 | 13 |
| Fo ₆₈ -enriched | 22 | 20 | 8 | 17 | 17 | 10 |
| Fo₅₃ site | | | | | | |
| Escarpment | 9 | 25 | 10 | 20 | 13 | 15 |
| Fo ₅₃ -enriched | 20 | 21 | 7 | 18 | 14 | 12 |
| Fo₃₉ site | | | | | | |
| Intercrater Plains | 8 | 28 | 11 | 21 | 13 | 14 |
| Fo ₃₉ -enriched | 11 | 29 | 10 | 21 | 13 | 11 |

Values are listed in this table as output from the linear least squares model to avoid rounding errors. However, please note that differences in mineral abundances less than ~5% are difficult to reliably distinguish.

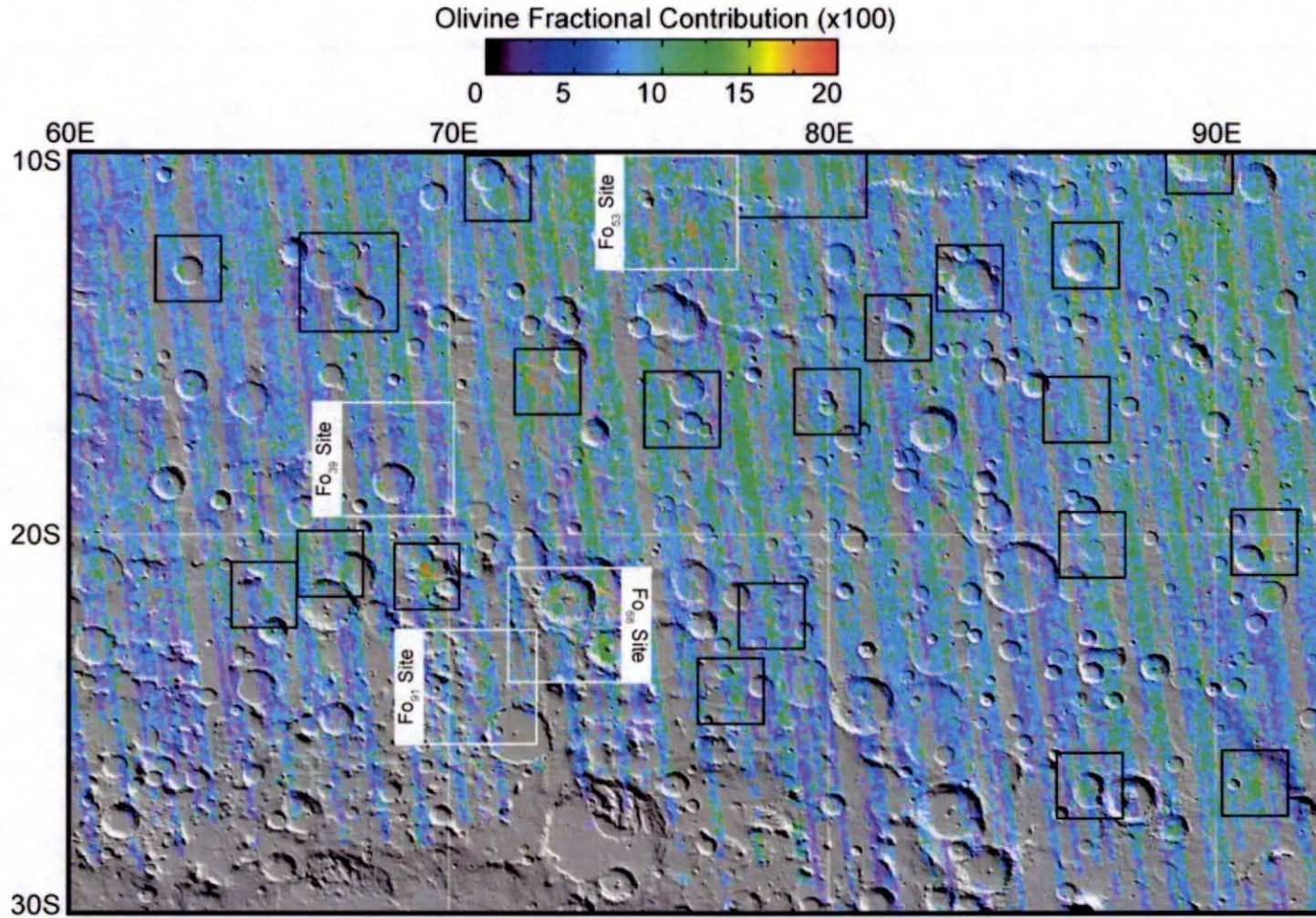


Figure 1. Shaded relief map of Terra Tyrrhena region overlain by the map of total olivine fractional contribution. Black boxes denote occurrences of olivine-enriched materials that we surveyed, and white boxes denote the four olivine-enriched sites examined in this study.

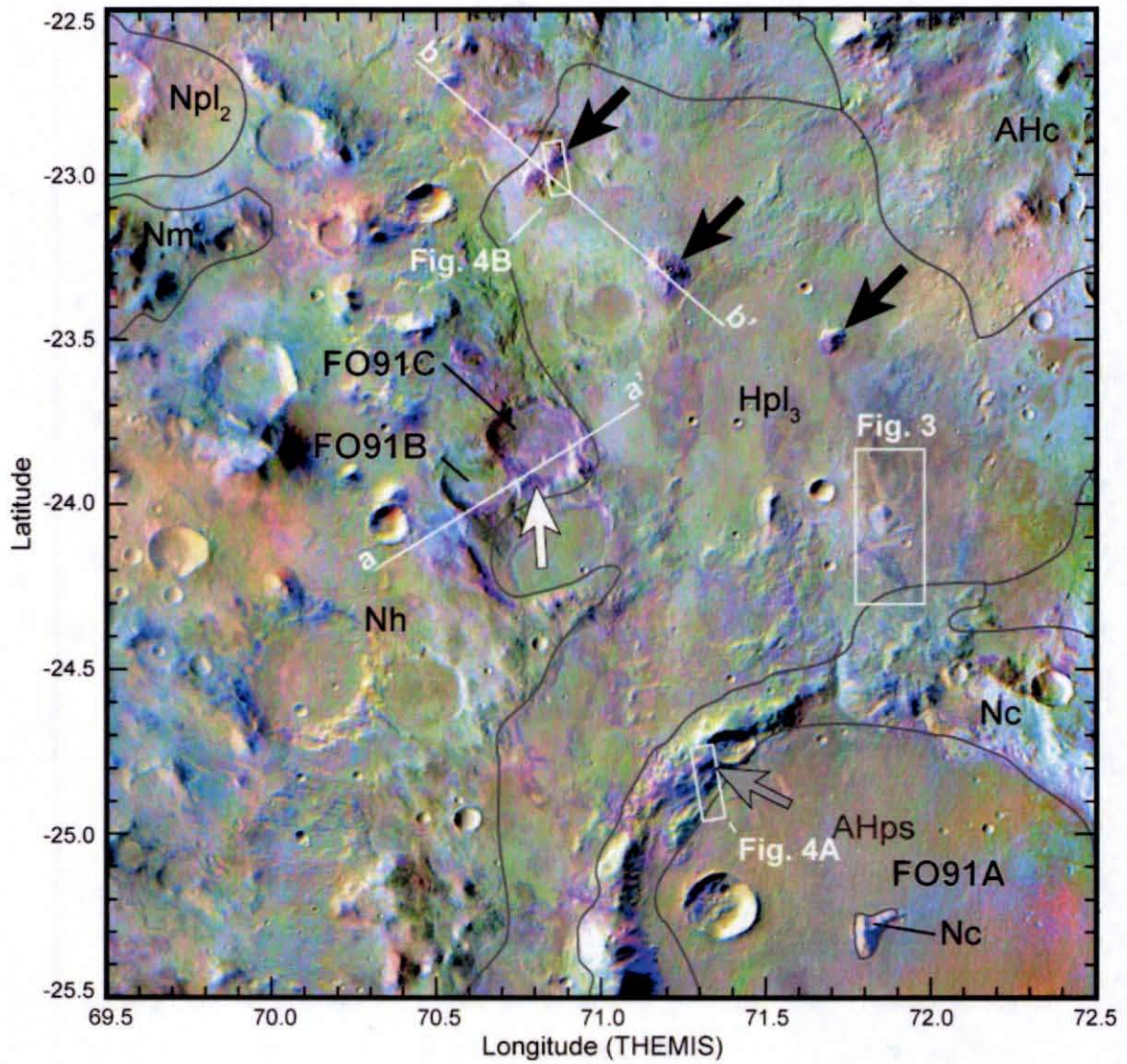


Figure 2. DCS mosaic of the FO₉₁ study area. Arrows point to the locations of olivine-enriched materials discussed in the text. White lines marked with a-a' and b-b' indicate the location of topographic profiles shown in Figure 5. Black labels indicate crater identifiers used in the text. Dark grey lines indicate approximate geologic boundaries modified from Leonard and Tanaka [2001].



Figure 3. Portion of THEMIS VIS image V23400004 showing that material flowed northward from the direction of FO91A and wrapped around a small pre-existing knob. The image is 14 km across.

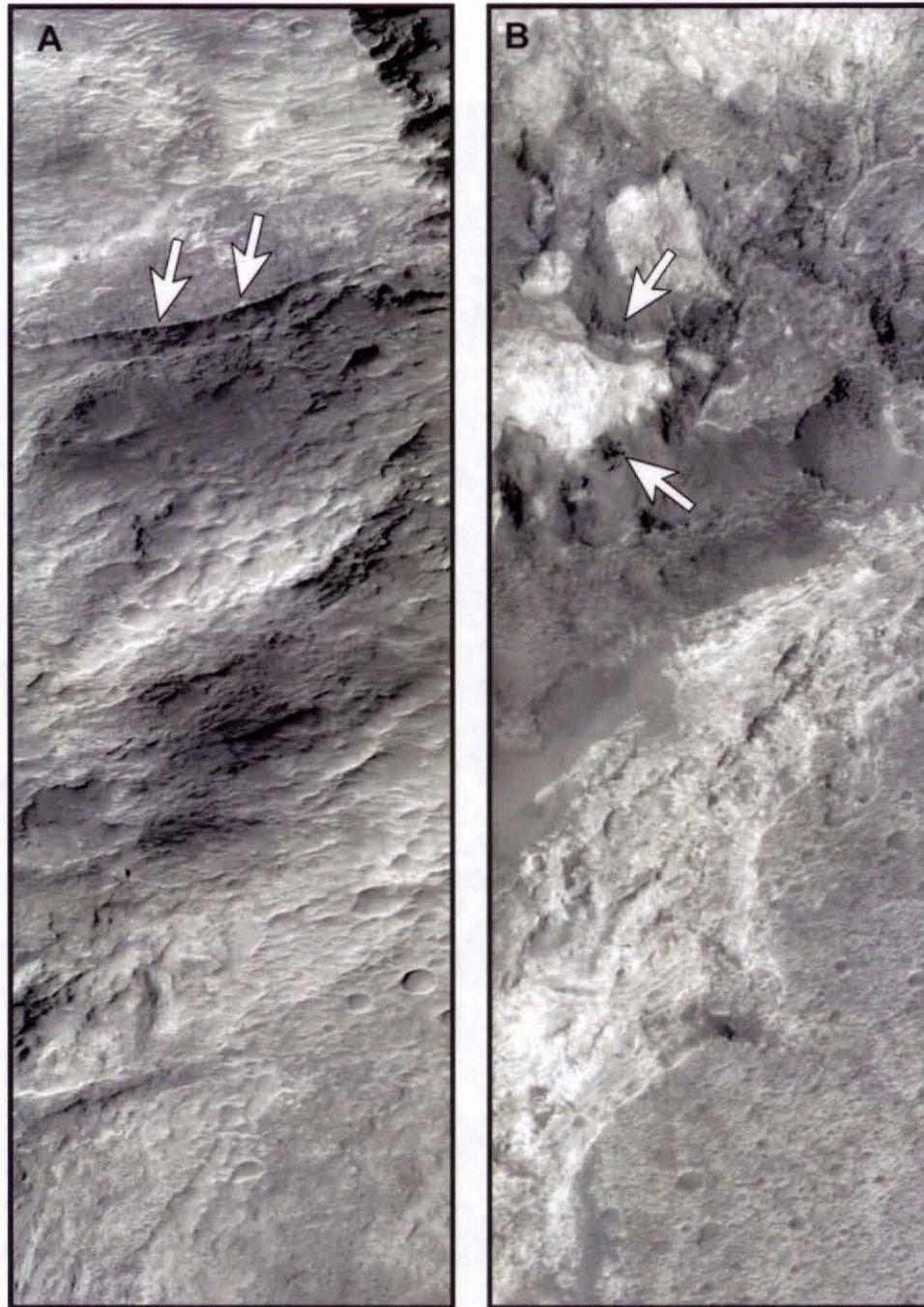


Figure 4. A) MOC NA image S1403191 showing the dark-toned materials associated with olivine-enrichment in the rim of FO91A. White arrows indicate a resistant ridge that appears to be the source of some of the materials. B) MOC NA image M0902017 showing olivine-enriched materials eroding out of the knob at 70.9°E, 23.0°S and moving down slope as talus. Both images are ~3 km across.

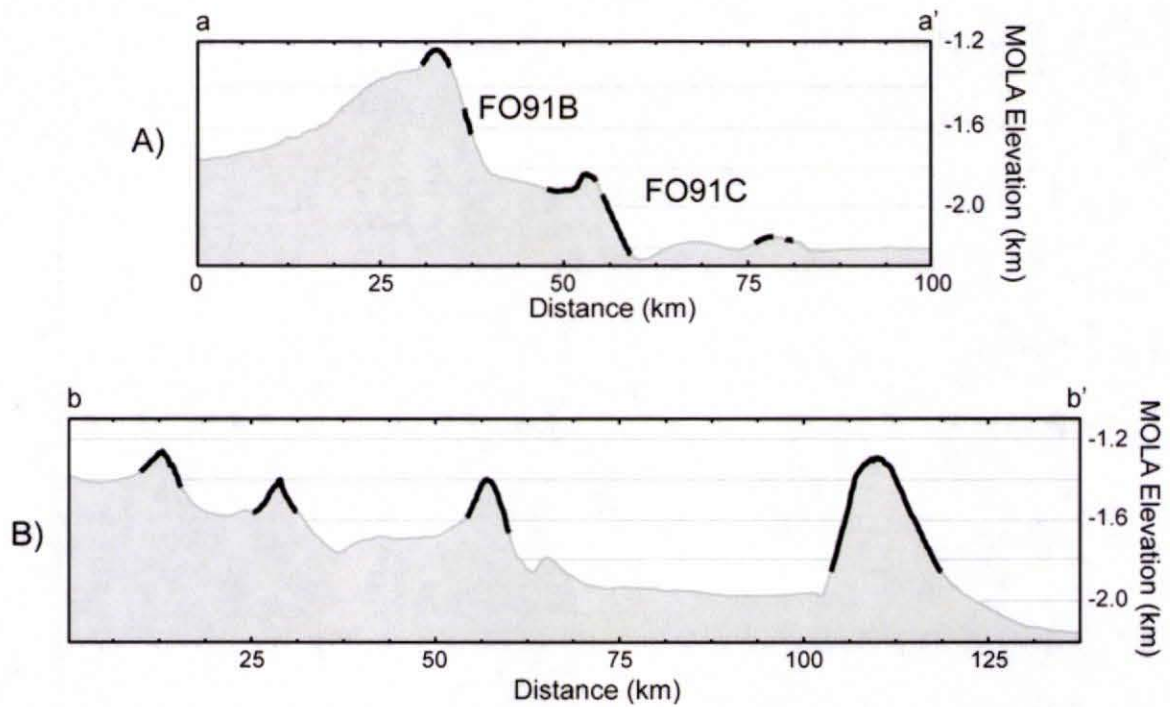


Figure 5. A) Topographic profile a-a' over the olivine-enriched crater rims of the FO91B and FO91C craters, and B) topographic profile b-b' over four olivine-enriched knobs. Thick black lines indicate where olivine-enriched materials are observed along the profile.

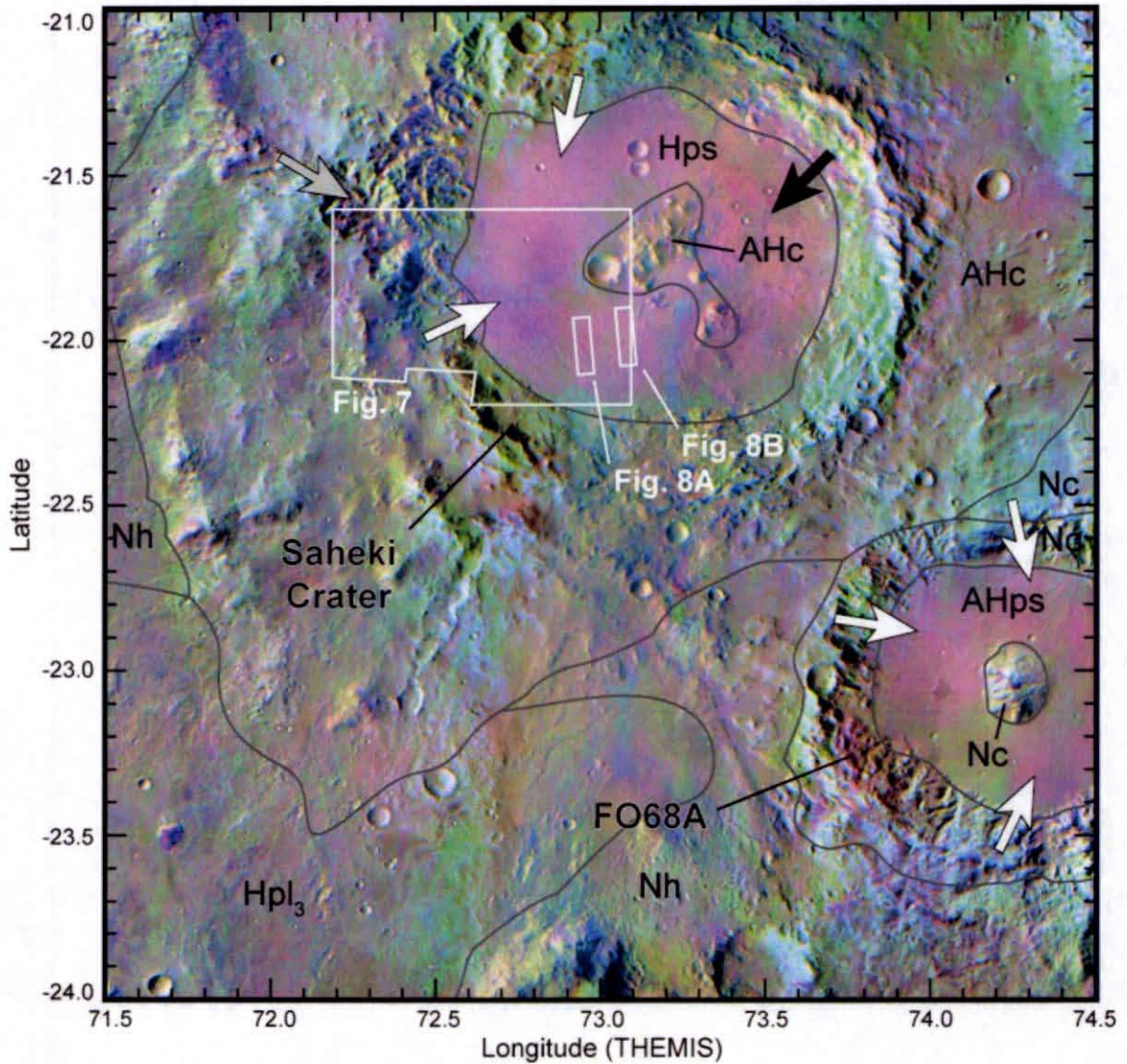


Figure 6. DCS mosaic of the FO₆₈ study area. Arrows point to the locations of olivine-enriched materials discussed in the text including olivine-enriched sedimentary fans (white arrows) and the floor of Saheki Crater (black arrow). Dark grey lines indicate approximate geologic boundaries modified from Leonard and Tanaka [2001].

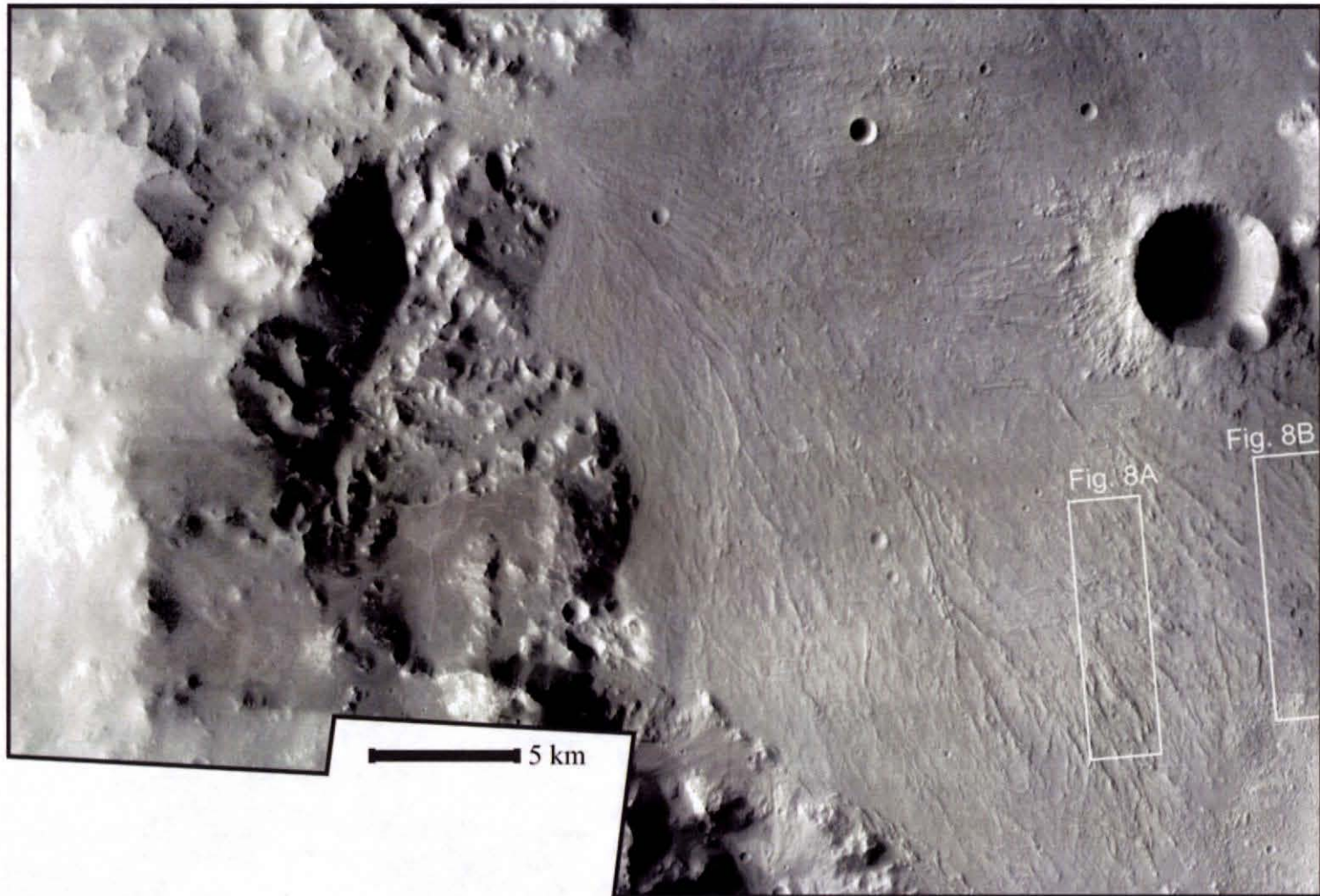


Figure 7. Mosaic of THEMIS VIS images: V10808002, V11120001, V14502001, V15101003, and V17260001 showing the morphology of a sedimentary fan in Saheki Crater. Branching channels and topographic inversion is apparent throughout the fan.



Figure 8. A) MOC NA image R1501806 showing the relief inversion of channels on the sedimentary fan in Saheki Crater, and B) MOC NA image R1402685 showing the distal end of the sedimentary fan; white arrows demarcate where fan deposits contact the pre-fan crater floor.

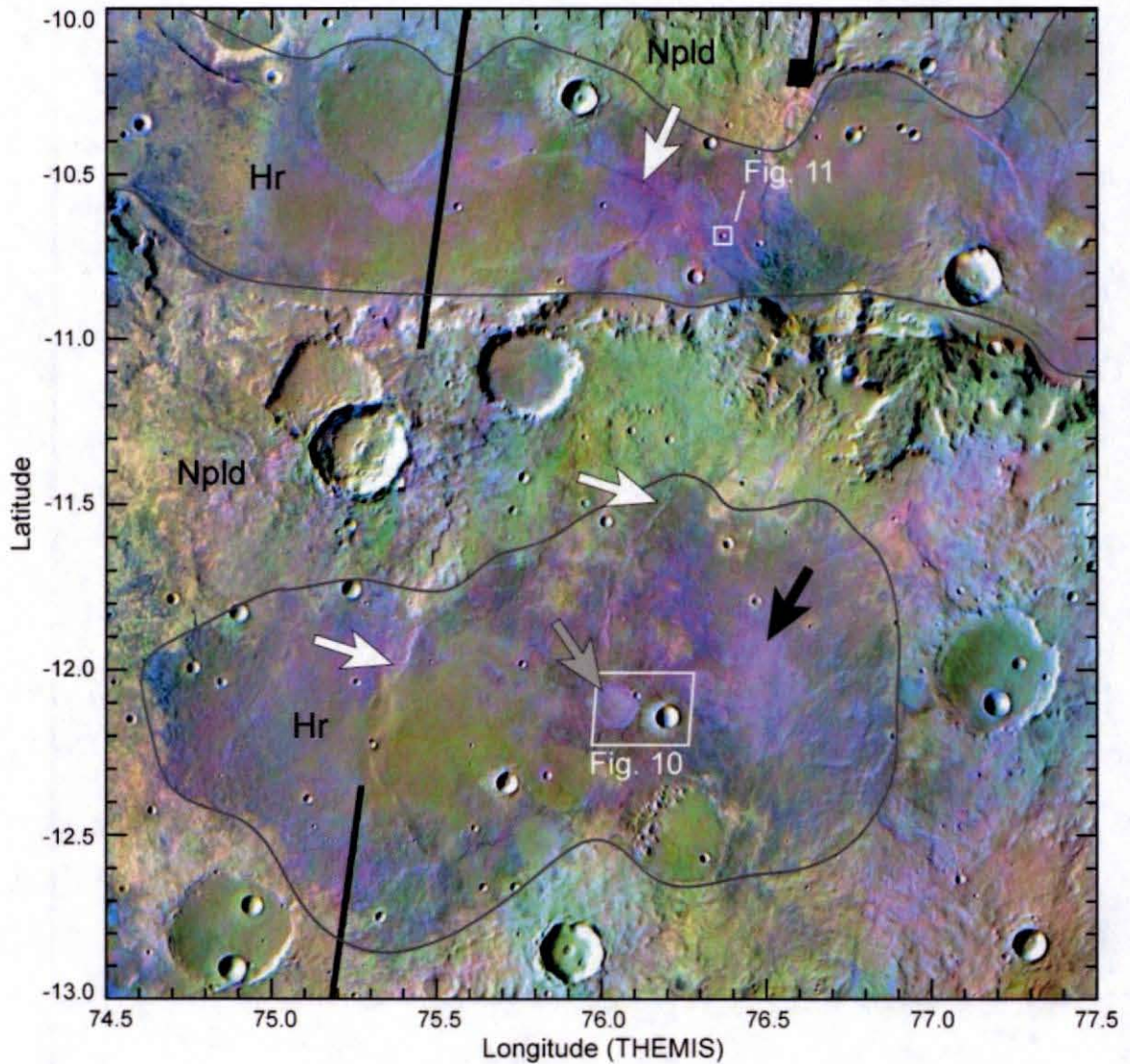


Figure 9. DCS mosaic of the FO₅₃ study area. Arrows point to surface features discussed in the text including arcuate, parallel ridges (white arrows), olivine-enriched low thermal inertia units (black arrow), and an olivine-enriched palimpsest crater (gray arrow). Black areas are regions that did not contain THEMIS daytime TIR data. Dark grey lines indicate approximate geologic boundaries modified from Greeley and Guest [1987].

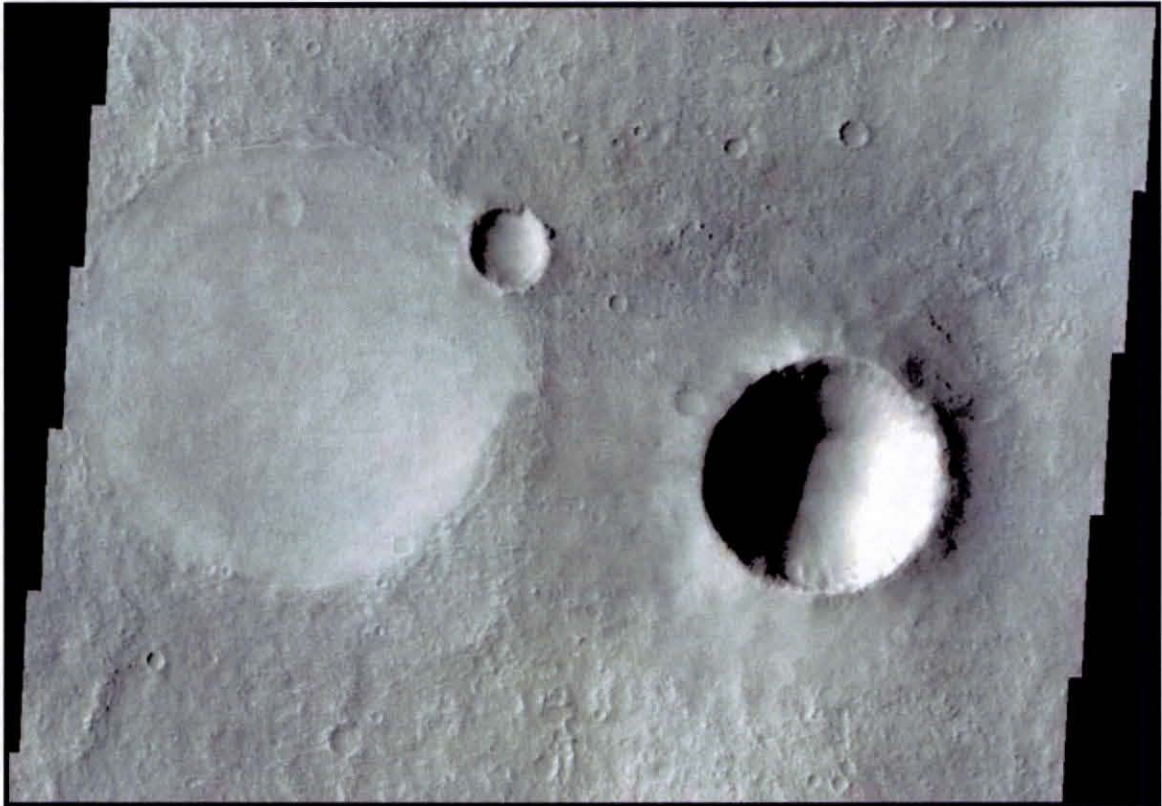


Figure 10. THEMIS VIS image V26682005 showing a palimpsest crater that is almost completely filled in contrasted with a relatively fresh crater.



Figure 11. Figure 7. MOC NA image S1100943 showing a A) relatively fresh crater in the northern ridged plains, and B) enlargement of the crater wall. Arrows indicate coherent layers outcropping throughout the crater walls.

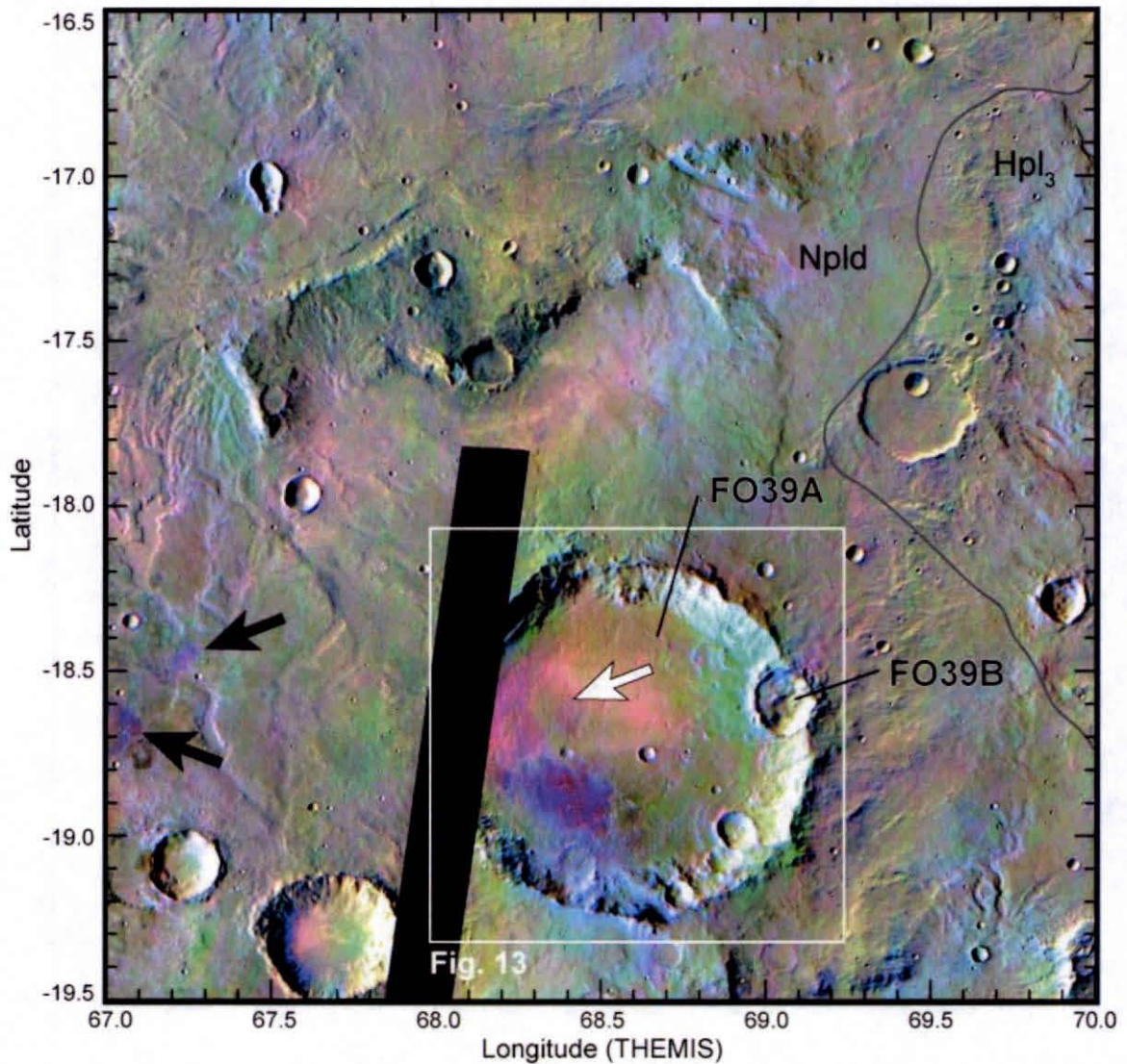


Figure 12. DCS mosaic of the FO₃₉ study area. The western portion of the crater floor is the only area that contains olivine-enriched material. Black areas are regions that did not contain THEMIS daytime TIR data. White box indicates the portion of the DCS mosaic enlarged in Figure 13. Dark grey lines indicate approximate geologic boundaries modified from Greeley and Guest [1987].

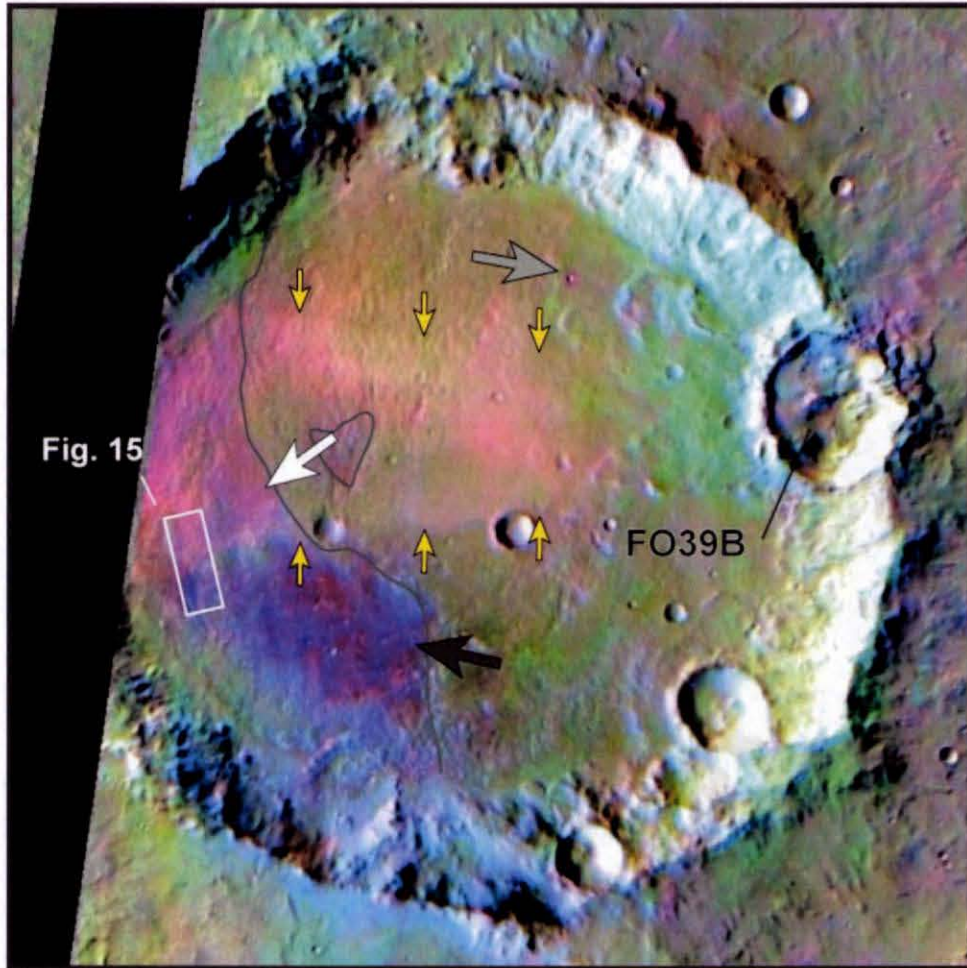


Figure 13. Enlargement of the DCS mosaic showing the FO_{39} -enriched crater floor. White and gray arrows point to FO_{39} -enriched materials. Black arrow points to light-toned outcrop (that appears dark in daytime TIR data), and small yellow arrows demarcate flow lines from the ejecta of FO39B. Dark grey lines indicate the end of the continuous ejecta blanket of FO39B.



Figure 14. MOC NA image M1500407 showing the contact between the light-toned, olivine poor materials and the dark-toned olivine-enriched crater floor. The surface is highly fractured, and superposition between the materials is not clear.

REFERENCES

- Abshire, J. B., X. Sun, and R. S. Afzal (2000), Mars Orbiter Laser Altimeter: Receiver model and performance analysis, *Applied Optics*, *39*, 2440-2460.
- Armstrong, J. C., and C. B. Leovy (2005), Long term wind erosion on Mars, *Icarus*, *176*, 57-74.
- Aronson, J. R., A. G. Emslie, and H. G. McLinden (1966), Infrared spectra from particulate surfaces, *Science*, *152*, 345-346.
- Bandfield, J. L. (2002), Global mineral distributions on Mars, *Journal of Geophysical Research*, *107*, 5042, doi:5010.1029/2001JE001510.
- Bandfield, J. L., P. R. Christensen, and M. D. Smith (2000a), Spectral data set factor analysis and end-member recovery: Application to analysis of Martian atmospheric particulates, *Journal of Geophysical Research*, *105*, 9573-9587.
- Bandfield, J. L., T. D. Glotch, and P. R. Christensen (2003), Spectroscopic identification of carbonate minerals in the Martian dust, *Science*, *301*, 1084-1087.
- Bandfield, J. L., V. E. Hamilton, and P. R. Christensen (2000b), A global view of Martian surface compositions from MGS-TES, *Science*, *287*, 1626-1630.
- Bandfield, J. L., V. E. Hamilton, P. R. Christensen, and H. Y. McSween, Jr. (2004a), Identification of quartzofeldspathic materials on Mars, *Journal of Geophysical Research*, *109*, doi:10.1029/2004JE002290.
- Bandfield, J. L., D. Rogers, M. D. Smith, and P. R. Christensen (2004b), Atmospheric correction and surface spectral unit mapping using Thermal Emission Imaging System data, *Journal of Geophysical Research*, *109*, doi:10.1029/2004JE002289.
- Bertka, C. M., and Y. Fei (1998a), Density profile of an SNC model Martian interior and the moment-of-inertia factor of Mars, *Earth Planet. Sci. Lett.*, *157*, 79-88.
- Bertka, C. M., and Y. Fei (1998b), Implications of Mars Pathfinder data for the accretion history of the terrestrial planets, *Science*, *281*, 1838-1840.
- Bibring, J.-P., Y. Langevin, A. Gendrin, B. Gondet, F. Poulet, M. Berthé, A. Soufflot, R. Arvidson, N. Mangold, J. F. Mustard, P. Drossart, and t. O. team (2005), Mars surface diversity as revealed by the OMEGA/Mars Express observations, *Science*, *307*, 1576-1581.
- Bibring, J.-P., Y. Langevin, J. F. Mustard, F. Poulet, R. E. Arvidson, A. Gendrin, B. Gondet, N. Mangold, P. Pinet, F. Forget, and t. O. team (2006), Global

mineralogical and aqueous Mars history derived from OMEGA/Mars Express data, *Science*, 312, 400-404, doi: 410.1126/science.1122659.

- Binzel, R. P., M. J. Gaffey, P. C. Thomas, B. H. Zellner, A. D. Storrs, and E. N. Wells (1997), Geologic mapping of Vesta from 1994 Hubble Space Telescope images, *Icarus*, 128, 95-103, IS975734.
- Bishop, J. C., and C. M. Pieters (1995), Low-temperature and low atmospheric pressure infrared reflectance spectroscopy of Mars soil analogue materials, *Journal of Geophysical Research*, 100, 5369-5379.
- Bishop, J. C., C. M. Pieters, and T. G. Burns (1993), Reflectance and Mossbauer spectroscopy of ferrihydrite-montmorillonite assemblages as Mars soil analogue materials, *Geochimica et Cosmochimica Acta*, 57, 4583-4595.
- Borg, L. E., and D. S. Draper (2003), A petrogenetic model for the origin and compositional variation of the martian basaltic meteorites, *Meteorit. Planet. Sci.*, 38, 1713-1731.
- Brearley, A. J., and R. H. Jones (1998), Chondritic meteorites, in *Planetary Materials*, edited by J. Papike, Mineralogical Society of America, Washington D. C.
- Burns, R. G., and F. E. Huggins (1972), Cation determinative curves for Mg-Fe-Mn olivines from vibrational spectra, *American Mineralogist*, 57, 967-985.
- Christensen, P. R., D. L. Anderson, S. C. Chase, R. N. Clark, H. H. Kieffer, M. C. Malin, J. C. Pearl, J. Carpenter, N. Bandiera, F. G. Brown, and S. H. Silverman (1992), Thermal Emission Spectrometer Experiment: Mars Observer Mission, *Journal of Geophysical Research*, 97, 7719-7734.
- Christensen, P. R., J. L. Bandfield, J. F. I. Bell, N. Gorelick, V. E. Hamilton, A. Ivanov, B. Jakosky, M., H. H. Kieffer, M. D. Lane, M. C. Malin, T. McConnochie, A. S. McEwen, H. Y. McSween, Jr., G. L. Mehall, J. E. Moersch, K. H. Nealson, J. W. Rice, Jr., M. I. Richardson, S. W. Ruff, M. D. Smith, T. N. Titus, and M. B. Wyatt (2003), Morphology and composition of the surface of Mars: Mars Odyssey THEMIS results, *Science*, 300, 2056-2061.
- Christensen, P. R., J. L. Bandfield, R. N. Clark, K. S. Edgett, V. E. Hamilton, T. M. Hoefen, H. H. Kieffer, R. O. Kuzmin, M. D. Lane, M. C. Malin, R. V. Morris, J. C. Pearl, R. Pearson, T. L. Roush, S. W. Ruff, and M. D. Smith (2000a), Detection of crystalline hematite mineralization on Mars by the Thermal Emission Spectrometer: Evidence for near-surface water, *Journal of Geophysical Research*, 105, 9623-9642.

- Christensen, P. R., J. L. Bandfield, V. E. Hamilton, D. A. Howard, M. D. Lane, J. L. Piatek, S. W. Ruff, and W. L. Stefanov (2000b), A thermal emission spectral library of rock-forming minerals, *Journal of Geophysical Research*, *105*, 9735-9739.
- Christensen, P. R., J. L. Bandfield, V. E. Hamilton, S. W. Ruff, H. H. Kieffer, T. N. Titus, M. C. Malin, R. V. Morris, M. D. Lane, R. N. Clark, B. Jakosky, M., M. T. Mellon, J. C. Pearl, B. J. Conrath, M. D. Smith, R. T. Clancy, R. O. Kuzmin, T. Roush, G. L. Mehall, N. Gorelick, K. Bender, K. Murray, S. Dason, E. Greene, S. H. Silverman, and M. Greenfield (2001a), Mars Global Surveyor Thermal Emission Spectrometer experiment: Investigation description and surface science results, *Journal of Geophysical Research*, *106*, 23823-23871.
- Christensen, P. R., J. L. Bandfield, M. D. Smith, V. E. Hamilton, and R. N. Clark (2000c), Identification of a basaltic component on the Martian surface from Thermal Emission Spectrometer data, *Journal of Geophysical Research*, *105*, 9609-9621.
- Christensen, P. R., B. Jakosky, M., H. H. Kieffer, M. C. Malin, H. Y. McSween, Jr., K. H. Nealson, G. L. Mehall, S. H. Silverman, S. Ferry, M. Caplinger, and M. Ravine (2004a), The Thermal Emission Imaging System (THEMIS) for the Mars 2001 Odyssey mission, *Space Science Reviews*, *110*, 85-130.
- Christensen, P. R., and H. J. Moore (1992), The Martian surface layer, in *Mars*, edited by H. H. Kieffer, Univ. of Ariz. Press, Tucson.
- Christensen, P. R., R. V. Morris, M. D. Lane, J. L. Bandfield, and M. C. Malin (2001b), Global mapping of Martian hematite mineral deposits: Remnants of water-driven processes on early Mars, *Journal of Geophysical Research*, *106*, 23873-23885.
- Christensen, P. R., M. B. Wyatt, T. D. Glotch, D. Rogers, S. Anwar, R. E. Arvidson, J. L. Bandfield, D. L. Blaney, C. Budney, W. M. Calvin, A. Fallacaro, R. L. Fergason, N. Gorelick, T. G. Graff, V. E. Hamilton, A. G. Hayes, J. R. Johnson, A. T. Knudson, H. Y. McSween, Jr., G. L. Mehall, L. K. Mehall, J. E. Moersch, R. V. Morris, M. D. Smith, S. W. Squyres, S. W. Ruff, and M. J. Wolff (2004b), Mineralogy at Meridiani Planum from the Mini-TES experiment on the Opportunity rover, *Science*, *306*, 1733-1739.
- Craddock, R. A., and T. A. Maxwell (1990), Resurfacing of the Martian highlands in the Amenthes and Tyrrhena region, *Journal of Geophysical Research*, *95*, 14265-14278.
- Crisp, J. A., A. B. Kahle, and E. A. Abbott (1990), Thermal infrared spectral character of Hawaiian basaltic glasses, *Journal of Geophysical Research*, *95*, 21657-21669.

- Crown, D. A., L. F. I. Bleamaster, and S. C. Mest (2005), Styles and timing of volatile-driven activity in the eastern Hellas region of Mars, *Journal of Geophysical Research*, 110, doi:10.1029/2005JE002496.
- Crown, D. A., and C. M. Pieters (1987), Spectral properties of plagioclase and pyroxene mixtures and the interpretation of lunar soil spectra, *Icarus*, 72, 492-506.
- Deer, W. A., R. A. Howie, and J. Zussman (1992), *An Introduction to the Rock-forming Minerals*, 2nd ed. ed., 696 pp., Longman, London.
- Duke, D. A., and J. D. Stephens (1964), Infrared investigation of the olivine group minerals, *American Mineralogist*, 49, 1388-1406.
- Elkins-Tanton, L., T., P. C. Hess, and E. M. Parmentir (2005), Possible formation of ancient crust on Mars through magma ocean processes, *Journal of Geophysical Research*, 110, doi:10.1029/2005JE002480.
- Fabian, D., T. Henning, C. Jäger, H. Mutschke, J. Dorschner, and O. Wehrhan (2001), Steps toward interstellar silicate mineralogy VI. Dependence of crystalline olivine IR spectra on iron content and particle shape, *Astronomy & Astrophysics*, 378, 228-238, DOI: 210/1051/0004-6361:20011196.
- Feely, K. C., and P. R. Christensen (1999), Quantitative compositional analysis using thermal emission spectroscopy: Application to igneous and metamorphic rocks, *Journal of Geophysical Research*, 104, 24195-24210.
- Fenton, L. K., and M. I. Richardson (2001), Martian surface winds: Insensitivity to orbital changes and implications for aeolian processes, *Journal of Geophysical Research*, 106, 32885-32902.
- Fergason, R. L., P. R. Christensen, J. F. Bell, III, M. P. Golombek, K. E. Herkenhoff, and H. H. Kieffer (2006), Physical properties of the Mars Exploration Rover landing sites as inferred from Mini-TES-derived thermal inertia, *Journal of Geophysical Research*, 111, doi:10.1029/2005JE002583.
- Friedman Lentz, R. C., G. Taylor, J., and A. H. Treiman (1999), Formation of a martian pyroxenite: A comparative study of the nakhlite meteorites and Theo's Flow, *Meteorit. Planet. Sci.*, 34, 919-932.
- Garcia, M. O., T. P. Hulsebosch, and J. M. Rhodes (1995), Olivine-rich submarine basalts from the southwest rift zone of Mauna Loa volcano: Implications for magmatic processes and geochemical evolution, edited, pp. 219-239, American Geophysical Union, Washington, D. C.

- Gillespie, A. R. (1992), Spectral mixture analysis of multispectral thermal infrared images, *Remote Sensing of the Environment*, 42, 137-145.
- Gillespie, A. R., A. B. Kahle, and R. E. Walker (1986), Color enhancement of highly correlated images: I. Decorrelation and HSI contrast stretches, *Remote Sensing of the Environment*, 20, 209-235.
- Goldich, S. S. (1938), A study of rock weathering, *J. Geology*, 46, 17-58.
- Gooding, J. L., S. J. Wentworth, and M. E. Zolensky (1991), Aqueous alteration of the Nakhla meteorite, *Meteoritics*, 26, 135-143.
- Gorelick, N. S., M. Weiss-Malik, B. Steinberg, and S. Anwar (2003), JMARS: A multimission data fusion application, LPSC XXXIV, abstract #2057.
- Greeley, R., and J. E. Guest (1987), Geologic map of the eastern equatorial region of Mars, U.S. Geol. Surv. Misc. Invest. Map, I-1802-B.
- Hamilton, V. E. (2000), Thermal infrared emission spectroscopy of the pyroxene mineral series, *Journal of Geophysical Research*, 105, 9701-9716.
- Hamilton, V. E. (2003), Constraints on the composition and particle size of high albedo regions on Mars, Sixth International Conference on Mars, abstract 3239.
- Hamilton, V. E., and P. R. Christensen (2000), Determining the modal mineralogy of mafic and ultramafic igneous rocks using thermal emission spectroscopy, *Journal of Geophysical Research*, 105, 9717-9733.
- Hamilton, V. E., and P. R. Christensen (2005), Evidence for extensive, olivine-rich bedrock in Nili Fossae, Mars, *Geology*, 33, 433-436.
- Hamilton, V. E., P. R. Christensen, and H. Y. McSween, Jr. (1997), Determination of Martian meteorite lithologies and mineralogies using vibrational spectroscopy, *Journal of Geophysical Research*, 102, 593-525,603.
- Hamilton, V. E., P. R. Christensen, H. Y. McSween, Jr., and J. L. Bandfield (2003), Searching for the source regions of Martian meteorites using MGS TES: Integrating Martian meteorites into the global distribution of igneous materials on Mars, *Meteorit. Planet. Sci.*, 38, 871-885.
- Hamilton, V. E., W. C. Koeppen, and D. H. Lineberger (in prep.), The thermal infrared spectra of the olivine series: forsterite to fayalite, *Icarus*.
- Hamilton, V. E., and P. G. Lucey (2005), One spectrometer, two spectra: Complementary hemispherical reflectance and thermal emission spectroscopy using a single FTIR instrument, LPSC XXXVI, abstract 1272.

- Hamilton, V. E., M. B. Wyatt, H. Y. McSween, Jr., and P. R. Christensen (2001), Analysis of terrestrial and Martian volcanic compositions using thermal emission spectroscopy: 2. Application to Martian surface spectra from the Mars Global Surveyor Thermal Emission Spectrometer, *Journal of Geophysical Research*, 106, 14733-14746.
- Hartmann, W. K. (2005), Martian cratering 8: Isochron refinement and the chronology of Mars, *Icarus*, 174, 294-320.
- Hartmann, W. K., and G. Neukum (2001), Cratering chronology and the evolution of Mars, *Space Science Reviews*, 96, 165-194.
- Hochberg, E. J., and M. Atkinson, J. (2003), Capabilities of remote sensors to classify coral, algae, and sand as pure and mixed spectra, *Remote Sensing of the Environment*, 85, 174-189.
- Hoefen, T. M., and R. N. Clark (2001), Compositional variability of Martian olivines using Mars Global Surveyor Thermal Emission Spectra, LPSC XXXII, abstract 2049.
- Hoefen, T. M., R. N. Clark, J. L. Bandfield, M. D. Smith, J. C. Pearl, and P. R. Christensen (2003), Discovery of olivine in the Nili Fossae region of Mars, *Science*, 302, 627-630.
- Howard, A. D., J. M. Moore, and R. P. Irwin, III (2005), An intense terminal epoch of widespread fluvial activity on early Mars: 1. Valley network incision and associated deposits, *Journal of Geophysical Research*, 110, doi:10.1029/2005JE002459.
- Hunt, G. R., and R. K. Vincent (1968), The behavior of spectral features in the infrared emission from particulate surfaces of various grain sizes, *Journal of Geophysical Research*, 73, 6039-6046.
- Irwin, R. P., III, A. D. Howard, R. A. Craddock, and J. M. Moore (2005), An intense terminal epoch of widespread fluvial activity on early Mars: 2. Increased runoff and paleolake development, *Journal of Geophysical Research*, 110, E12S15.
- Jackson (1983), Spectral indices in n-space, *Remote Sensing of the Environment*, 13, 409-421.
- Jakosky, B., M., M. T. Mellon, H. H. Kieffer, P. R. Christensen, E. S. Varnes, and S. W. Lee (2000), The thermal inertia of Mars from the Mars Global Surveyor Thermal Emission Spectrometer, *Journal of Geophysical Research*, 105, 9643-9652.
- Jakosky, B. M. (1986), On the thermal properties of Martian fines, *Icarus*, 66, 117-124.

- Johnson, J. R., F. Hörz, and M. I. Staid (2003), Thermal infrared spectroscopy and modeling of experimentally shocked plagioclase feldspars, *American Mineralogist*, 88, 1575-1582.
- Johnson, P. E., M. O. Smith, S. Taylor-George, and J. B. Adams (1983), A semiempirical method for analysis of the reflectance spectra of binary mineral mixtures, *Journal of Geophysical Research*, 88, 3,557-553,561.
- Joshi, M. M., R. M. Haberle, J. R. Barnes, J. R. Murphy, and J. Schaeffer (1997), Low-level jets in the NASA Ames general circulation model, *Journal of Geophysical Research*, 102, 6511-6523.
- Kanner, L. C., J. F. Mustard, J.-P. Bibring, A. Gendrin, Y. Langevin, B. Gondet, S. M. Pelkey, and t. O. S. Team (2005), Analysis of Martian pyroxene compositions in Syrtis Major: Full MGM application to OMEGA, LPSC XXXVI, abstract 1730.
- Kauth, R. J., and G. S. Thomas (1976), The tasseled cap - a graphic description of the spectral-temporal development of agricultural crops as seen by Landsat, Symposium on Machine Processing of Remotely Sensed Data, 41-51.
- Kieffer, H. H., T. Z. Martin, A. R. Peterfreund, B. M. Jakosky, E. D. Miner, and F. D. Palluconi (1977), Thermal and albedo mapping of Mars during the Viking primary mission, *Journal of Geophysical Research*, 82, 4249-4291.
- Klein, C. (1983), Diagenesis and metamorphism of Precambrian iron-formations, in *Iron-Formation: Facts and Problems*, edited by A. F. Trendall and R. C. Morris, pp. 417-469, Elsevier, Amsterdam.
- Klein, C. (2005), Some Precambrian banded iron-formations (BIFs) from around the world: Their age, geologic setting, mineralogy, metamorphism, geochemistry, and origin, *American Mineralogist*, 90, 1473-1499.
- Klein, C., and C. S. Hurlbut, Jr. (1985), *Manual of Mineralogy*, after James D. Dana, 21 ed., 681 pp., John Wiley & Sons, New York.
- Koeppen, W. C., and V. E. Hamilton (in press), The global distribution, composition, and abundance of olivine on the surface of Mars from thermal infrared data, *Journal of Geophysical Research*, #2007JE002984R.
- Koike, C., H. Chihara, A. Tsuchiyama, H. Suto, H. Sogawa, and H. Okuda (2003), Compositional dependence of infrared absorption spectra of crystalline silicate: II. Natural and synthetic olivines, *Astronomy & Astrophysics*, 399, 1101-1107.

- Kraft, M. D., J. R. Michalski, and T. G. Sharp (2003), Effects of pure silica coatings on thermal emission spectra of basaltic rocks: Considerations for Martian surface mineralogy, *Geophysical Research Letters*, *30*, doi:10.1029/2003GL018848.
- Lane, M. D. (2007), Mid-infrared emission spectroscopy of sulfate and sulfate-bearing minerals, *American Mineralogist*, *92*, 1-18.
- Lawson, C. L., and R. J. Hanson (1974), *Solving Least Squares Problems*, 340 pp., Prentice Hall, Upper Saddle River, N. J.
- Leonard, G. J., and K. L. Tanaka (2001), Geologic map of the Hellas region of Mars, U.S. Geol. Surv. Geologic. Invest. Map, I-2694.
- Lodders, K., and B. Fegley, Jr. (1997), An oxygen isotope model for the composition of Mars, *Icarus*, *126*, 373-394.
- Longhi, J., E. Knittle, J. R. Holloway, and H. Wänke (1992), The bulk composition, mineralogy and internal structure of Mars, in *Mars*, edited by H. H. Kieffer, et al., pp. 185-208, The University of Arizona Press, Tucson.
- Lucey, P. G., J. Hinrichs, M. L. Urquhart, D. Wellnitz, N. Izenberg, S. L. Murchie, M. Robinson, B. E. Clark, and J. F. I. Bell (2002), Detection of temperature-dependent spectral variation on the asteroid Eros and new evidence for the presence of an olivine-rich silicate assemblage, *Icarus*, *155*, 181-188, doi:110.1006/icar.2001.6747.
- Lyon, R. J. P. (1959), Quantitative mineralogy in 30 minutes, *Econ. Geology*, *54*, 1047-1055.
- Malin, M. C., G. E. Danielson, A. P. Ingersoll, H. Masursky, J. Veverka, M. A. Ravine, and T. A. Soulanille (1992), Mars Observer Camera, *Journal of Geophysical Research*, *97*, 7699-7718.
- Malin, M. C., and K. S. Edgett (2001), Mars Global Surveyor Mars Orbiter Camera-Interplanetary cruise through primary mission, *Journal of Geophysical Research*, *106*, 23429-23570.
- Malin, M. C., and K. S. Edgett (2003), Evidence for persistent flow and aqueous sedimentation on early Mars, *Science*, *302*, 1931-1934.
- Martinez-Alonso, S., M. T. Mellon, B. C. Kindel, and B. Jakosky, M. (2006), Mapping compositional diversity on the surface of Mars: The Spectral Variance Index, *Journal of Geophysical Research*, *111*, doi:10.1029/2005JE002492.

- Mason, B. (1981), ALHA77005 petrographic description, in *Antarctic Meteorite Newsletter*, edited, p. 12, JSC Curator's Office, Houston.
- McSween, H. Y., Jr., R. E. Arvidson, J. F. I. Bell, D. L. Blaney, N. A. Cabrol, P. R. Christensen, B. C. Clark, J. A. Crisp, L. S. Crumpler, D. J. Des Marais, J. D. Farmer, R. Gellert, A. Ghosh, S. Gorevan, T. G. Graff, J. Grant, L. A. Haskin, K. E. Herkenhoff, J. R. Johnson, B. L. Jolliff, G. Klingelhöfer, A. T. Knudson, S. McLennan, K. A. Milam, J. E. Moersch, R. V. Morris, R. Rieder, S. W. Ruff, P. A. de Souza, Jr., S. W. Squyres, H. Wänke, A. Wang, M. B. Wyatt, A. Yen, and J. Zipfel (2004), Basaltic rocks analyzed by the Spirit rover in Gusev Crater, *Science*, *305*, 842-845.
- McSween, H. Y., Jr., T. L. Grove, and M. B. Wyatt (2003), Constraints on the composition and petrogenesis of the Martian crust, *Journal of Geophysical Research*, *108*, 5135, doi:5110.1029/2003JE002175.
- McSween, H. Y., Jr., E. Stolper, L. A. Taylor, R. A. Muntean, G. D. O'Kelley, J. S. Eldridge, S. Biswas, H. T. Ngo, and M. E. Lipschutz (1979), Petrogenetic relationship between Allan Hills 77005 and other achondrites, *Earth Planet. Sci. Lett.*, *45*, 275-284.
- McSween, H. Y., Jr., and A. H. Treiman (1998), Martian meteorites, in *Planetary Materials*, edited by J. Papike, pp. 6.1-6.53, Mineralogical Society of America, Washington D. C.
- McSween, H. Y., Jr., M. B. Wyatt, R. Gellert, J. F. I. Bell, R. V. Morris, K. E. Herkenhoff, L. S. Crumpler, K. A. Milam, K. R. Stockstill, L. L. Tornabene, R. E. Arvidson, P. Bartlett, D. L. Blaney, N. A. Cabrol, P. R. Christensen, B. C. Clark, J. A. Crisp, D. J. Des Marais, T. Economou, J. D. Farmer, W. Farrand, A. Ghosh, M. P. Golombek, S. Gorevan, R. Greeley, V. E. Hamilton, J. R. Johnson, B. L. Jolliff, G. Klingelhöfer, A. T. Knudson, S. McLennan, D. W. Ming, J. E. Moersch, R. Rieder, S. W. Ruff, C. Schröder, P. A. de Souza, S. W. Squyres, H. Wänke, A. Wang, A. Yen, and J. Zipfel (2006), Characterization and petrologic interpretation of olivine-rich basalts at Gusev Crater, Mars, *Journal of Geophysical Research*, *111*, doi:10.1029/2005JE002477.
- Mellon, M. T., and B. Jakosky, M. (1995), The distribution and behavior of Martian ground ice during past and present epochs, *Journal of Geophysical Research*, *100*, 11781-11799.
- Mellon, M. T., B. Jakosky, M., H. H. Kieffer, and P. R. Christensen (2000), High-resolution thermal inertia mapping from the Mars Global Surveyor Thermal Emission Spectrometer, *Icarus*, *148*, 437-455.
- Melosh, H. J. (1989), *Impact Cratering*, 245 pp., Oxford University Press, New York.

- Mest, S. C., and D. A. Crown (2006), Geologic map of the MTM-20272 and -25272 quadrangles, Tyrrhena Terra region of Mars, U.S. Geol. Surv. Scientific Investigations Map 2934.
- Michalski, J. R., M. D. Kraft, T. Diedrich, T. G. Sharp, and P. R. Christensen (2003), Thermal emission spectroscopy of the silica polymorphs and considerations for remote sensing of Mars, *Geophysical Research Letters*, *30*, doi:10.1029/2003GL018354.
- Michalski, J. R., M. D. Kraft, T. G. Sharp, L. B. Williams, and P. R. Christensen (2005), Mineralogical constraints on the high-silica martian surface component observed by TES, *Icarus*, *174*, 161-177, doi:10.1016/j.icarus.2004.1010.1022.
- Milam, K. A., H. Y. McSween, Jr., V. E. Hamilton, J. E. Moersch, and P. R. Christensen (2004), Accuracy of plagioclase compositions from laboratory and Mars spacecraft thermal emission spectra, *Journal of Geophysical Research*, *109*, doi:10.1029/2003JE002097.
- Minitti, M. E., J. F. Mustard, and M. J. Rutherford (2002), Effects of glass content and oxidation on the spectra of SNC-like basalts: Applications to Mars remote sensing, *Journal of Geophysical Research*, *107*, doi:10.1029/2001JE001518.
- Moersch, J. E., and P. R. Christensen (1995), Thermal emission from particulate surfaces: A comparison of scattering models with measured spectra, *Journal of Geophysical Research*, *100*, 7465-7477.
- Moersch, J. E., and P. R. Christensen (1995), Thermal emission from particulate surfaces: A comparison of scattering models with measured spectra, *Journal of Geophysical Research*, *100*, 7465-7477.
- Moore, J. M., and A. D. Howard (2005), Large alluvial fans on Mars, *Journal of Geophysical Research*, *110*.
- Morris, R. V., G. Klingelhöfer, B. Bernhardt, C. Schröder, D. S. Rodionov, P. A. de Souza, Jr., A. Yen, R. Gellert, E. N. Evlanov, J. Foh, E. Kankeleit, P. Gütlich, D. W. Ming, F. Renz, T. Wdowiak, S. W. Squyres, and R. E. Arvidson (2004), Mineralogy at Gusev Crater from the Mössbauer spectrometer on the Spirit rover, *Science*, *305*, 833-836.
- Morse, S. A. (1996), Kiglapait mineralogy III: Olivine compositions and Rayleigh fractionation models, *J. Petrology*, *37*, 1037-1061.
- Murchie, S. L., L. Kirkland, S. Erard, J. F. Mustard, and M. Robinson (2000), Near-infrared spectral variations of Martian surface materials from ISM imaging spectrometer data, *Icarus*, *147*, 444-471.

- Mustard, J. F., and C. D. Cooper (2005), Joint analysis of ISM and TES spectra: The utility of multiple wavelength regimes for Martian surface studies, *Journal of Geophysical Research*, *110*, doi:10.1029/2004JE002355.
- Mustard, J. F., S. Erard, J.-P. Bibring, J. W. I. Head, S. Hurtrez, Y. Langevin, C. M. Pieters, and C. J. Sotin (1993), The surface of Syrtis Major: Composition of the volcanic substrate and mixing with altered dust and soil, *Journal of Geophysical Research*, *98*, 3387-3400.
- Mustard, J. F., and J. E. Hays (1997), Effects of hyperfine particles on reflectance spectra from 0.3 to 25 microns, *Icarus*, *125*, 145-163.
- Mustard, J. F., S. L. Murchie, B. L. Ehlmann, S. M. Pelkey, L. A. Roach, F. P. Seelos, IV, F. Poulet, J.-P. Bibring, N. Mangold, J. A. Grant, R. E. Milliken, and t. C. team (2007a), CRISM-OMEGA observations of phyllosilicate-olivine stratigraphy in Nili Fossae, Mars, LPSC XXXVIII, abstract 2071.
- Mustard, J. F., F. Poulet, A. Gendrin, J.-P. Bibring, Y. Langevin, B. Gondet, N. Mangold, G. Bellucci, and F. Altieri (2005), Olivine and pyroxene diversity in the crust of Mars, *Science*, *307*, 1594-1597.
- Mustard, J. F., F. Poulet, J. W. Head, III, N. Mangold, J.-P. Bibring, S. M. Pelkey, C. I. Fassett, Y. Langevin, and G. Neukum (2007b), Mineralogy of the Nili Fossae region with OMEGA/Mars Express data: 1. Ancient impact melt in the Isidis Basin and implications for the transition from the Noachian to Hesperian, *Journal of Geophysical Research*, *112*, doi:10.1029/2006JE002834.
- Mustard, J. F., F. Poulet, J. W. I. Head, N. Mangold, J.-P. Bibring, C. Fassett, Y. Langevin, and G. Neukum (2006), Ancient crust, aqueous alteration, and impact melt preserved in the Isidis Basin, Mars, LPSC XXXVII, abstract 1683.
- Neugebauer, G., G. Münch, H. H. Kieffer, S. C. Chase, Jr., and E. D. Miner (1971), Mariner 1969 infrared radiometer results: Temperatures and thermal properties of the Martian surface, *Astron. J.*, *76*, 719-728.
- Noble, S. K., and C. M. Pieters (2001), Type 2 terrain: Compositional constraints on the Martian lowlands, LPSC XXXII, abstract 1230.
- Papike, J. J., G. Ryder, and C. K. Shearer (1998), Lunar samples, in *Planetary Materials*, edited by J. Papike, Mineralogical Society of America, Washington D. C.
- Pearl, J. C., M. D. Smith, B. J. Conrath, J. L. Bandfield, and P. R. Christensen (2001), Observations of Martian ice clouds by the Mars Global Surveyor Thermal Emission Spectrometer: The first Martian year, *Journal of Geophysical Research*, *106*, 12,325-312,338.

- Piatek, J. L. (1997), Vibrational spectroscopy of clay minerals: Implications for remote sensing of terrestrial planetoids, Masters thesis, 78 pp, Arizona State University, Tempe.
- Pieters, C. M. (1982), Copernicus Crater central peak: Lunar mountain of unique composition, *Science*, *215*, 59-61.
- Pokrovsky, O. S., and J. Schott (2000), Kinetics and mechanism of forsterite dissolution at 25°C and pH from 1 to 12, *Geochimica et Cosmochimica Acta*, *64*, 3313-3325.
- Poulet, F., and S. Erard (2004), Nonlinear spectral mixing: Quantitative analysis of laboratory mineral mixtures, *Journal of Geophysical Research*, *109*, doi:10.1029/2003JE002179.
- Poulet, F., C. Gomez, J.-P. Bibring, Y. Langevin, B. Gondet, P. Pinet, G. Belluci, and J. F. Mustard (2007), Martian surface mineralogy from Observatoire pour la Minéralogie, l'Eau, les Glaces et l'Activité on board the Mars Express spacecraft (OMEGA/MEx): Global mineral maps, *Journal of Geophysical Research*, *112*, doi:/2006JE002840.
- Presley, M. A., and P. R. Christensen (1997), Thermal conductivity measurements of particulate materials: 2. Results, *Journal of Geophysical Research*, *102*, 6551-6566.
- Presley, M. A., and R. A. Craddock (2006), Thermal conductivity measurements of particulate materials: 3. Natural samples and mixtures of particle sizes, *Journal of Geophysical Research*, *111*, doi:10.1029/2006JE002706.
- Prinz, M., P. H. Hlava, and K. Keil (1974), The Chassigny meteorite: A relatively iron-rich cumulate dunite, *Meteoritics*, *9*, 393-394.
- Putzig, N. E., and M. T. Mellon (2007), Apparent thermal inertia and the surface heterogeneity of Mars, *Icarus*, *191*, 68-94.
- Ramsey, M. S., and P. R. Christensen (1998), Mineral abundance determination: Quantitative deconvolution of thermal emission spectra, *Journal of Geophysical Research*, *103*, 577-596.
- Ramsey, M. S., and J. H. Fink (1999), Estimating silicic lava vesicularity with thermal remote sensing: A new technique for volcanic mapping and monitoring., *Bull. Volcanol.*, *61*, 32-39.
- Rencher, A. C. (1995), *Methods of multivariate analysis*, 2nd ed., 627 pp., Wiley Interscience, New York.

- Richardson, A. J., and C. L. Wiegand (1977), Distinguishing vegetation from soil background information, *Photogrammetric Engineering and Remote Sensing*, *43*, 1541-1552.
- Rogers, A. D., J. L. Bandfield, and P. R. Christensen (2007), Global spectral classification of Martian low-albedo regions with Mars Global Surveyor Thermal Emission Spectrometer (MGS-TES) data, *Journal of Geophysical Research*, *112*, doi:10.1029/2006JE002726.
- Rogers, A. D., and P. R. Christensen (2007), Surface mineralogy of Martian low-albedo regions from MGS-TES data: Implications for upper crustal evolution and surface alteration, *Journal of Geophysical Research*, *112*, doi:10.1029/2006JE002727.
- Rogers, A. D., P. R. Christensen, and J. L. Bandfield (2005), Compositional heterogeneity of the ancient Martian crust: Analysis of Ares Vallis bedrock with THEMIS and TES data, *Journal of Geophysical Research*, *110*, doi:10.1029/2005JE002399.
- Ruff, S. W. (2003), Basaltic andesite or weathered basalt: A new assessment, Sixth International Conference on Mars.
- Ruff, S. W. (2004), Spectral evidence for zeolite in the dust on Mars, *Icarus*, *168*, 131-143.
- Ruff, S. W., and P. R. Christensen (2002), Bright and dark regions on Mars: Particle size and mineralogical characteristics based on Thermal Emission Spectrometer data, *Journal of Geophysical Research*, *107*, doi:10.1029/2001JE001580.
- Ruff, S. W., and P. R. Christensen (2007), Basaltic andesite, altered basalt, and a TES-based search for smectite clay minerals on Mars, *Geophysical Research Letters*, *34*, doi:10.1029/2007GL029602.
- Ruff, S. W., P. R. Christensen, P. W. Barbera, and D. L. Anderson (1997), Quantitative thermal emission spectroscopy of minerals: A laboratory technique for measurement and calibration, *Journal of Geophysical Research*, *102*, 14899-14913.
- Salisbury, J. W. (1993), Mid-infrared spectroscopy: Laboratory data, in *Remote Geochemical Analysis*, edited by C. M. Pieters and P. A. J. Englert, pp. 79-98, Cambridge University Press, New York.
- Salisbury, J. W., and A. Wald (1992), The role of volume scattering in reducing spectral contrast of reststrahlen bands in spectra of powdered minerals, *Icarus*, *96*, 121-128.

- Salisbury, J. W., L. S. Walter, N. Vergo, and D. M. D'Aria (1991), *Infrared (2.1-25 μ m) Spectra of Minerals*, 267 pp., The Johns Hopkins University Press, Baltimore.
- Scott, D. H., and K. L. Tanaka (1986), Geologic map of the western equatorial region of Mars, U.S. Geol. Surv. Misc. Invest. Map, I-1802-A.
- Smith, D. E., and M. T. Zuber (1998), The relationship between MOLA northern hemisphere topography and the 6.1-mbar atmospheric pressure surface of Mars, *Geophysical Research Letters*, 25, 4397-4400.
- Smith, D. E., M. T. Zuber, H. V. Frey, J. B. Garvin, J. W. Head, D. O. Muhleman, G. H. Pettengill, R. J. Phillips, S. C. Solomon, and H. J. Zwally (2001), Mars Orbiter Laser Altimeter: Experiment summary after the first year of global mapping of Mars, *Journal of Geophysical Research*, 106, 23689-23722.
- Smith, M. D. (2002), The annual cycle of water vapor on Mars as observed by the Thermal Emission Spectrometer, *Journal of Geophysical Research*, 107, doi:10.1029/2001JE001522.
- Smith, M. D., J. L. Bandfield, and P. R. Christensen (2000), Separation of atmospheric and surface spectral features in Mars Global Surveyor Thermal Emission Spectrometer (TES) spectra, *Journal of Geophysical Research*, 105, 9589-9607.
- Soha, J. M., and A. A. Schwartz (1978), Multispectral histogram normalization contrast enhancement, Proc. 5th Canadian Symposium on Remote Sensing, 86-93.
- Squyres, S. W., J. P. Grotzinger, R. E. Arvidson, J. F. I. Bell, W. M. Calvin, P. R. Christensen, B. C. Clark, J. A. Crisp, W. H. Farrand, K. E. Herkenhoff, J. R. Johnson, G. Klingelhöfer, A. H. Knoll, S. M. McLennan, H. Y. McSween, Jr., R. C. Morris, J. W. Rice, Jr., R. Rieder, and L. A. Soderblom (2004), In situ evidence for an ancient aqueous environment at Meridiani Planum, Mars, *Science*, 306, 1709-1714.
- Staid, M. I., L. R. Gaddis, and T. N. Titus (2001), A new approach for mapping minerals on Mars with TES data, *Eos Trans. AGU*, 82, abstract P42.0553.
- Staid, M. I., J. R. Johnson, and L. R. Gaddis (2004), Analysis of Mars Thermal Emission Spectrometer Data Using Large Mineral Reference Libraries, LPSC XXXV, abstract 1778.
- Stopar, J. D., G. Taylor, J., V. E. Hamilton, and L. Browning (2006), Kinetic model of olivine dissolution and extent of aqueous alteration on Mars, *Geochimica et Cosmochimica Acta*, 70, 6136-6152.

- Taylor, G. J., W. V. Boynton, J. Brückner, H. Wänke, G. Dreibus, K. Kerry, J. Keller, R. C. Reedy, L. G. Evans, R. Starr, S. W. Squyres, S. Karunatillake, O. Gasnault, S. Maurice, C. d'Uston, P. A. J. Englert, J. Dohm, V. Baker, D. K. Hamara, D. M. Janes, A. Sprague, K. Kim, and D. M. Drake (2006), Bulk composition and early differentiation of Mars, *Journal of Geophysical Research*, *111*, doi:10.1029/2005JE002645.
- Thomson, J. L., and J. W. Salisbury (1993), The mid-infrared reflectance of mineral mixtures (7-14 μm), *Remote Sensing of the Environment*, *45*, 1-13.
- Tompkins, S., and C. M. Pieters (1999), Mineralogy of the lunar crust: Results from Clementine, *Meteorit. Planet. Sci.*, *34*, 25-41.
- Tornabene, L. L., J. E. Moersch, H. Y. McSween, Jr., V. E. Hamilton, J. L. Piatek, and P. R. Christensen (submitted), Surface and crater-exposed lithologic units of the Isidis Basin as mapped by co-analysis of THEMIS and TES derived data products, *Journal of Geophysical Research*.
- Toulmin, P., III, A. K. Baird, B. C. Clark, K. Keil, J. H. J. Rose, R. P. Christian, P. H. Evans, and W. C. Kelliher (1977), Geochemical and mineralogical interpretation of the Viking inorganic chemical results, *Journal of Geophysical Research*, *82*, 4626-4634.
- Vincent, R. K., and G. R. Hunt (1968), Infrared Reflectance from Mat Surfaces, *Applied Optics*, *7*, 53-59.
- Wänke, H., and G. Dreibus (1988), Chemical Composition and Accretion History of Terrestrial Planets, *Philosophical Transactions of the Royal Society of London. Series A, Mathematical and Physical Sciences*, *325*, 545-557.
- Wänke, H., G. Dreibus, and I. P. Wright (1994), Chemistry and Accretion History of Mars [and Discussion], *Philosophical Transactions: Physical Sciences and Engineering*, *349*, 285-293.
- Wechsler, A. E., P. E. Glaser, A. D. Little, and J. A. Fountain (1972), Thermal properties of granulated materials, in *Thermal Characteristics of the Moon*, edited by J. W. Lucas, pp. 215-241, MIT Press, Cambridge, MA.
- White, A. F., and S. L. Brantley (2003), The effect of time on the weathering of silicate minerals: Why do weathering rates differ in the laboratory and field?, *Chemical Geology*, *2002*, 479-506.
- Wogelius, R. A., and J. V. Walther (1992), Olivine dissolution kinetics at near surface conditions, *Chem. Geol.*, *97*, 101-112.

- Wood, J. A., D. L. Anderson, W. R. Buck, W. M. Kaula, E. Anders, G. Consolmagno, J. Morgan, A. E. Ringwood, E. Stolper, and H. Wänke (1981), Geophysical and Cosmochemical constraints on properties of mantles of the terrestrial planets, *Basaltic Volcanism in the Terrestrial Planets (Basaltic Volcanism Study Project 1981)*, 633-699.
- Wyatt, M. B., V. E. Hamilton, H. Y. McSween, Jr., P. R. Christensen, and L. A. Taylor (2001), Analysis of terrestrial and Martian volcanic compositions using thermal emission spectroscopy: 1. Determination of mineralogy, chemistry, and classification strategies, *Journal of Geophysical Research*, 106, 14711-14732.
- Wyatt, M. B., and H. Y. McSween, Jr. (2002), Spectral evidence for weathered basalt as an alternative to andesite in the northern lowlands of Mars, *Nature*, 417, 263-266.
- Zuber, M. T., D. E. Smith, S. C. Solomon, D. O. Muhleman, J. W. Head, J. B. Garvin, J. B. Abshire, and J. L. Bufton (1992), The Mars Observer laser altimeter investigation, *Journal of Geophysical Research*, 97, 7781-7797.